DOTTORATO DI RICERCA IN SCIENZE CHIMICHE

CICLO XXXIV

COORDINATORE Prof. PIERO BAGLIONI

Self-assembly of copolymers and capsule formation in complex fluids

Settore Scientifico Disciplinare CHIM/02

Dottorando
Dott. Constantina Sofroniou

_____
(firma)

Tutore
Prof. Piero Baglioni

_____
(firma)

Coordinatore
Prof. Piero Baglioni

_____
(firma)

Anni 2018/2021

Abstract

Currently in the market there is the need of more environmentally friendly encapsulation technologies, less time and energy consuming processes, and release of actives, such as perfume, via other triggers besides the classic mechanical fracturing.

This PhD project aims at the development of a new perfume encapsulation technology based on soft polymeric systems. Soft encapsulation methods are taking advantage of the self-assembly process and are thus more sustainable (use of less energy for capsule formation, less time consuming, more efficient use of materials) and more friendly to the environment as they can use biodegradable and biocompatible materials. Here, amphiphilic graft-copolymers with improved environmental footprint are tested as possible candidates for perfume encapsulation with potential use in commercial liquid home- and personal-care products.

Complex liquid matrices used in industrial formulations are composed by numerous components, such as polymers, surfactants, perfumes and other minors (e.g., pH adjustment agents and structurers for viscosity regulation). Additionally, common industrial perfume accords are most often composed by tens or hundreds of single fragrances. Encapsulation of perfume in such complex liquid systems is a complicated and multidimensional process that involves the interactions between the different formulation components. For that reason, a bottom-to-top approach was followed, for deep understanding of the polymer-surfactant-perfume-media interactions. Our investigation started from simpler liquid matrices, including only one polymer of interest and one perfume raw material (PRM) in aqueous solution. In a later extend, our studies have been extended in more complex liquid matrixes, where perfume encapsulation was carried out in a model industrial formulation, a simplified liquid fabric enhancer (SLFE).

Two commercial polymers have been tested and used as perfume carriers: the polyvinyl acetate - polyethylene glycol graft copolymer, PEG-*g*-PVAc and the polyethylene glycol - polyvinyl acetate - polyvinyl caprolactam graft copolymer, PEG-*g*-(PVAc-*co*-PVCL) known under the commercial name

Soluplus. Additionally, another polymer based on the PEG-*g*-(PVAc-*co*-PVCL) structure, but synthesized within the SAMCAPS European project network, was tested and compared to Soluplus. Several single fragrance molecules, with different hydrophobicity (as expressed by their octanol-water partition coefficient, *log* K_{ow}) but also different chemical characteristics (functional groups, molecular conformation etc.) were used in our studies, in order to obtain insights on the role of perfume nature and the interactions with the polymer that are driving encapsulation.

Our main findings have shown that amphiphilic graft copolymers can be successfully used as perfume encapsulation vectors. Depending on the nature of the polymer and the single PRM, the concentration and the medium used, encapsulation can take place in the form of different self-assembled structures: single chain nanoparticles (SCNPs), micelles, lamellar liquid crystalline phases (L_α), matrix-type microcapsules, core-shell microcapsules and oil-in-water (O/W) emulsions. For the characterization of the self-assembled structures, small angle x-ray scattering (SAXS), small-angle neutron scattering (SANS), confocal laser-scanning microscopy (CLSM) and confocal-Raman microscopy (CRM) have been used as main experimental techniques, complimented by several other techniques, including nuclear magnetic resonance (NMR) spectroscopy, dynamic light scattering (DLS), differential scanning calorimetry (DSC), rheology, tensiometry, optical microscopy and headspace gas chromatography – mass spectrometry (GC-MS). Interestingly, we have shown that the encapsulation of a single fragrance does not depend only on its *log* K_{ow} value, a parameter very often used to describe perfume encapsulation systems. Additionally, other parameters play a key role, like the functional group on the perfume molecule and its molecular conformation. Moreover, small variations on the polymeric structure (e.g. variations of the molecular weight, cloud point temperature, grafting degree) can lead to different self-assembly properties and to more resistant micro-capsules in a simplified liquid fabric enhancer formulation. Finally, performance tests after deposition of SLFE products on fabrics have shown the benefit of using the polymeric carriers *versus* a free perfume in the product.

List of abbreviations

PRM: Perfume raw material

SLFE: Simplified liquid fabric enhancer

PEG: Polyethylene glycol

EO: Ethylenoxide

PVAc: Polyvinyl acetate

VAc: Vinylacetate

PVCL: Polyvinyl caprolactam

VCL: Vinylcaprolactam

log K_{ow}: Octanol-water partition coefficient

SCNP(s): Single chain nanoparticle(s)

L_{α}: Lamellar liquid crystals

O/W: oil in water emulsion

SAXS: small angle x-ray scattering

SANS: small angle neutron scattering

CLSM: confocal laser-scanning microscopy

CRM: Confocal-Raman microscopy

NMR: Nuclear magnetic resonance

DLS: Dynamic light scattering

DSC: differential scanning calorimetry

GC-MS: Gas chromatography / mass spectrometry

EO(s): Essential oil(s)

W/O: Water-in-oil emulsion

SLNs: Solid lipid nanoparticles

NLCs: Nanostructured lipid carriers

MF: Melamine formaldehyde

GUV: Giant unilamellar vesicles

LLC(s): Lamellar liquid crystals

Q_1: Cubic phases

Q_2: Reversed cubic phases

H_1: Hexagonal phases

H_2: Reversed hexagonal phases

CD(s): Cyclodextrin(s)

M_w: Molecular weight

PE: 2-phenyl ethanol

CAR: L-carvone

LIN: Linalool

FLO: Florhydral

CIT: β-citronellol

PIN: α-pinene

LIM: R-limonene

HAB: Habanolide

IES: Iso-E super

MA: Methyl anthranilate

SLD: Scattering length density

DFO: Dry fabric odor

DFO-24: Dry fabric odor after 24 hours

DFO-48: Dry fabric odor after 48 hours

HS: Headspace

SPME: Solid phase micro-extraction

LLPS: Liquid-liquid phase separation

R_H: Hydrodynamic radius

NOESY: Nuclear Overhauser effect spectroscopy

PGSTE: Pulse-gradient stimulated echo

f_a: Amphiphilicity factor

CMC: Critical micelle concentration

D_h: Hydrodynamic diameter

LCST: Lower critical solution temperature

PNIPAm: Poly(N-isopropylacrylamide)

DMSO-d_6: Hexadeuterodimethyl sulfoxide

HSQC: Heteronuclear Single Quantum Coherence

COSY: Correlated spectroscopy

η_B: Blockiness index

Φ_H: Effective volume fraction

N_{agg}: Aggregation number

ΔH_f: Enthalpy of fusion

CPT: Cloud point temperature

GD: Grafting degree

PEO: Polyethylene oxide

Contents

Introduction

Perfumes are used in people's everyday life from the ancient years and the Egyptians until now, where perfumes are incorporated in daily life products including personal care, household and fabric care, food and health care.[1] Their pleasant scent comes from volatile chemicals, either of natural or synthetic origin: the odorous products that can be extracted from plant raw materials are called essential oils (EO), and they are complex mixtures of terpenic hydrocarbons and oxygenated derivatives (aldehydes, ketones, alcohols, phenols, esters), also known as single fragrant molecules or perfume raw materials (PRMs).[2] What makes the use of EOs or their isolated components a challenge, is their low physico-chemical stability coming from their highly volatile nature. Another difficulty is the low water solubility (or insolubility in some cases) that fragrances exhibit, as well as their degradation upon exposure to high temperature, oxygen, or light.[3] All these issues make EOs and single fragrances significantly difficult to handle, especially in industrial liquid formulations that are in most of the cases based in water solutions. For that reason, micro- and nanoencapsulation of perfumes is essential to improve their stability in terms of increased shelf-life and protection from external environmental conditions.[4,5]

Encapsulation can be defined as the process to entrap or enclose an active agent within another substance. The substance that is being encapsulated can be called the core, fill, active or payload phase, while the substance that is used as the encapsulant is often called the capsule, carrier, matrix, shell or coating.[6] The produced particles or capsules can usually have dimensions from few nanometres to a few micrometres. The first microencapsulation example dates back to 1957 and the manufacture of carbonless copying paper by Green and Schleicher.[7,8] Back then, complex coacervation of gelatine and gum arabic was used to encapsulate dyes. Carbonless copy paper is one of the most significant application of the microencapsulation technology that led to the development of various microcapsule products in later years.

1.1. Liquid formulations – fields of application

In the next paragraphs, the main fields of application of perfume, that include home- and personal-care products, food and pesticides/antimicrobials, will be briefly covered. For a more detailed description of perfume usage in such applications, the reason why perfume encapsulation is essential in each case, the most commonly used encapsulation materials, and selected publications, please refer to Paper III in the Appendix.

1.1.1. Home care

Home care fragrance containing products can be listed in three main categories, according to their target surface: household cleaning products (or hard surface cleaners), dishwashing products and laundry detergents.[9] Perfume in such products plays a key role as it is directly linked to the idea of freshness and cleanliness and it's directly proportional to the product's quality for consumers. Fragrance is present in liquid home care products in small amounts (i.e. 0.1 - 1% w/w). The main components of the formulations are usually mixtures of surfactants, depending on the application, for example, anionic (e.g. linear alkyl sulphates) and non-ionic surfactants (e.g. alcohol ethoxylates) for cleaning properties or cationic surfactants (e.g. quaternary ammonium salts with fatty acid chains) that can act as softeners. Other minors can be present in the product, serving special purposes, as for example film-forming polymers such as polyacrylates for giving shining effect after the use of hard surface cleaners, antibacterials such as peroxides for disinfection purposes, enzymes to prevent grease, builders such as sodium citrate for Ca^{2+} removal, thickening agents, pH regulators, foam boosters etc. In laundry detergents, encapsulation of fragrance has a dual role: except of increasing a product's shelf-life by protecting the volatiles from evaporation and degradation, to increase the product's performance by surviving the wash cycle conditions (high temperatures, shear forces) and by prolonging the release of fragrance after its deposition on fabrics.[10] This is not an easy job and not many scaffolds are able to fulfil such requirements. An additional challenge of the field is the increasing attention to microplastic pollution. Since microcapsules present in current home and personal care products contribute to this problem, it's clear why there's such a high interest in developing new encapsulation technologies using biodegradable and

disposable materials.[11–13] Liquid fabric enhancer has been used as target matrix for perfume encapsulation in this PhD thesis.

1.1.2. Personal care

Personal care products containing perfume can be categorised in personal hygiene products including hand or body washing detergents, shampoos, conditioners, toothpastes, shaving creams etc., and cosmetics including face and body creams, moisturizers, peeling products, sunscreen, make-up products etc. Stricter restrictions are in place, related with toxicological tests of the components present in personal care product formulations, since such products come into direct contact with the human skin.[9] The primary component of conventional personal hygiene products, such as shower gels and shampoos, are surfactants (e.g. sodium laureth sulfate) while cosmetics such as body of face creams are based on surfactants and oily substances to provide a smoothing effect on the skin, including triglycerides, glycerol etc. Besides cleaning and conditioning, personal care products may be used for the delivery of other bioactive compounds including antioxidants, disinfectants or beneficial oils. Encapsulation is needed in those cases, to incorporate the active agent in the complex formulation matrix that is usually characterized by high viscosity. Perfume serves many purposes when present in personal care formulations, including providing a pleasant scent, antioxidant activity (e.g. oregano or tea tree oil), cooling feeling (e.g. mint in toothpastes) or pharmacological properties (e.g. chamomile has anti-inflammatory activity on skin).[14]

1.1.3. Food

Flavour and aroma compounds can be found as additives in several food products, including dairy products, beverages, confectionery products or nutraceuticals, a class of foods combining pharmacological properties and nutritional value.[15,16] Flavour and aroma, resulting from the mixture of many volatile fragrance molecules, have a huge impact in food industry as they directly influence satisfaction when the product is consumed. For that reason, encapsulation is extremely important for the protection of perfume from harsh processing and storage conditions, high temperatures and humidity that may cause the loss of aroma and lead to the development of undesired smell or taste with negative influence to the customer.[17] The choice of encapsulant

materials in the case of food products is even more limited as the material needs to be edible and recognized as safe.[18]

1.1.4. Pesticides and antimicrobials

Pesticides and antimicrobials are products used for the elimination of pathogens and pests that are causing damage to crops but are also a danger to animal and human health. Pesticide products are usually sprayed on the crop foliage and thus the product is exposed to an environment that leads to notable losses as a result of leaking, evaporation, or can be simply washed away after rain. For that reason, encapsulation of the active agent is crucial for the agrochemical sector and lately innovate pesticide technologies and smart delivery methods are developing.[19,20] Perfumes and essential oils are incorporated in pesticides and antimicrobials due to their insecticidal, antioxidant, antimicrobial, antifungal and herbicidal effects.[21–24]

1.2. Encapsulation methods

In this section, the main methods of encapsulation will be briefly introduced, that include interfacial or emulsion polymerization, emulsification, encapsulation via lipid carriers and encapsulation in self-assembly colloidal systems. The resulting encapsulation vectors include polymeric micro- and nanocapsules (core-shell, core-multi-shell, multi-core-shell, matrix-like, coacervates), emulsions (O/W, W/O, W/O/W, O/W/O), lipid carriers (SLNs, NLCs), self-assembled colloids (micelles, microemulsions, vesicles, lyotropic liquid crystal phases, coacervates) and unimolecular hosts (cyclodextrins, multiarm star or graft copolymers, single-chain nanoparticles (SCNPs)). All the encapsulation vectors are explained in more detail in Paper III, Appendix.

1.2.1. Interfacial polymerization / Emulsion polymerization

Interfacial polymerization or emulsion polymerization are methods used for the fabrication of core-shell (or core with multiple shells) micro- and nanocapsules (**Figure 1.1**) where polymerization takes place in situ. This method is versatile and efficient, where a variety of monomers can be used (hydrophobicity-hydrophilicity, cross-linkable sites, etc.) allowing for a fine tuning of the properties of the final material. During interfacial polymerization, generally a polycondensation step takes place (chain growth)

at the interface between two immiscible phases. On the other hand, during emulsion polymerization a radical polymerization takes place on the particles that are formed spontaneously when water, a monomer (usually a cross-linker too) and a surfactant are present. The polymer chain grows while the oil phase remains enclosed. Interfacial polycondensation of melamine and formaldehyde (MF) is the most commonly used method of encapsulation. The first use of melamine for the encapsulation of hydrophobic materials in water dates back to 1969, and such microcapsules are still the standard ones used in the laundry detergent and personal care industry.[25] Additionally, urea and formaldehyde derivatives have been extensively used as capsules walls materials too.[26] MF microcapsules exhibit exceptional stability towards mechanical and chemical stresses and long-term resistance to environmental conditions. Investigation of alternative encapsulation methods is on-going for a long time towards new technologies and processes with improved efficiency of their environmental and biodegradability profile. Studies exploiting alternative methods and materials include interfacial polymerization using water-soluble dithiol and oil-soluble acrylate,[27] or the fabrication of light-responsive capsules, for example via incorporation of 2-oxoacetates into poly(urea-urethane) shells[28]. However, until now there's no alternative to fulfil the requirements for efficiency and mechanical resistance of the classic aminoresin microcapsules, so that further work is required towards more sustainable encapsulation technologies.

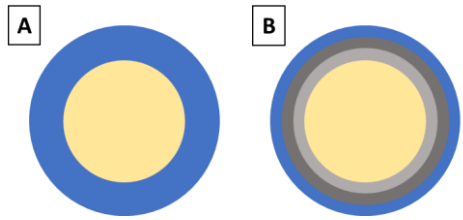

Figure 1.1. Schematic representation of the polymeric micro- and nano-capsules. A: core-shell capsule; B: core-multi-shell capsule.

1.2.2. Emulsification

An emulsion is defined as a fluid colloidal system in which liquid droplets are dispersed in another liquid, and the two media are immiscible. Emulsions can be classified in two main categories: oil-in-water emulsions (O/W) when the

continuous phase is an aqueous solution and water-in-oil emulsions (W/O) when the continuous phase is an organic liquid or an oil. Multiple emulsions can be also formed (**Figure 1.2**). All types of emulsions are metastable colloids, formed in the presence of one or more stabilizing agents (surfactants, hydrotropes, polymers) and upon a non-negligible energy input into the system, typically by means of mechanical- (Ultra-Turrax) or high-pressure homogenization (**Figure 1.3**).[29] Low-energy emulsification methods include the phase-inversion temperature,[30] the phase-inversion composition[31] and the use of microfluidics.[32] Emulsions are not thermodynamically stable phases and they tend to phase separate via different mechanisms (creaming, Ostwald ripening, coalescence, flocculation). Emulsification has been extensively used for the encapsulation of oily molecules, including fragrances, flavours, and essential oils. Selected examples include the encapsulation using microfluidics of oregano essential oil in a nanoemulsion stabilized by sugar-based natural surfactants, presenting high stability against coalescence[33] and multi-wall emulsions generated via layer-by-layer (LbL) amongst alternating layers of tannic acid and bovine serum albumin.[34] Expect of standing alone as an encapsulation method, emulsification is also often the first step for the fabrication of micro- and nanoparticles via further processing (**Figure 1.4**). The most commonly used techniques based on an initial emulsification step include solvent evaporation, emulsion electrospinning, electrospraying and spray-drying. One example is the use of emulsification-gelation of an alginate-amide copolymer with $CaHPO_4$ to encapsulate Osmanthus flower fragrance; the submicron capsules thereby obtained were then used as Pickering emulsion stabilizers for application in cosmetics.[35]

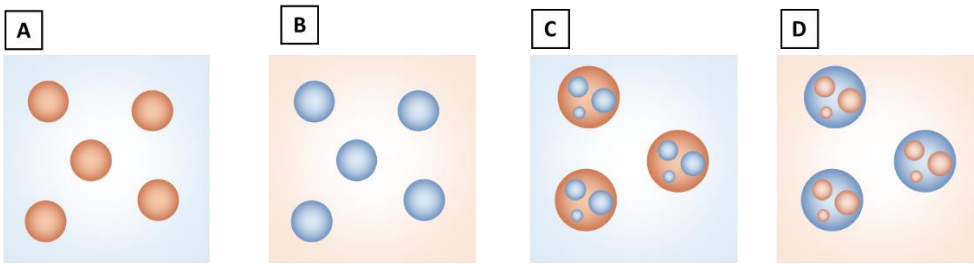

Figure 1.2. Schematic representation of emulsion types. A: oil-in-water emulsion; B: water-in-oil emulsion; C: water-in-oil-in-water emulsion; D: oil-in-water-in-oil emulsion.

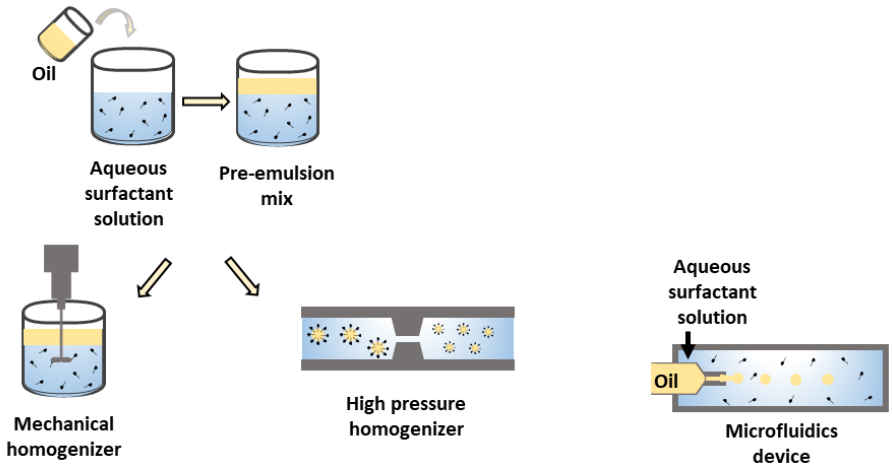

Figure 1.3. Methods of preparation of a typical oil-in-water emulsion system.

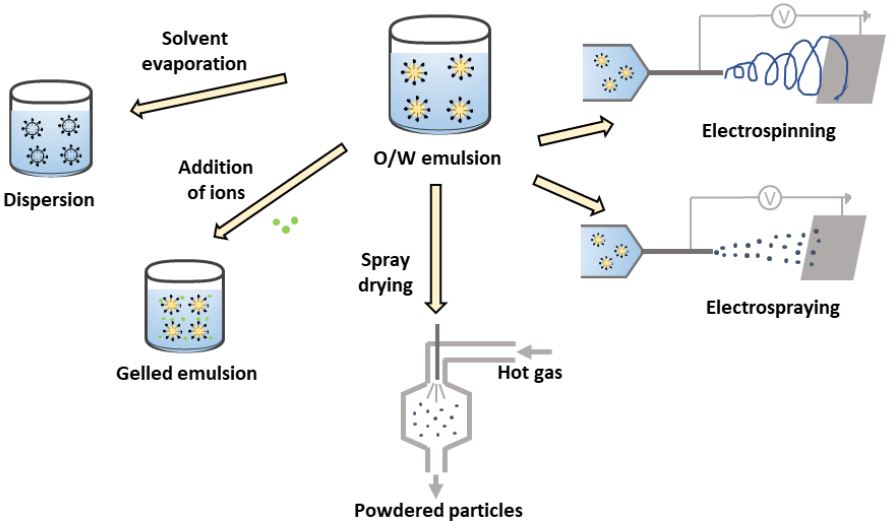

Figure 1.4. Most common techniques used to obtain particles from emulsion systems.

1.2.3. Encapsulation in lipid carriers

Lipid carriers include solid lipid nanoparticles (SLNs) and nanostructured lipid carriers (NLCs) (**Figure 1.5**). SLNs are spherical nanoparticles with a solid lipid core stabilized by amphiphiles, while in NLCs a part of the solid lipid core is replaced by a liquid lipid. In general, SLNs are less stable due to solidification/crystallization of the lipids followed by an increase in particle size and a decrease in the loading capacity.[36] The most common methods of preparation for SLNs and NLCs are high-pressure homogenization, solvent

emulsification/evaporation and ultrasonication. High-pressure homogenization is established as the technique for high-scale production of SLNs and NLCs, where the hydrophobic molecule to be encapsulated is first dissolved in the lipid (in its melted state) and then the fluid is moved with high pressure (100–2000 bar) into a homogenizer.[37] SLNs and NLCs have been extensively studied as carriers for fragrant molecules. Selected examples include the encapsulation of seven fragrances ((α)-amyl-cinnamal, cinnamal, cinnamyl alcohol, eugenol, geraniol, hydroxycitronellal, and isoeugenol) with five different lipids (petrolatum, candelilla, shea butter, C10-18 triglycerides, and cetyl palmitate) via a hot homogenization process coupled with ultrasound. This study showed that the loading capacity of SLNs depended both on the nature of the lipid and the fragrance and the octanol/water partition coefficient, *log* K_{ow}, of the fragrance is correlated with the encapsulation efficiency.[38] Two other examples showing the benefits of encapsulation are coming from Rodenak-Kladniew et al.[39] for the encapsulation of linalool in myristyl myristate, cetyl esters and cetyl palmitate SLNs with enhanced antiproliferative effects on cancer cell lines, while Bashiri et al.[40] encapsulated cinnamon essential oil in chitosan-coated cocoa butter NLCs that exhibited several advantages over the non-coated NLCs, including increased stability under storage conditions and higher encapsulation efficiency.

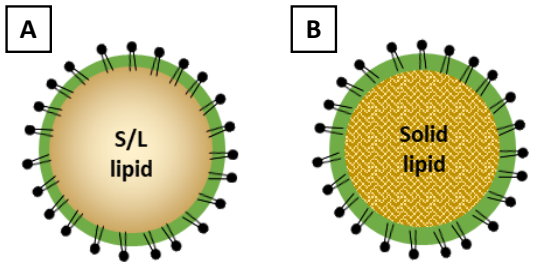

Figure 1.5. Schematic representation of lipid carriers. A: nanostructured lipid carrier; B: solid lipid nanoparticle.

1.2.4. Encapsulation in self-assembly colloidal systems

With the term "self-assembly" we describe the process of spontaneous, ordered arrangement of molecules under thermodynamic or kinetic driving forces. The interactions involved in the colloidal self-assembly process are long-range, non-covalent interactions and include van der Waals forces,

hydrophobic and electrostatic forces, hydrogen bonding, π-π aromatic stacking and metal coordination.[41] Many classes of natural and synthetic amphiphiles, including lipids, surfactants and polymers, can undergo self-assembly, giving rise to a variety of different phases briefly described in the next paragraphs, the main classes of which are: micelles, microemulsions, vesicles, liquid crystals, coacervates and encapsulation in unimolecular hosts,.

Micelles

A micelle is a thermodynamically stable colloidal aggregate of surface-active molecules, where its size and shape are determined by the geometry of the amphiphile. Schematic representation of a conventional spherical surfactant micelle or mixed surfactant micelle can be seen in **Figure 1.6**. Except of the conventional surfactant-based micelles, polymeric micelles can also be formed and they are divided into two main categories according to the force driving the self-assembly process: hydrophobically assembled micelles, that are usually composed of amphiphilic copolymers, and polyion-complex micelles, that are formed by charged polymer blocks.[42] The procedure for encapsulation in micelles is, in most cases, simply the direct dissolution of the amphiphile and a hydrophobic molecule (either together or separately) in an aqueous solvent. Micelle formation is induced by combining the two solutions to appropriate ratios. In the case of water-insoluble amphiphiles, the amphiphile and a hydrophobic molecule are dissolved in an organic solvent, and micelles are formed after a solvent removal step, e.g. for water-miscible organic solvents, after a dialysis step of the copolymer phase against water.[43] Polymeric micelles have been widely used for the encapsulation of fragrance molecules, including Pluronics,[44,45] Tween-80,[46] Poly(Ethylene Oxide-b-Lactic Acid) block copolymer,[47] or comb-like polymers.[48] It's worth mentioning the work of Grillo et al.[45] where the encapsulation properties of several essential oils and their pure terpenic compounds were investigated, using the nonionic micelles of Pluronic F127. For the investigation, mainly scattering techniques (SAXS and SANS) were used and it was shown that the oily molecule can be found in different compartments of the polymeric micelles: eucalyptol and methyl salicylate were found to be homogeneously distributed in the micelle polypropylene oxide core while for the rest of the oils the core was made by the pure oil surrounded by a first polypropylene oxide shell and a second polyethylene oxide shell.

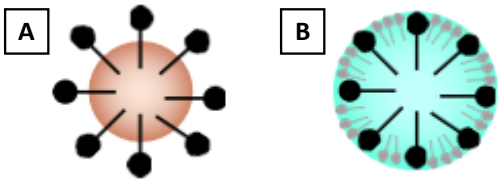

Figure 1.6. Schematic representation of A: spherical micelles and B: mixed micelles.

Microemulsions

The term microemulsion, also known as Winsor microemulsion, refers to dispersions of water, oil, and amphiphiles with droplet sizes up to 100 nm. Microemulsions are, in contrast to emulsions and nanoemulsions, thermodynamically stable systems and are formed spontaneously under specific conditions of composition, temperature and pressure. Microemulsions can be classified in four categories (**Figure 1.7**):

1. Winsor I microemulsion: two-phase system including a lower O/W microemulsion phase in equilibrium with an upper oil phase.
2. Winsor II microemulsion: two-phase system including a lower aqueous phase in equilibrium with an upper W/O microemulsion phase.
3. Winsor III microemulsion: three-phase system including a lower aqueous phase, an intermediate bicontinuous phase, and an upper oil phase.
4. Winsor IV microemulsion: one-phase system composed of a homogenous mixture of oil, water and surfactant.

The encapsulation of bioactive oils in microemulsion systems is covered in a review by Xavier-Junior et al..[49] Two examples of encapsulation of fragrances in microemulsion systems used Polysorbate 80 and ethanol or glycerol as the surfactant and co-surfactant respectively,[4,50] or Pluronic P123.[51]

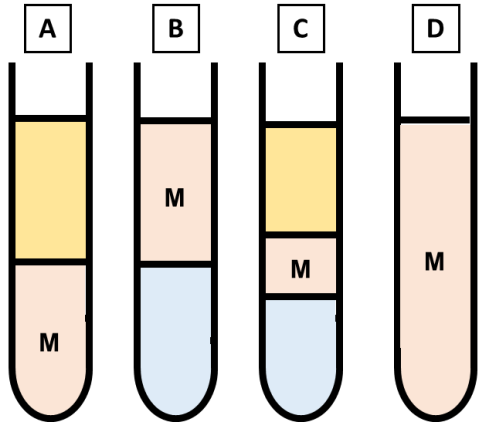

Figure 1.7. Schematic representation of the types of Winsor microemulsions. A: type I (two-phase system including a lower O/W microemulsion phase in equilibrium with an upper oil phase; B: type II (two-phase system with a lower aqueous phase in equilibrium with an upper W/O microemulsion phase); C: type III (three-phase system with a lower aqueous phase, an intermediate bicontinuous phase and an upper oil phase; D: type IV (single-phase system of a homogenous mixture of oil, water and surfactant).

Vesicles

Vesicular systems are composed by a surfactant bilayer bent into a 3D ring shape, usually enclosing the same solution as the one of the dispersed phase (**Figure 1.8**). Depending on their bilayer components' nature, vesicles can be named differently: *liposomes* when the bilayer is composed by lipids, *niosomes* when the building blocks are non-ionic surfactants, and *polymersomes* when the bilayer is composed by amphiphilic polymers. Vesicles can be further divided into five categories according to their size structure: small unilamellar vesicles (20 –100 nm), large unilamellar vesicles (100 nm – 1 μm), giant unilamellar vesicles (>1 μm), multilamellar vesicles, and multivesicular vesicles.[52] For the preparation of vesicles, the amphiphile has to be in its dry state and in contact with an aqueous phase where it's subsequently hydrated until the vesicular system is formed. Another common method of preparation is when the amphiphile is initially dissolved in an organic solvent which is then evaporated to produce a film on the container's surface; in a second step, addition of water leads to the hydration of the film and vesicles are produced with a broad size distribution. For the preparation of giant unilamellar vesicles, electroformation is used, where the amphiphile film is spread on a pair of electrodes followed by the addition of aqueous buffer and application of an electric current.[53] Vesicles have been extensively used as carriers for fragrances and selected examples include the use

of soy lecithin and cholesterol liposomes[54,55] as well as saturated and unsaturated phospholipid liposomes.[55]

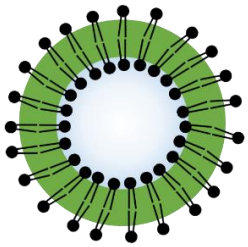

Figure 1.8. Schematic representation of a vesicular system.

Liquid crystals

Lyotropic liquid crystals (LLC) can be classified into three main categories: lamellar (L_α), cubic (Q_1) (or reversed cubic, Q_2) and hexagonal (H_1) (or reversed hexagonal, H_2) (**Figure 1.9**). LLCs differ from real crystals as they exhibit orientational, but no positional long-range order and they can be also called mesophases (intermediate states). LLCs are thermodynamically stable and formed by simply mixing the components in the appropriate concentration ratios. LLC nanoparticles, such as cubosomes or hexosomes, require more complicated preparation techniques, including high temperature dispersion, mechanical agitation, and the use of stabilizing polymers or hydrotropic solvents.[56] Several examples in literature show LLCs as carriers of fragrances, including phosphatidylcholine hexosomes and cubosomes encapsulating limonene,[57] a multiple emulsion with lamellar liquid crystals and different oils,[58] citrus sinensis essential oil L_α and H_1 structures with larvicide activity,[59] and trans-cinnamaldehyde in Q_1 and H_1 structures[60] or menthol in Q_2 phases[61] for transdermal delivery purposes.

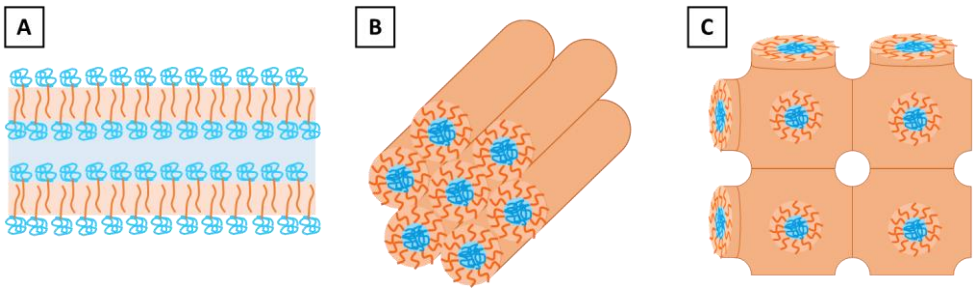

Figure 1.9. Schematic representation of the main categories of liquid crystals. A: lamellar (L_α) phases; B: hexagonal (H_1) phases; C: cubic (Q_1) phases.

Coacervates

With the term coacervation we define the liquid-liquid phase separation (LLPS) taking place in a solution of surfactants or polymers, with result to produce two immiscible phases that are in equilibrium: one phase is surfactant-rich while the other phase is diluted.[62] Depending on the relative densities, the surfactant-rich phase can be found as a dispersion of coacervate droplets. Different LLPS types are mentioned to take place in polymer solutions, including the solvent displacement process, coacervation by addition of a nonsolvent, nanoprecipitation and spontaneous emulsification, but all the types are describing the same physical phenomenon, known as the polymeric Ouzo effect. This phenomenon was described as a nonequilibrium, spontaneous emulsification process resulting from homogeneous liquid-liquid nucleation.[63,64] Coacervation can be classified in two main categories:

1. Simple coacervation: Here only one molecular species (one type of surfactant or polymer) takes place in coacervation (**Figure 1.10A**). The driving force of the formed coacervate is the dehydration of the surfactant chains, which depends on their amphiphilic nature and promotes the association of the molecules. A representative example is the "cloud point" temperature (CPT), a property of some non-ionic surfactants which leads to the formation of supramolecular aggregates that can scatter visible light and thus lead to a cloudy solution. This phenomenon is observed above a critical temperature. Other factors that can promote coacervation include the addition of salts, alcohols or co-surfactants. One example of simple coacervation can be found in the work of Bartolini et al., where the non-ionic amphiphilic graft copolymer PEG-*g*-PVAc was used for fragrance encapsulation above its cloud point in the presence of anionic and non-ionic surfactants.[65]

2. Complex coacervation: Here more than one molecular species takes place in coacervation. Usually in this type of coacervation the surfactants or polymers have opposite electrostatic charge (**Figure 1.10A**) and polysaccharides (most commonly gum arabic, chitosan, alginates, xanthan gum, and cellulose derivatives) and proteins (most commonly gelatin, albumin, whey protein, casein) are the leading class of complex coacervates.[66] Selected examples of complex coacervation

in fragrance and flavour encapsulation can be found with application in food industry, and eco- pesticides.[67–69]

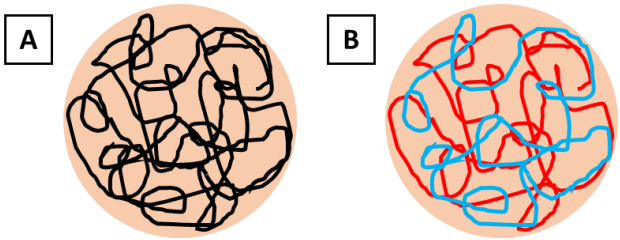

Figure 1.10. Schematic representation of the two types of coacervates. A: simple coacervate; B: complex coacervate.

Unimolecular hosts

Encapsulation of actives can be also achieved by their inclusion in unimolecular hosts. Such hosts can be multi-arm star-block copolymers or comb/graft polymers. Such polymers can fold in water to form structures with an outer hydrophilic shell and an inner hydrophobic core, able to accommodate insoluble molecules. Examples of fragrance encapsulation using multi-arm star-shaped polymers include the use of a polyester-polyacrylic acid block copolymer, loaded with several fragrances (*e.g.* geraniol, benzyl acetate).[70–72] Except of multi-arm star polymers, other polymeric architectures can be used for unimolecular encapsulation. Two examples are the linear poly(2-hydroxyethyl methacrylate-*co*-pyridyl disulfide ethyl methacrylate) copolymer and the poly ethylene glycol-polyvinyl acetate graft copolymer that have been reported to form single chain nanoparticles able to encapsulate hydrophobic fragrances.[73,74]

Another approach for encapsulation in unimolecular hosts is the one involving the use of cyclodextrins (CDs), the most widely employed host compounds. CDs are cyclic oligosaccharides, obtained by enzymatic conversion of starch, consisting in a variable number of glucose subunits joined by α-1,4 glycosidic linkages. Most common CDs are 6, 7 and 8 glucose units rings, and are named respectively as α-, β- and γ-cyclodextrins. CDs exhibit an asymmetric toroidal conformation with two openings of different sizes, and their alcoholic moieties pointing towards the exterior or the openings of the toroid. For that reason, the exterior is hydrophilic making CDs water soluble while the interior of the toroid is less hydrophilic and able

to host hydrophobic molecules. Selected examples of cyclodextrins on the encapsulation of perfume include the formation of α-, β- and γ-CD complexes with 13 different aroma molecules, where in all cases the formation of a 1:1 complex was observed and complexes of β-CD being the most stable.[75] CDs have been also shown to be effective in the stabilization, solubilization and delivery of other fragrances including allyl isothiocyanate,[76] tea tree oil,[77] and non-epicatechins from green tea.[78]

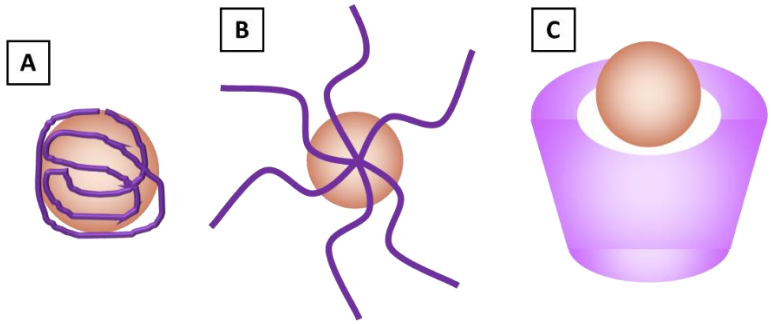

Figure 1.11. Schematic representation of unimolecular hosts. A: inclusion in single-chain polymer nanoparticle; B: inclusion in multiarm star copolymers; C: inclusion in cyclodextrins.

1.3. Encapsulation in this PhD thesis

No one can deny that perfume, essential oils and flavour encapsulation is a topic that drives a lot of attention from the scientific community, as evident from the plethora of publications on the subject and their numerous application fields. From the list of different encapsulation methods, we can spot their specific advantages or disadvantages that are distinguishing them. To select an encapsulation method, one should consider several aspects including how complicated a technique is during fabrication, if it includes or not the use of organic solvents and toxic reagents, if it requires more, or less friendly to the environment materials, evaluate the cost of the method according to the desired application or how easy it is to scale up, if needed. On the other hand, the properties of the obtained product from each fabrication method should be evaluated too, according to the aiming application: the product can exhibit different physicochemical properties, be in the liquid or solid state, being vulnerable under different conditions like pressure, light, temperature and undergo different release mechanisms.

This PhD thesis is part of the SAMCAPS (Self-assembled micro-capsules) project (grant agreement No 814100), that is a Marie - Skłodowska Curie industrial doctorate program in the Horizon 2020 framework. In this project we aim for a new perfume encapsulation technology for potential use in liquid home and personal care consumer products. Currently in the market, there is the need of new, sustainable, less time and energy consuming perfume encapsulation technologies where the active is not only limited to be released via pressure. Here, we are exploring the potentials of perfume encapsulation by taking advantage of the self-assembly properties of commercially available amphiphilic graft-copolymers, and others synthesized within the SAMCAPS network. Self-assembly is a simple and sustainable way to achieve encapsulation as it is a low energy and spontaneous process. Important aspect of this work is to investigate how the different polymers and the different single fragrance molecules, or PRMs affect the self-assembly and encapsulation, since industrial perfumes consist of tens or hundreds of PRMs.

Materials and Methods

A wide number of techniques have been used for the characterization of the self-assembled systems. In this chapter, the main techniques of characterization used in this work are reported.

2.1. Chemicals

Commercial polymers

Poly(ethylene glycol)-poly(vinyl acetate) graft copolymer (PEG-*g*-PVAc) produced by BASF. The polymer is characterized by a PEG/VAc weight ratio of 40/60, M_n = 13.1 kDa, M_w = 27.5 kDa (polydispersity index (PDI) = 2.1) and a degree of branching of 1−2%.[74]

Soluplus® or poly(ethylene glycol)-(poly(vinyl acetate)-poly(vinyl caprolactam)) graft copolymer (PEG-*g*-(PVAc-co-PVCL)) produced by BASF. The polymer is characterized by a PEG/PVAc/PVCL weight ratio of 13/34/53, M_w range of 90 – 140 kDa and cloud point temperature of 40 °C,[79] and grafting degree of 1.12 (units of PVAc-co-PVCL graft per PEG chain).

Polymers synthesized within the SAMCAPS network

Polymer S2, batch A (named S2A), is a PEG-*g*-(PVAc-co-PVCL) graft copolymer synthesized within the SAMCAPS project. The polymer is characterized by a PEG/PVAc/PVCL weight ratio of 15/25/60, M_w of 195 kDa, cloud point temperature of 21.5 °C and grafting degree of 1.46.

Polymer S2, batch B (named S2B), is a PEG-*g*-(PVAc-co-PVCL) graft copolymer synthesized within the SAMCAPS project. The polymer is characterized by a PEG/PVAc/PVCL weight ratio of 14/25/61, M_w of 193 kDa, cloud point temperature of 20.8 °C and grafting degree of 1.45.

Perfume raw materials

2-phenyl ethanol (PE, Sigma-Aldrich, ≥ 99.0% (GC), *log* K_{ow} = 1.36, M_W 122.16 g mol^{-1}); L-carvone (CAR, Sigma-Aldrich, ≥ 97%, (FCC, FG), *log* K_{ow} = 2.74, M_W 150.22 g mol^{-1}); linalool (LIN, Symrise, ≥ 97%, (FCC, FG), *log* K_{ow} = 2.97, M_W 154.25 g mol^{-1}); florhydral (FLO, Givaudan, ≥ 98%, *log* K_{ow} =

3.02, M_W 190.29 g mol^{-1}), β-citronellol (CIT, Sigma Aldrich, ≥ 95%, (FCC,FG), *log* K_{ow} = 3.30, M_W 156.27 g mol^{-1}); α-pinene (PIN, Sigma-Aldrich, ≥ 99.0%, *log* K_{ow} = 4.44, M_W 136.23 g mol^{-1}); R-limonene (LIM, Symrise, ≥ 95%, *log* K_{ow} = 4.57, M_W 166.26 g mol^{-1}); methyl anthranilate (MA, Sigma Aldrich, ≥ 98%, *log* K_{ow} = 1.88, M_w = 151.17 g mol^{-1}); iso-E super (IES, International Flavors & Fragrances, *log* K_{ow} = 5.12, M_w = 234.38 g mol^{-1}); habanolide (HAB, Firmenich, *log* K_{ow} = 5.53, M_w = 238.37 g mol^{-1}).

Other chemicals

Rhodamine-B isothiocyanate (mixed isomers, Sigma-Aldrich, MW 536.08 g mol^{-1}). D_2O (deuterium content > 99%); H_2O used in the rest of this work was Milli-Q grade (18.2 MΩ cm at 25 °C).

Industrial perfume accord: P&G, mixed of ~60 perfume raw materials with average *log* K_{ow} = 6.99.

Simplified liquid fabric enhancer (SLFE) (P&G, 5-11% cationic surfactant, di-fatty ester quaternary ammonium chlorides, <0.1% hydrochloric acid and formic acid, >88.9 – 94.9% H_2O). Cationic surfactant is present in SLFE in the form of vesicles. The SLFE matrix was used as it is, after preparation from the Procter and Gamble company process making. Two SLFE batches have been used: batch 1 (SLFE_A), containing one population of vesicles of ~0.2 μm diameter; batch 2 (SLFE_B), containing two populations of vesicles, one of ~0.2 μm and a second one of ~8 μm. **Table 2** summarizes the names and properties of the different SLFE matrices used.

Table 2.1. Properties of the different SLFE matrices used.

SLFE batch	SLFE name	Surfactant content (% w/w)	Vesicle diameter (μm)
1 (SLFE_A)	SLFE_A1	7	0.2
	SLFE_A2	11	0.2
2 (SLFE_B)	SLFE_B1	5	0.2, 8.0
	SLFE_B2	7	0.2, 8.0

2.2. Labelling of polymers

For confocal microscopy experiments, PEG-*g*-PVAc and Soluplus were covalently labelled with rhodamine-B isothiocyanate, according to a procedure described in a previous publication of the group.[65]

2.3. Sample preparation

Samples for phase diagrams of PEG-g-PVAc / PRM / water

PEG-*g*-PVAc/PE/water ternary phase diagrams in the concentration range 10 to 90% w/w, where PRM = 2-phenyl ethanol (PE), L-carvone (CAR) or α-pinene (PIN), were constructed by weighing the appropriate amounts of water, polymer, and perfume in a glass vial with an analytical balance. The viscous polymer was firstly molten at 50 °C in order to be more easily mixable with the other components of the system. Samples were vortexed until homogenization using a standard VELP vortex mixer at a maximum speed of 3000 rpm, and they were stabilized at 25 °C in an incubator for 14 days. The samples were kept in sealed vials and at a constant temperature in order not to affect the partition equilibrium of fragrance molecules between the liquid phase and the headspace, and thereby ensure a constant concentration in the formulations. In this thesis, concentrations will always be expressed as weight percent unless specified differently.

Soluplus polymer aqueous solutions

Samples with polymer contents ranging between 1% and 80% w/w in distilled or deuterated water were prepared to study Soluplus/water binary system phase behaviour. The appropriate amounts of polymer and water were mixed, and samples were vortexed until homogenization and stabilized at 25 °C in an incubator in sealed vials.

Soluplus / PRM aqueous solutions

For the preparation of samples containing PRMs and Soluplus, 50 mg of polymer were mixed with 900 mg of water and placed in the orbital shaker until fully dissolved. Following, 50 mg of one of the PRMs (PE, CAR, LIN, FLO, CIT, PIN or LIM) were added and the solution was vortexed for a few seconds until homogenisation. The samples were stored at 25 °C in an incubator, in sealed vials.

2.4. Scattering techniques

Small angle scattering

Small angle scattering is a widely used technique that allows the characterization of size, shape and orientation of colloidal structures in a sample. Small angle methods include the scattering of x-rays (small angle x-ray scattering – *SAXS*) or neutrons (small angle neutron scattering – *SANS*). Despite the fact that the physical mechanism of scattering differs in x-rays and neutrons, they can be described by the same theoretical principles, pointing out the differences between the two types of radiation. **Figure 2.1** illustrates the general setup for a small angle scattering experiment. During a small angle scattering experiment the source of radiation (x-rays or neutrons) emits a polychromatic beam which then passes through a monochromator that converts it into a narrow band of wavelengths. The incident beam, which is described by the wave vector $\vec{k_i}$ with modulus $2\pi/\lambda$, where λ is the wavelength, is focused on the sample through apertures. The scattered beam, which is described by the wave vector $\vec{k_s}$ is collected on a detector under the angle of 2θ.

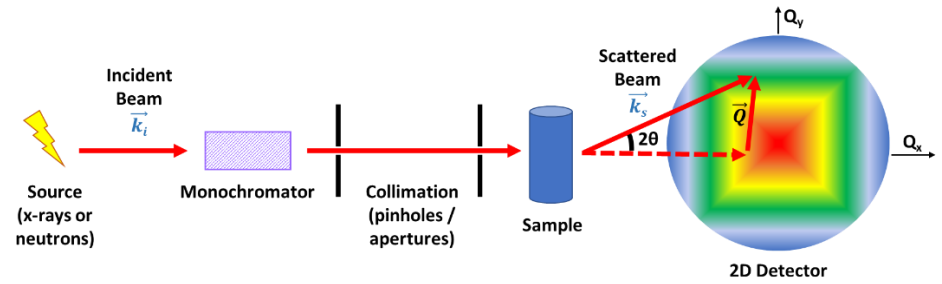

Figure 2.1. The general setup of a small angle scattering experiment.

The momentum transfer during the scattering process between the incident and the scattered beam is described by the scattering vector $\vec{Q}$:

$$\vec{Q} = \vec{k_s} - \vec{k_i} = \frac{4\pi}{\lambda}\sin\theta \qquad \textit{Eq. 2.1}$$

The scattering strength, or in other words, how strongly a sample scatters, can be described by the differential cross section, $d\sigma/d\Omega$ with dimensions of area per unit solid angle, $d\Omega$. The scattering intensity obtained from a sample in

the direction of the scattering vector $\vec{Q}$, in the solid angle dΩ, is related with the differential scattering cross section through the photon flux (Φ_0):

$$dI = \Phi_0 \frac{d\sigma}{d\Omega} d\Omega \qquad \textit{Eq. 2.2}$$

X-rays and neutrons exhibit some differences that need to be addressed in order to understand what type of samples can be studied and what information can be obtained in each case. The first difference between x-rays and neutrons is related to the wavelength of the beam. X-rays are characterized by a wavelength in the order of angstroms (around 1 Å), while for neutrons the wavelength can vary depending on the temperature of the neutrons used, between 0.01 and 3 nm. As the wavelength is related to the scattering vector Q (Eq. 2.1), increase in the wavelength leads to a decrease of Q which leads to the observation of larger scale objects. The most important difference between x-rays and neutrons is the mechanism by which the incident radiation interacts with matter. X-rays interact with the electrons surrounding an atomic nucleus, while neutrons interact with the nuclei. For x-rays, as electromagnetic waves, energy (E) is related with λ through Planck's equation:

$$E = hc / \lambda \qquad \textit{Eq. 2.3}$$

Where h is the Planck's constant and c the speed of light. On the other hand, neutrons have a finite mass of $1.674\ 10^{-27}$ kg that can't be neglected, and thus their kinetic energy needs to be taken into account:

$$E = h^2 / 2m\lambda^2 \qquad \textit{Eq. 2.4}$$

Thus, a neutron with a wavelength of 0.15 nm has energy equal to 36.4 meV, while the energy of a 0.15 nm x-ray photon is 8.2 keV. This is important for example in the case of sensitive, biological samples.

For x-rays, the differential scattering cross section arising from the interaction with electrons in the sample, is proportional to the electron cloud polarizability, α:

$$\frac{d\sigma}{d\Omega} = \frac{\pi^2 \alpha^2}{\lambda^4} \left(\frac{1 + \cos^2 2\theta}{2} \right) \qquad \textit{Eq. 2.5}$$

Eq. 2.5 is known as the Rayleigh ratio.

In the case of neutrons, the differential scattering cross section for an isolated atom is related with the scattering length, b:

$$\frac{d\sigma}{d\Omega} = b_j^2 \qquad \textit{Eq. 2.6}$$

The scattering length, b_j, is a characteristic parameter, different for each element. Variations of b can be caused by the variation of the nuclear spin direction with time, or by variations between isotopes of the same element. This is the reason why neutrons are isotope sensitive. For an ensemble of scatterers, the differential neutron scattering cross section can be described by the sum of their scattering lengths:

$$\sum_{ij} b_i b_j e^{i\vec{Q}\vec{R_{ij}}} \qquad \textit{Eq. 2.7}$$

Where R_{ij} is the distance between the scatterers. The differential cross section can be divided into two sums:

$$\frac{d\sigma}{d\Omega} = \langle b \rangle^2 \sum_{ij} e^{(i\vec{Q}\vec{R_{ij}})} + N\left(\langle b^2 \rangle - \langle b \rangle^2\right) \qquad \textit{Eq. 2.8}$$

Where N is the number of atoms in the scattering system. The first term in Eq. 2.8 is named coherent Scattering and it depends on the direction of Q, while the second term refers to the incoherent scattering that is uniform in all directions. Incoherent scattering is isotropic and in a small angle scattering experiment it contributes to the background signal. **Table 2.2** shows some examples of the coherent and incoherent scattering cross sections of common nuclei.

Table 2.2. Coherent and incoherent scattering cross sections of common nuclei.[80]

Nucleus	**σ_{coh} (10^{-28} m^2)**	**σ_{inc} (10^{-28} m^2)**
^{1}H	1.8	80.2
^{2}H	5.6	2.0
^{12}C	5.6	0.0
^{16}O	4.2	0.0

This phenomenon is particularly important for hydrogen, as the most abundant chemical in all matter. **Table 2.3** shows the scattering length density of selected common nuclei. As can be observed from **Table 2.3**, hydrogen isotopes are almost invisible to x-rays, while with neutrons, there is a large difference in scattering between ^{1}H and deuterium, ^{2}H. This difference between the hydrogen isotopes finds numerous applications over the years by scientists, as it offers the possibility of the so called "contrast-matching", a technique that is widely used in soft matter systems to "highlight" selected parts of larger aggregates.

Table 2.3. Neutron and x-ray scattering lengths for common atoms.[81]

Nucleus	**Neutron scattering length (10^{-12} cm)**	**X-ray scattering length (10^{-12} cm)**
^{1}H	-0.37	0.28
^{2}H	0.67	0.28
^{12}C	0.67	1.69
^{14}N	0.94	1.97
^{16}O	0.58	2.25

For x-rays, the scattering length density (SLD) of a given material can be calculated according to the equation:

$$SLD_{SAXS} = r_c \sum_{i}^{n} \frac{z_i}{V_{mol}} \qquad \textit{Eq. 2.9}$$

Where r_c is the Rayleigh constant, equal to 2.8 10^{-10} cm, z_i is the number of electrons in the i-th atom, n is the total number of atoms in the molecule and V_{mol} is the molecular volume. V_{mol} can be obtained from:

$$V_{mol} = M_W / dN_A \qquad \textit{Eq. 2.10}$$

Where M_w is the molecular weight of the molecule, d is the bulk density of the substance, and N_A is Avogadro's number. For neutrons, the scattering length density (SLD) of a given material can be calculated according to the equation:

$$SLD_{SANS} = \sum_i \frac{b_i}{V_{mol}} \qquad \textit{Eq. 2.11}$$

Where b_i is the scattering length of atom i in the molecule. The scattering intensity in a SAXS or SANS experiment results from the difference between the SLDs of the particles and the solvent. This difference in the SLDs is called "contrast", and it's calculated as:

$$\Delta\rho^2 = (SLD_{particle} - SLD_{solvent})^2 \qquad \textit{Eq. 2.12}$$

In a typical SAXS and SANS experiment, the scattered intensity I, is a function of the scattering vector Q. For monodisperse centrosymmetric scattering objects it can be given by the general expression:

$$I(Q) = \Phi V(\Delta\rho)^2 P(Q) S(Q) + B \qquad \textit{Eq. 2.13}$$

Where Φ is the particle volume fraction, V is the volume of one particle, P(Q) is a function called *form factor* and S(q) is a function called *structure factor* that both depend on Q, and B is the incoherent background, which is mainly important for neutron scattering.

The expression of the form factor is given by $\left\langle |F(Q)|^2 \right\rangle$, where F(Q) is a function related to the shape and size of the scattering object. For example, F(Q) for a spherical object is given by the expression:

$$F(Q) = \left[\frac{3(\sin(QR_p) - QR_p \cos(QR_p))}{(QR_p)^3} \right]^2 \qquad \textit{Eq. 2.14}$$

Where R_p is the radius of the spherical particle.

S(Q) accounts for the interaction potential in the system.[82] In very dilute, non-interacting systems, $S(Q) \sim 1$ and $I(Q) \propto P(Q)$. In higher concentrations, the interactions between particles can be describe by the expression:

$$S(Q) = 1 + \frac{N}{V}\int_0^\infty (g(R) - 1)\frac{\sin(QR)}{QR} 4\pi R^2 dR \qquad \textit{Eq. 2.15}$$

Where g(R) is the pair correlation function, which describes the interaction potential u(R) between the scatterers. When S(Q) < 1 the interactions between the particles are repulsive, while when S(Q) > 1 the interactions are attractive. An example of the contribution of P(Q) and S(Q) to the total scattering intensity obtained from a SAXS or SANS experiment is illustrated in **Figure 2.2**.

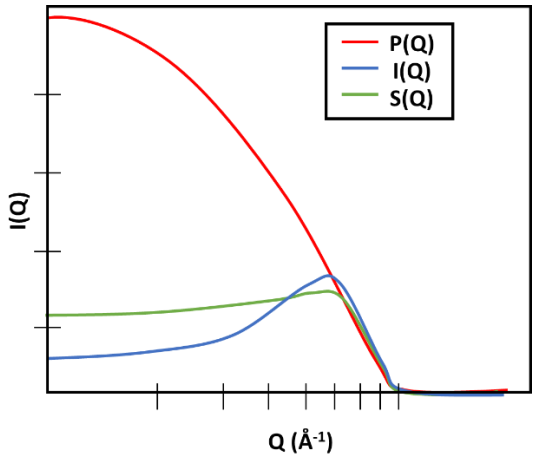

Figure 2.2. Example of the contribution of P(Q) and S(Q) to the total scattering intensity obtained from a SAXS or SANS experiment. P(Q): typical scattering pattern of the form factor of spherical particles; S(Q): an example of the structure factor when repulsive interactions are present between the particles; I(Q): the resulting scattering pattern obtained by combining P(Q) and S(Q).

In a scattering pattern, different regions can be identified as can be seen in **Figure 2.3** (typical P(Q) pattern for cylindrical scatterers), where the different spatial scales $2\pi/Q$ can give specific information for the studied system. At low Q values the so-called *Guinier region* can be found, a plateau region that contains information on the volume-square weighted size of the scatterers. At intermediate Q values, the *Debye region*, which is usually characterized by a slope proportional to Q^{-1} - Q^{-3}, and provides information on the shape of the structure (e.g. sphere, cylinder, disk etc.) is found. At higher Q values the *Porod region* can be identified, where information of the particle's surface can be extracted. The scattering intensity in this region is often proportional to Q^{-4},

but it can also take lower values, indicative of fractal-like structures in the sample.[83,84]

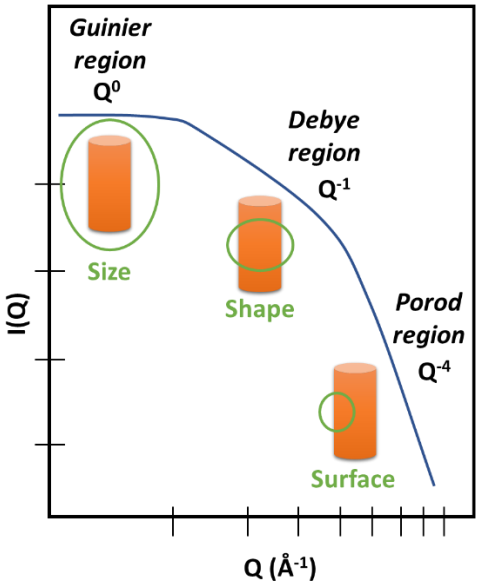

Figure 2.3. Schematic representation of the form factor of a sample with cylindrical shape scatterers, highlighting the different regions that can be found in a scattering pattern: Guinier region, Debye region and Porod region.

Small angle x-ray scattering (SAXS)

SAXS measurements were performed on a HECUS S3-MICRO camera equipped with a position-sensitive detector (OED 50 M) containing 1024 channels of width 54 μm. The X-ray source (GENIX-Fox 3D, Xenocs, Grenoble) operated at a maximum power of 50 W to provide an ultrabrilliant point microfocus Cu K*a* radiation (wavelength λ = 1.542 Å). The sample-to-detector distance was 281 mm. SAXS curves were obtained in the Q-range between 0.009 and 0.54 $Å^{-1}$. Samples were placed in either quartz Mark capillaries (liquids) or in a steel demountable cell using Kapton tape as windows (very viscous liquids or solids), and the cells were kept under vacuum during the experiments. All measurements were performed at the temperature 25 ± 0.1 °C (controlled by a Peltier element). All scattering curves were corrected for the empty cell contribution considering the relative transmission factor. Data reduction and modeling were performed with the NIST package

on the software IGOR Pro (WaveMetrics, Inc.)[85] and with the software SasView.

Small angle neutron scattering (SANS)

Small-angle neutron scattering data were collected at the ISIS neutron and muon source (Oxford, UK) on the ZOOM beam-line, with an observed Q-range of $2 \cdot 10^{-3}$ Å^{-1} < Q < 0.45 Å^{-1}. 2D data were radially averaged and standard reduction procedures (subtraction of empty cell and solvent contribution) were applied. The fitting procedure of the obtained scattering curves was performed with the NIST package of the software IGOR Pro (WaveMetrics, Inc.).[85]

Dynamic light scattering (DLS)

DLS measurements were performed on a Brookhaven BI9000-AT digital autocorrelator, equipped with a diode-pumped solid-state (DPSS) laser operating at λ = 532 nm (Torus, mpc3000, LaserQuantum, U.K.) and an avalanche photodiode (APD) detector positioned at 90°. Samples were placed in glass test tubes after filtering and immersed in a vat filled with decahydronaphtalene as a glass refraction index matching liquid. Experiments were performed at 25 °C; the temperature was controlled by a thermostatic bath with an accuracy of ±0.5 °C. Autocorrelation functions were analysed via the cumulant method to extract the diffusion coefficients D, which were then converted into hydrodynamic radii, assuming a spherical shape, through the Stokes–Einstein equation:

$$R_H = k_B T / 6\pi\eta D \qquad \textit{Eq. 2.16}$$

where R_H is the hydrodynamic radius, k_B is the Boltzmann constant, and η is the viscosity of the solvent.

2.5. Microscopy

Confocal laser scanning microscopy (CSLM)

The idea of confocal microscopy was pioneered in the 1950s by Marvin Minsky at Harvard University, during his effort to visualize neural networks of brain tissue. During the years, there has been an enormous raise in the usage of confocal microscopy, as this technique not only offers a remarkable

quality of images in a matter of seconds, but x-z sections provide three-dimensional (3D) visualization of micro-objects on the monitor. CLSM is becoming more and more popular, especially in the field cell biology that rely on imaging of living cells and tissues.

CLSM instruments are capable of obtaining images of serial sections in a thick sample, after a high intensity monochromatic laser beam is focused on a point of the sample. The 3D image is obtained by raster scanning of the specimen. The single points in the sample, upon excitation, can act as a secondary source of radiation. This phenomenon is widely known as fluorescence, the process where the electrons in the sample are excited by the laser beam and then undergo relaxation with spontaneous emission of light, of higher wavelength than the one of the beams. Samples in CLSM can be used when they naturally exhibit emission properties, or after a process called *labelling*, where they are exposed to an external fluorophore.

Figure 2.4 shows a general scheme for a CLSM microscope. The excitation source, the laser, emits coherent light which passes through a first pinhole, located in a confocal plane with the scanning point of the sample. A second circular pinhole is located before the detector. This is the main difference between CLSM and a classical wide-field fluorescence microscope. In a conventional fluorescence microscope, background fluorescence is emitted from the sample, especially when a sample is thick (>2 μm). CLSM is able to avoid the secondary emission coming from parts of the sample out of the plane of focus. The light is reflected by a dichromatic mirror and is then emitted on a defined focal plane of the sample. The secondary fluorescence emitted from points on the sample in focal plane passes back through the dichromatic mirror and is focused as a confocal point in the second pinhole, before reaching the detector. Fluorescence emission that comes from points above and below the objective focal plane, so out-of-focus planes, is not confocal with the pinhole and do not contribute to the final image. During a measurement, the distance between the sample and the objective varies producing a series of focal planes, and after collection of the individual slices the sample can be digitally reconstructed in a 3D manner.[86]

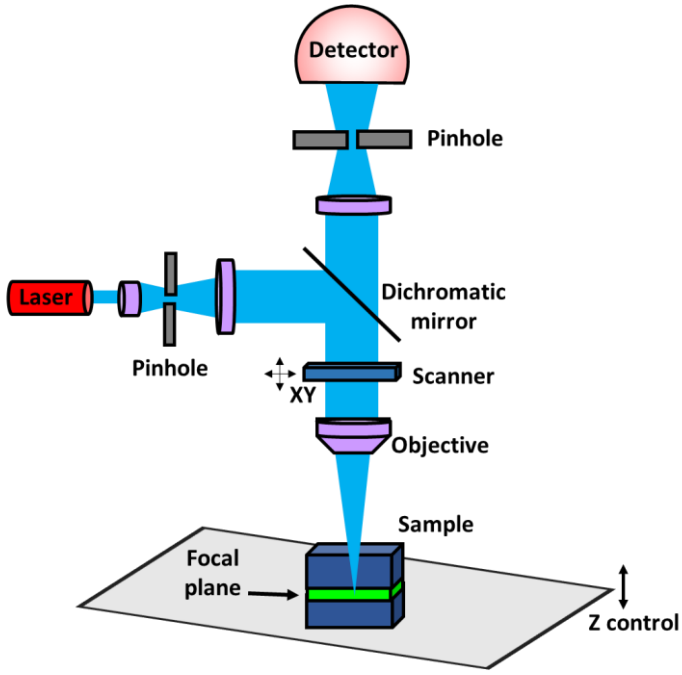

Figure 2.4. Schematic representation of a confocal laser scanning microscope.

Here, CLSM imaging was performed with a Leica TCS SP8 confocal microscope (Leica Microsystems GmbH, Wetzlar, Germany). Wells were used as sample holders (Lab-Tek Chambered 1.0 Borosilicate Coverglass System, Nalge Nunc International, Rochester, NY USA). The objective used was a 63× water immersion objective to image the samples. Rhodamine-B was used as a probe and it was excited at 561 nm with a DPSS laser. A Hybrid SMD detector was used for the fluorescence emission in the 571–600 nm range.

Confocal – Raman microscopy (CRM)

Confocal Raman Microscopy (CRM) combines the use of Raman spectroscopy with confocal optical microscopy and has driven much attention during the last decades as it exhibits a powerful tool to visualize minor structural characteristics of larger aggregates or biological samples with excellent resolution. As confocal microscopy allows for the retrieval of the 3D image of a sample, a combination with Raman spectroscopy enables the "chemical" imaging of discrete sample features. 3D maps can be generated with this method, by acquiring Raman spectra from numerous pixels within a certain area of the sample. Each pixel is then represented by its own spectrum

which provides its molecular constituents. A map can then be generated, that indicates the spatial distribution of certain molecular vibrations of the components. This technique has been widely applied for 3D imaging of cells, tissues and other biological samples where via high-resolution Raman maps, different components (like H_2O, polymers, nucleotides) are visible within complex multi-component samples.

Raman spectroscopy characterizes the molecular vibrations based on the inelastic scattering of photons. Raman scattering is only produced when a vibration produces a change in the polarizability of the molecule, which is more pronounced in symmetric vibrations. Light can be scattered when upon irradiation of a molecule, it generates a dipole moment, causing it to oscillate and emit light of the same frequency of the light beam. This phenomenon is widely known as *Rayleigh-scattering*. C.V. Raman and K.S. Krishnan back to 1920s observed, for the first time, lines additional to Rayleigh lines, whose frequencies had shifted by the magnitude of the vibrational and rotational frequencies of the molecules. The Raman scattering effect can be described as the inelastic scattering of photons on a molecule, through the equation:

$$\Delta E = E_f - E_i = \hbar\,(\omega_i - \omega_s) \qquad \textit{Eq. 2.17}$$

Where E_i and E_s is the initial and final energy of the molecule, respectively, and ω_i and ω_s the initial and final frequency of the photon, respectively. When the photon hits a molecule, a part of its energy is transferred to the molecule, which is then excited at higher energy levels. This energy transfer to the molecule can be translated into vibrational, rotational or electric energy. The difference between Raman and infrared spectroscopy, which very often are used as complimentary techniques, is the method of energy transfer between the photon and a molecule: In infrared (IR) spectroscopy the molecules are excited via absorption of IR radiation.

The Raman effect is described as the induction of an electrical dipole moment (p) upon placement of a molecule in an electric field E. The induced electrical dipole moment can be split into three parts that are functions of the vibrational frequency of the incident beam (ν_0) and the one of the molecules (ν_ν).

$$p = \alpha E_0 \cos(2\pi v_0 t) + \frac{1}{2}\alpha' \cos(2\pi(v_0 + v_v)t) + \frac{1}{2}\alpha' \cos(2\pi(v_0 - v_v)t)$$

Eq. 2.18

Where α is the time independent part of the polarizability, α' is the time dependent part of the polarizability and E_0 is the initial electric field. The first term of Eq. 2.18, which only depends on ν_0, represents the Rayleigh scattering. The second and third part of the equation, that depend on the incoming frequency, represents the so-called *Anti-Stokes scattering* and *Stokes scattering* respectively. **Figure 2.5** represents the energy transition related to the Rayleigh, Stokes and Anti-Stokes. Rayleigh scattering is not accompanied by any loss of energy. During Raman scattering (Stokes and anti-Stokes), an event of energy loss occurs, where the incoming photon is excited via absorption and another photon is scattered, that has a lower or higher energy than the initial one, for Stokes and anti-Stokes scattering respectively.

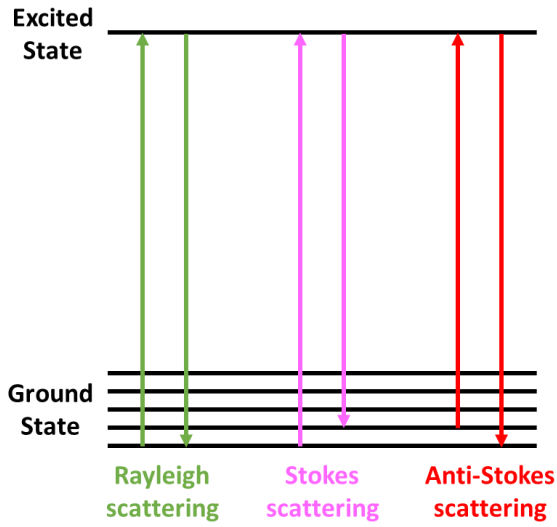

Figure 2.5. Schematic representation of the energy transitions during Rayleigh, Stokes and Anti-Stokes scattering. Upward arrows represent the excitation process, and the downward arrows represent the scattered radiation.

As explained earlier, confocal laser scanning microscopy uses fluorescence emission as probe for imaging, while during a confocal Raman microscope measurement, molecular vibration modes are determined providing the chemical fingerprint of the sample. Raman microscopy has some advantages

compared to fluorescence microscopy. Firstly, a sample does not need to be externally labelled with a fluorophore in order to be visible under a Raman microscope, like is needed in CLSM imaging if a sample is not naturally fluorescent. Additionally, during the fluorescence emission process, the sample, in order to be excited it needs to absorb light within a specific wavelength range. On the other hand, Raman is not a resonant process and thus can take place at different frequencies of the light. In the case of fluorescence presence in the sample desired to be analysed with Raman microscopy, it can be avoided by using a lower energy / higher wavelength excitation laser.[87–89]

Here, Raman analysis and mapping were performed on a Renishaw InvIa Qontor confocal MicroRaman system equipped with 785 nm (solid state type, IPS R-type NIR785, 100 mW, 1200 l/mm grating) and 532 nm (Nd:YAG solid state type, 50 mW, 1800 l/mm grating) lasers, front illuminated CCD camera (256x1024 px, working temp. −70 °C) and research grade Leica DM 2700 microscope equipped with LWD 50× (NA 0.55, WD 8.0 mm), LWD 100× (NA 0.75, WD 4.7 mm) and 100× (NA 0.85, WD 0.27 mm) objectives.

Samples were prepared by placing a small amount of product between two microscopy glass slides. References for pure compounds were collected using the 785 nm excitation wavelength for Soluplus and 532 nm excitation wavelength for the PRMs. Raman spectra were recorded in the 300-3700 cm^{-1} wavenumber range using the extended range mode. 2D maps were acquired in static range measurement mode by using the LWD 50× objective and the 532 nm laser. Acquisition times varied between 10 and 40 s (to improve signal-to-noise ratio), acquiring a single scan. Raw data were processed using Renishaw software WiRE v.5.2 for baseline correction, peak fitting and maps generation.

Optical microscopy

Optical images were collected with an inverted optical microscope (Diaphot 300, Nikon) equipped with a digital camera (Nikon Digital Sight DS-U1). The objective magnification used was 20×. For the image analysis the software ACT 2U by Nikon was used.

Fluorescence microscopy

Fluorescence microscopy imaging at the Procter&Gamble Brussels Innovation Centre was performed using a Zeiss Axio Imager A1 upright microscope (Zeiss Ltd., Germany) equipped with an Axiocam 305 color camera. All observations were carried out with objective magnification ×40. The excitation wavelength for the rhodamine-b labelled copolymers was around 560 (±40) nm, and the emission wavelength was around 640 (±75) nm using a Zeiss 45 Filter Set. For tracking of the PRM methyl anthranilate, the Zeiss Filter Set 02 has been used, with excitation wavelength around 300-400 nm, and a long-pass emission filter of 420 nm. For image acquisition, the software AxioVision SE64 has been used.

2.6. Differential Scanning Calorimetry (DSC)

For the DSC measurements a TA Q2000 (New Castle, USA) was used. Steel pans were used as sample holders containing 15 - 20 mg of sample. The analysis was performed in heating mode between −80 °C and 25 °C, using a 0.5 ºC/min heating ramp. For the calculation of the free water content (FWC) of each sample the following formula was used:

$$FWC = \frac{\Delta H_{f,sample} . m_{sample}}{\Delta H_{f,water} . m_{water}} \times 100 \qquad \textit{Eq. 2.19}$$

where $\Delta H_{f,sample}$ and $\Delta H_{f,water}$ are the enthalpy of fusion (J/g) of water in the sample and of pure water, respectively. m_{sample} and m_{water} are the weight of the sample and the nominal amount of water in the sample respectively (in g). $\Delta H_{f,sample}$ was obtained by integrating the bands in the −20 °C – +5 °C temperature range. $\Delta H_{f,water}$ was obtained from the literature.[90]

2.7. Rheology

Rheological measurements were carried out on a TA DHR3 rheometer that works in controlled shear stress mode, using a plate-plate geometry (Flat Plate 40 mm or 60 mm diameter) and a Peltier system for temperature control. All the measurements were carried out at 25 °C. The gap between the plates at zero radial position was always maintained equal to 500 μm. The cell was closed by lowering the head to the measuring position in the z-axis force-

controlled mode; flow curves were collected by measuring the viscosity values under the application of a shear rate logarithmic ramp in the range 1-10^3 s^{-1}.

2.8. Nuclear magnetic resonance (NMR)

^{1}H-NMR, {^{1}H-^{13}C}-HSQC, {^{1}H-^{1}H}-NOESY and {^{1}H-^{1}H}-COSY experiments were performed by means of a Bruker AVANCE spectrometer operating at 400 MHz (^{1}H) using the peak of the residual protonated solvent as internal reference. Samples of pure Soluplus were prepared in DMSO-d_6 ^{1}-HNMR. Spectra of pure PRMs were aquired in $CDCl_3$. ^{1}H-^{1}H-NOESY of the samples with polymer (PEG-*g*-PVAc or Soluplus) and PRM were acquired in D_2O. NOESY experiments were conducted with mixing times of 200 and 500 ms, 512 experiments in the F1 dimension with 16 scans for each of the increments on t_1 and a sweep width of 15 ppm.

2.9. Tensiometry

Measurement of the surface tension of Soluplus aqueous solutions was done with a KSV Sigma 70 static tensiometer (accuracy 0.1 mN/m) allowing an automatic determination of the CMC by using the duNouy ring. The temperature was constant at 25.0 ± 0.5 °C in a controlled temperature vessel. CMC was measured by water dilution of a concentrated polymer solution.

2.10. Performance tests

Performance tests evaluate the benefit consumers will perceive when using a product and they are designed to simulate real conditions. In a first step, perfume is encapsulated using the amphiphilic graft-copolymer self-assembly approach. Then, capsules were formulated in a simplified liquid fabric enhancer (SLFE) formulation simulating production plant conditions. In the last step, capsules were applied to fabrics using two protocols: a) the so-called forced deposition test, and b) real washing machine conditions. Perfume capsules deposition and performance was evaluated using headspace gas chromatography – mass spectrometry (GC-MS) analysis at two touchpoints: on dry fabrics after 24- and 48-hours following deposition. The fabrics were further analysed via headspace GC-MS at the two touchpoints:

- DFO-24 (Dry Fabric Odor): Fabrics are analysed after line-dried in a closed room for approximately 24 hours

- DFO-48: Fabrics are analysed after line-dried in a closed room for approximately 48 hours

Formulation of perfume capsules in SLFE

Formulations and wash test solutions were always prepared the same day of the wash test. Products were prepared by dissolving 5 mg of each polymer (Soluplus, S2A or S2B) in 990 mg of SLFE. The sample was vortexed for few seconds until fully dissolved. Following, 5 mg of the selected PRM or industrial perfume accord were added, and the samples were again vortexed for 30 s until homogenisation. Reference solution was prepared by dissolving 5 mg of PRM or industrial perfume in the SLFE (without polymer addition).

Forced deposition tests

The forced deposition tests evaluate the performance of the capsules without taking into account deposition in the wash. Knitted cotton fabrics were cut in square pieces of 15 g each. The products prepared in the previous step were diluted 100 times with tap water to prepare the wash test solution, in order to mimic the washing machine conditions. On each piece of fabric, 10 g of wash solution were spread using a plastic pipette. At the end of the forced-deposition procedure, the fabrics were line dried and analysed at the desired touchpoint.

Washing machine tests

Washing machine tests are designed to simulate consumer habits. For each wash test, a washing machine (ex Miele) was loaded with 3 kg fabrics (knitted cotton fabrics and polyester fabrics, 80/20 w/w ratio). During the wash test, the fabrics were washed at 40 °C and with 1200 rpm spin speed with 79 g of powder detergent. A dosage of 35 g of the test wash solution was added in the appropriate dispenser before the last rinse step, together with 500 ml water to ensure there is no residue left. At the end of the cycle, the fabrics were line dried and analysed at the desired touchpoint.

Perfume evaluation on fabrics: Headspace gas chromatography – mass spectroscopy (GC/MS)

To evaluate the performance of the SLFE after fabric treatment, the headspace above the fabric was analysed using solid phase micro-extraction (SPME) headspace GC/MS. The fabrics were cut into squares of 4 x 4 cm and were transferred into 25 ml headspace vials, where they equilibrated for 10 minutes at 65°C. The headspace above the fabrics was sampled via SPME (50/30 µm DVB/Carboxen/PDMS) for 5 minutes and the SPME fiber was subsequently on-line thermally desorbed into the GC. The analysis by GC/MS was in full scan mode. The total perfume headspace response and perfume headspace composition was determined.

Results and Discussion

This PhD thesis is dealing with amphiphilic graft copolymers as self-assembled, perfume encapsulation systems with potential use in complex industrial liquid formulations. As explained in detail in the Introduction of this thesis, complex liquid matrices used in industrial formulations are in principle water-based and their main components are polymers and/or surfactants, active molecules like perfumes and other minors (e.g. pH adjusters). Here, in order to fully obtain the knowledge and understanding of the encapsulation process, a bottom to top approach is being followed, starting from simpler to more complex liquid matrices. Simplified liquid matrices include the polymer of interest and one PRM in water medium. Studies in more complex liquid matrixes were extended in industrial model formulations including the polymer of interest and the PRM in a simplified liquid fabric enhancer (SLFE). Commercial polymers, and polymers synthesized within the SAMCAPS network were used for perfume encapsulation, that are based on two main structures: PEG-*g*-PVAc or PEG-*g*-(PVAc-*co*-PVCL).

The Results and Discussion section of this PhD thesis is divided in four main parts:

1. Part 1: Ternary phase diagrams of PEG-*g*-PVAc aqueous solutions in the presence of three common natural fragrances
2. Part 2: Investigation of the self-assembly properties of Soluplus or PEG-*g*-(PVAc-*co*-PVCL) aqueous solutions
3. Part 3: Soluplus as an encapsulating agent for fragrances in aqueous media
4. Part 4: Self-assembly, perfume encapsulation and performance of PEG-*g*-(PVAc-*co*-PVCL) copolymers in SLFE

Results and Discussion: Part 1

Ternary phase diagrams of PEG-*g*-PVAc aqueous solutions in the presence of three common natural fragrances

Poly(ethylene glycol)-*graft*-poly(vinyl acetate) or PEG-*g*-PVAc is an amphiphilic comb-like copolymer with low grafting density that has been intensively studied by our research group in the past. PEG-*g*-PVAc was shown to self-fold in water into single-chain nanoparticles (SCNPs) for concentrations up to 10%, capable of solubilizing small hydrophobic molecules.[91] The studies were later extended, and the binary system PEG-*g*-PVAc/water was investigated in the 10–90% range. Experimental results, that were in full agreement with simulations, demonstrated a progressive structuration of the SCNPs into bicontinuous phases.[92] In a later extend, the ability of PEG-*g*-PVAc to undergo liquid-liquid phase separation (LLPS) in surfactant formulations was investigated. Findings showed that the formation of micro-domains by LLPS was driven by the polymer/surfactant interactions and by the salting-out effect, produced by electrolyte addition. The morphology of the micro-domains depended on the ratio between non-ionic and anionic surfactants, but also the free water content in the system. The ability of the micro-capsules to encapsulate hydrophobic or hydrophilic molecules and then release them with water dilution was investigated. The hydrophobic poly(dimethylsiloxane) bis(3-aminopropyl) terminated and the hydrophilic (Z,Z)-disodium distyrylbiphenyl disulfonate (whitening agent used in laundry liquid detergents) were successfully encapsulated.[65]

In this chapter we discuss the investigation of the phase behaviour of PEG-*g*-PVAc aqueous solutions in the presence of three natural fragrance molecules, commonly used in home and personal care products: 2-phenyl ethanol (PE), L-carvone (CAR) and α-pinene (PIN). The three selected natural fragrances exhibit similar bulkiness, but different water affinities as expressed by their octanol/water partition coefficients (*log* K_{ow}). α-pinene is the most hydrophobic (*log* K_{ow} = 4.44), L-carvone has intermediate hydrophobicity (*log*

K_{ow} = 2.74, solubility in water = 0.4% w/v), and 2-phenyl ethanol is the most hydrophilic (*log* K_{ow} =1.36, solubility in water = 2% w/v). The ternary systems were investigated in the 10-90% concentration range in all the possible ratios, to elucidate the effect of the actives' hydrophobicity and/or affinity for the polymer blocks on the polymorphism of PEG-*g*-PVAc. Knowledge of the ternary phase diagrams provides useful practical insights for consumer good formulators, such as the correct dilution path e.g., to avoid the formation of excessively viscous liquid-crystal phases. Moreover, understanding the polymer behaviour toward cosolvents and nonsolvents is of paramount importance to predict its properties as an emulsifier and formulation stabilizer, and to best apply it in everyday life products. For our investigation of the polymorphism of PEG-*g*-PVAc, DLS, SAXS, NMR spectroscopy, and confocal laser scanning microscopy were the main experimental techniques used.

The Gibbs phase diagrams for the ternary systems PEG-*g*-PVAc/PRM/water (A = 2-phenyl ethanol; B = L-carvone; C = α-pinene) at 25 °C and the 10-90% concentration range can be seen in **Figure 3.1**. The three phase diagrams were first created by visual inspection of the samples. Starting from the PEG-*g*-PVAc/PE/water system, three monophasic sample regions were observed. The biggest of the three regions, which dominates the phase diagram, was a continuous isotropic liquid region of varying viscosity, extending from the polymer/water binary axis toward the polymer/PE axis. A similar region was observed in the PEG-*g*-PVAc/CAR/water diagram, but its extension was limited to a smaller area. Both phase diagrams included a central region of viscous birefringent liquid, which identified to be Lamellar liquid crystalline phases (L_α), as it will be discussed later in detail. Following a dilution line from the birefringent phase toward the H_2O corner, a small region of milky liquid, identified, as will be discussed later, to be a micro-capsule suspension (named "D" region) was observed. The PEG-*g*-PVAc/PIN/water system did not present any single-phase areas. The discussion will be focused on the specific regions observed in the phase diagrams, comparing the effect of the different fragrances.

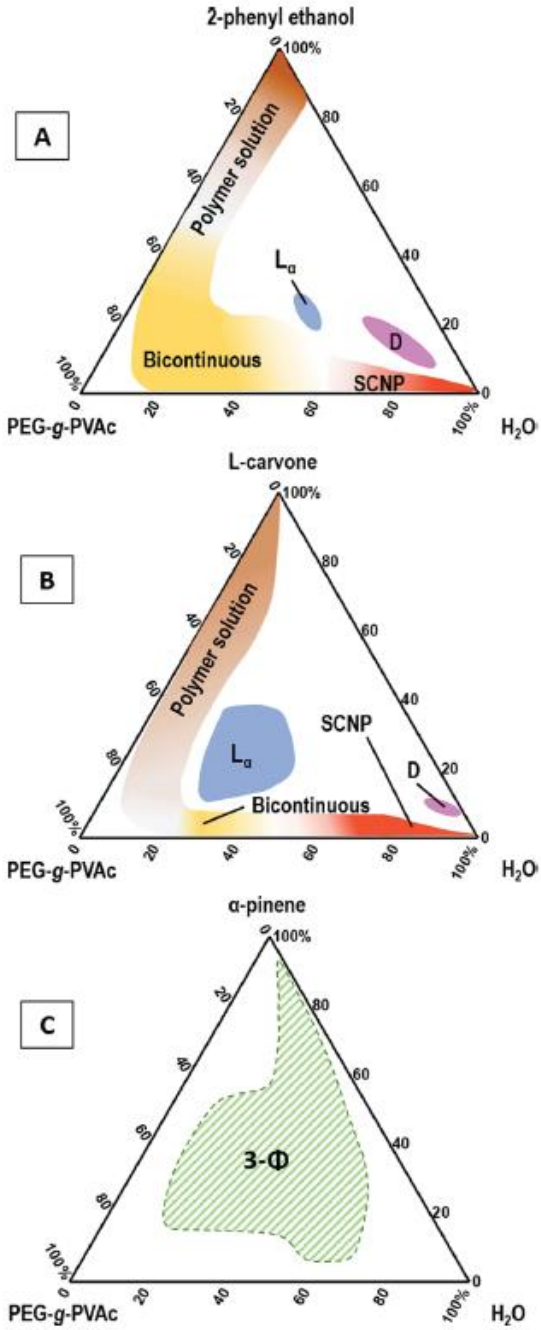

Figure 3.1. Gibbs ternary phase diagrams for the PEG-*g*-PVAc/PRM/water ternary systems at 25 °C: (A) 2-phenyl ethanol, (B) L-carvone, and (C) α-pinene. "SCNP" = single-chain nanoparticles; "D" = micro-capsule suspension; "L_α" = lamellar mesophases; "3-Φ" = three-phase region. The white areas represent two-phase regions.

3.1. PEG-*g*-PVAc/PRM/water systems in the highly dilute regime

Our analysis started from the highly diluted regime of the phase diagram, and selected samples containing 2 or 5% polymer and 0.5 or 1% perfume respectively, were investigated by means of DLS (results can be found in Table 1 of Paper I) and SAXS. SAXS patterns of the samples are shown in **Figure 3.2**.

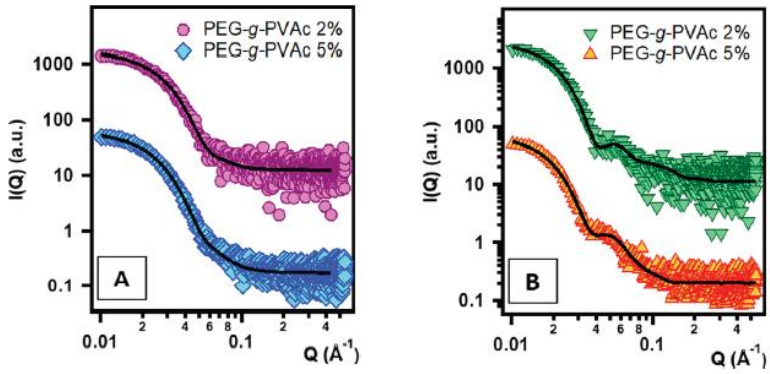

Figure 3.2. SAXS curves obtained for samples in the highly dilute regime of the PEG-*g*-PVAc/PRM/water ternary systems, with (A) 2-phenyl ethanol and (B) L-carvone. Polymer concentrations are indicated in the figure legends. Markers represent experimental points, while the solid lines represent the best fits to the models discussed in the text. Curves were offset along the y axis for presentation purposes.

DLS analysis of the samples containing 2-phenyl ethanol yielded hydrodynamic radii in close agreement with those measured previously for the polymer SCNPs (R_H = 112 Å for 2% polymer in water).[91] The SAXS pattern of the system with 2% polymer and 0.5% perfume (**Figure 3.2A**) was fitted with a sphere form factor (Eq. 3.1) and Schulz radii distribution (equation S3, Paper I) and the results are summarised in **Table 3.1.**

$$P(Q) = \frac{A}{V}\left[\frac{3V(\Delta\rho)(\sin(QR) - QR\cos(QR))}{(QR)^3}\right]^2 + B \qquad \textit{Eq. 3.1}$$

Where A is a scale factor, V and R are the volume and radius, respectively, of the scattering objects, $\Delta\varrho$ is the contrast (difference between the SLDs of the particles and the solvent), and B is the instrumental background. For a detailed description of the model's mathematical expressions and parameters see Supporting Information of Paper I. Fitting results gave a 66 Å radius, roughly

the same size found for the pure polymer SCNPs. The scattering length density (SLD) of the spheres obtained from the fitting procedure was 10.2×10^{-6} Å^{-2}, which is consistent with an average of the values for PEG, PVAc, and PE. The SLD values of pure components can be seen in Table S3, Paper I. This result indicates a complex mixing of the three species, suggesting the self-folding of the polymer into the SCNP structure embedding the perfume. The structure remains as it is when increasing the polymer content to 5% and the perfume to 1%.

Table 3.1. Obtained parameters after fittings of SAXS patterns in Figure 3.2A with a sphere form factor: R = sphere radius; σ = Schulz polydispersity of R; SLD_{sphere} = scattering length density of the sphere.

Sample composition	**PEG-*g*-PVAc 2%, PE 0.5%**	**PEG-*g*-PVAc 5%, PE 1%**
R (Å)	66	71
σ	0.22	0.24
SLD_{sphere} (10^{-6} Å^{-2})	10.2	10.2

Table 3.2. Obtained parameters after fittings of SAXS patterns in Figure 3.2B with a core-two shell sphere form factor: R_c = core radius; σ = Schulz polydispersity of R; SLD_{core}, SLD_{s1}, and SLD_{S2}= scattering length densities of the core, first shell, and second shell, respectively; t_1 and t_2: thickness of the first and second shell, respectively; R_{tot}: radius of the core−shell particle (not a fittings parameter).

Sample composition	**PEG-*g*-PVAc 2%, CAR 0.5%**	**PEG-*g*-PVAc 5%, CAR 1%**
R_c (Å)	43	45
σ	0.23	0.31
SLD_{core} (10^{-6} Å^{-2})	8.99	8.99
SLD_{s1} (10^{-6} Å^{-2})	10.5	10.5
SLD_{S2} (10^{-6} Å^{-2})	9.51	9.51
t_1	16	40
t_2	55	46
R_{tot} (Å) = $R_c + t_1 + t_2$	114	131

In the presence of L-carvone, larger radii were obtained from DLS and SAXS measurements than those in the presence of PE. The SAXS patterns in the presence of CAR were fitter with a core−two shell sphere form factor according to Eq. 3.2:

$$P(Q) = \frac{A}{V_s}\left[\frac{3V_c(\rho_c - \rho_{s1})\,j_1(QR_c)}{QR_c} + \frac{3V_{s1}(\rho_{s1} - \rho_{s2})\,j_1(QR_{s1})}{QR_{s1}} + \frac{3V_{s2}(\rho_{s2} - \rho_{solv})\,j_1(QR_{s2})}{QR_{s2}}\right]^2 + B$$

Eq. 3.2

Where the subscripts have the following meanings: c = core, s_1 = first shell, s_2 = second shell, solv = solvent; ϱ is the SLD. $j_1(x) = (\sin(x) - x\cos(x))/x^2$. $R_{s1} = R_c + t_1$ and $R_{s2} = R_c + t_1 + t_2$, with t the thickness of each shell; $V_i = (4\pi/3)R_i^3$. For a detailed description of the model's mathematical expressions and parameters see Supporting Information of Paper I. Fitting results are summarized in **Table 3.2**. For the core, the yielded SLD value was 8.99×10^{-6} Å^{-2}, close to the SLD of pure carvone ($8.84 \times 10{-}6$ Å^{-2}). On the other hand, the first shell (inner shell) had an SLD value of 10.5×10^{-6} Å^{-2}, consistent with the one of pure PVAc, while the second shell (outer shell) SLD was 9.51×10^{-6} Å^{-2}, indicative of highly hydrated PEG moieties. In this case, results suggest encapsulation of carvone in the SCNP core, leading to the swelling of the structure. These results confirm that both perfumes are encapsulated in the SCNPs, but with different arrangement of the PEG and PVAc chains.

To confirm the different type of encapsulation in the SCNPs for PE and CAR, further 2D {^{1}H−^{1}H} NOESY correlation NMR experiments were performed to give insights on the PRM-polymer interactions.[93–95] For this purpose, samples with 5% polymer and 1% PRM were prepared in D_2O. SAXS experiments on these samples confirmed that replacing H_2O with D_2O did not significantly affect the self-assembled structures (Figure S1, Supporting Information, Paper I). The proton NMR spectra of the PEG-*g*-PVAc/PE/ water mixture and PEG-*g*-PVAc/CAR/ water mixture are shown in Figure S2 and Figure S3, Supporting Information, Paper I. PE shows two well-resolved bands in its NMR spectrum, in the 7.25−7.40 and 2.80−2.90 ppm regions. CAR shows its main bands in the 1.00−2.50, 4.70−4.90 and 6.85 ppm regions. On the other hand, PEG-*g*-PVAc has well-distinct resonances for the

two blocks at 3.60 ppm (PEG segment) and at 4.80−5.20 and 1.50−2.30 ppm regions (PVAc segment). {^{1}H−^{1}H} NOESY correlation maps for the two samples can be seen in **Figure 3.3**. For PE, in-phase cross-peaks are present between all the characteristic bands of PE and the ones of both PEG and PVAc segments. This is a further indication that PE interacts with both PEG and PVAc without preference for one of the two. In this way, we confirm that 2-phenyl ethanol is embedded in the polymer matrix of the SCNP. For CAR, the main bands of the spectrum almost completely overlap with the PVAc polymer signals, and the only band that can be used as probe is the resonance at 6.85 ppm, related with the = CH− proton of the carvone ring. Interestingly, no clear cross-correlation of this signal with any band of the polymer is observable in the NOESY map, meaning that no specific and strong interactions are present between the polymer and CAR. This observation is a further indication of the preferential location of L-carvone in the core of the SCNP, with minimum interactions between the PRM and the polymer's segments or water.

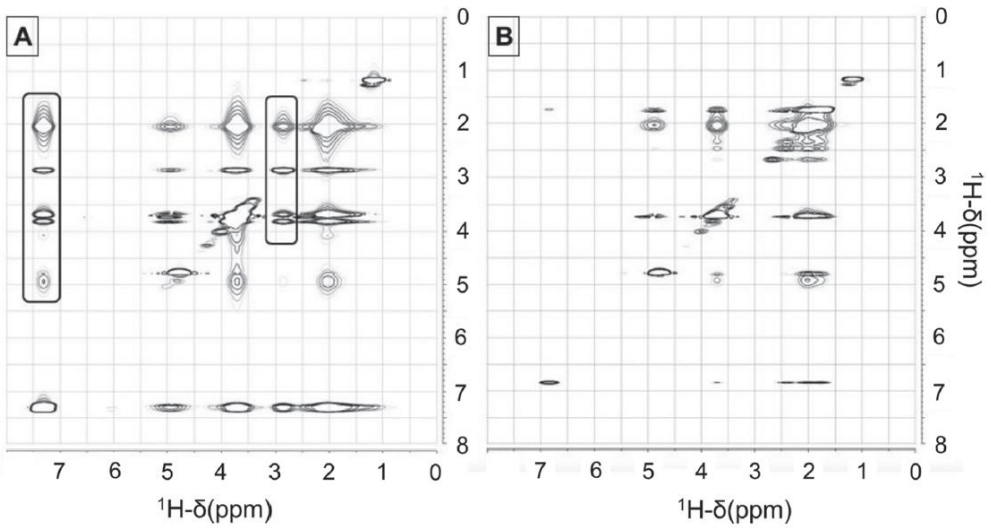

Figure 3.3. {^{1}H−^{1}H} NOESY correlation maps for (A) PEG-*g*-PVAc (5%)/PE (1%)/D_2O and (B) PEG-*g*-PVAc (5%)/Car (1%)/D_2O.

The highly diluted regime of the phase diagram was also investigated using pulse-gradient stimulated echo (PGSTE) NMR experiments. The experiments were performed in collaboration with Prof. Sergio Murgia at the University of Cagliari, Sardinia. With those experiments we would be able to extract the self-

diffusion coefficients of the different species present in the samples. The samples used for the PGSTE experiments were selected across a dilution line extending from the H_2O corner of the phase diagram up to around 30% polymer. The position of the selected samples in the phase diagrams can be seen in **Figure 3.4**. For all the samples of the two systems, the presence of two diffusing species was observed. Tables S1 and S2 of Paper I summarize the self-diffusion coefficients of all the diffusing species detected in the PEG-*g*-PVAc/PE/D_2O and PEG-*g*-PVAc/CAR/D_2O systems, respectively. Starting from the binary sample at 5% polymer in water and by using the Stokes–Einstein equation (for details on the calculations refer to the main text of Paper I), two hydrodynamic radii of 25 and 155 Å were calculated, for the fast and slow diffusing species respectively. The larger diameter species is consistent with previous DLS results (R_H = 114 Å for 5% polymer in water) suggesting that the slow component can be associated with the SCNPs' diffusion. A possible explanation for the fast component is the presence of a polymer synthesis residual such as small oligomers.

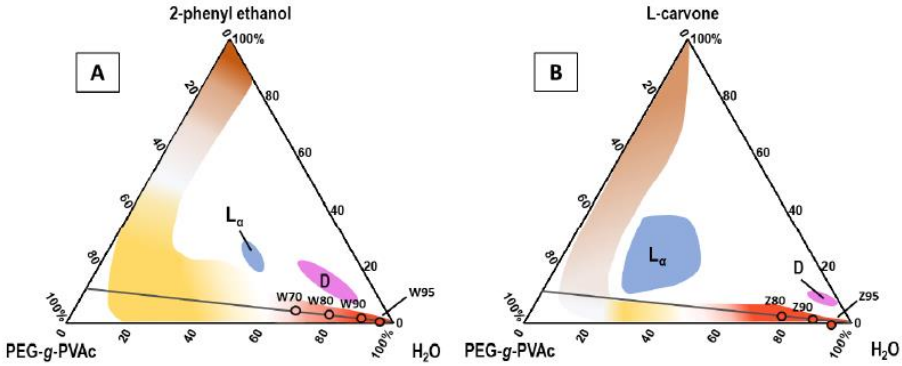

Figure 3.4. Positions of the samples investigated by means of NMR self-diffusion measurements in the PEG-*g*-PVAc/perfume/water phase diagrams with A) 2-phenyl ethanol and B) L-carvone.

Moving to the addition of PRMs, for the sample with 9% polymer and 1% PE, PGSTE yielded a hydrodynamic radius of 321 Å, much larger than expected for the SCNPs. This result can be explained with the interparticle interactions appearing with higher polymer concentrations causing changes in the particle morphology.[92] With further increase of polymer concentration (sample series W90, W80, W70, **Figure 3.4**) an abrupt reduction of the slow

component's self-diffusion coefficient (D_ϕ) was observed. Along the polymer's concentration increase, the system undergoes percolation,[92] and the diffusing particles do not have a spherical shape anymore, but possibly an elongated one, closely interacting but not yet constituting a bicontinuous network. On the other hand, self-diffusion coefficients of PE and D_2O follow an approximately linear decrease, possibly due to the limited available volume as the polymer concentration increases. Similar results were obtained for the PEG-*g*-PVAc/CAR/D_2O system, with a hydrodynamic radius of the slow component equal to 303 Å for the sample with 9% polymer and 1% CAR.

3.2. Evolution of the PEG-*g*-PVAc/water binary axis after perfume addition

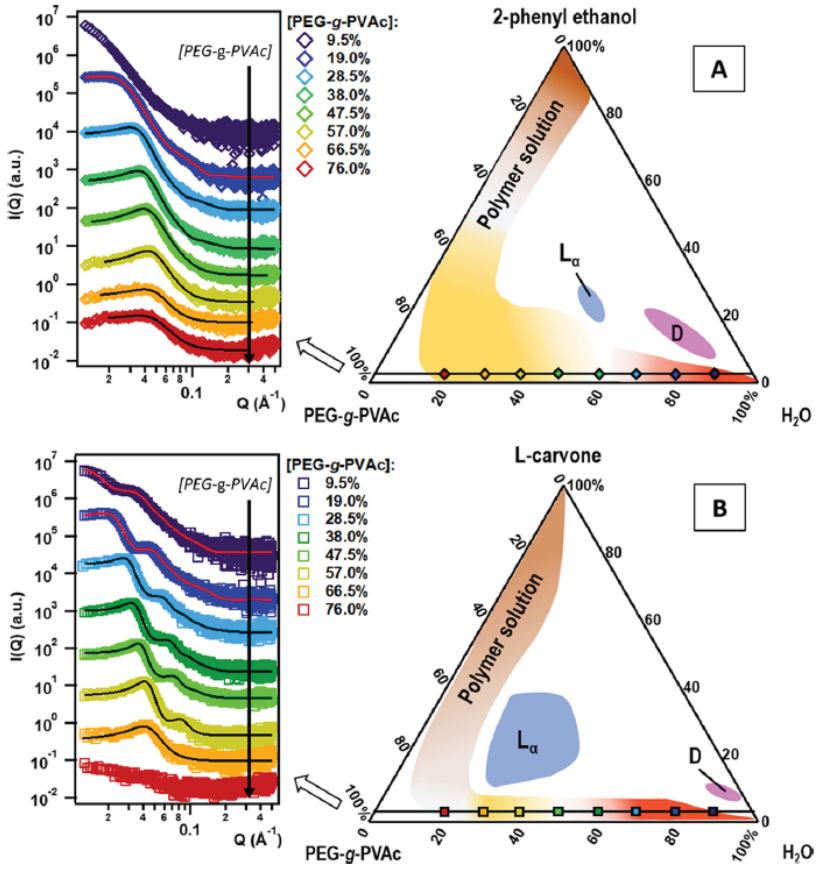

Figure 3.5. SAXS patterns obtained for the samples along the polymer/water axis, with 5% perfume added: (A) PE and (B) CAR. Curves were offset along the y axis for presentation purposes.

The binary system PEG-*g*-PVAc/water was investigated before.[92] As mentioned earlier, results showed the formation of SCNP for polymer concentration <10% that coexisted a bicontinuous network which was becoming more dominant at higher polymer concentration. In this section we investigated the effect of adding 5% perfume to this binary system, using mainly SAXS. Results can be seen in **Figure 3.5**. Starting with PE addition, at 9.5% polymer, a turbid sample was obtained (cloud point = 5−7 °C, Figure S5, Paper I) which split into two phases in few days. The scattering pattern suggested the presence of large aggregates, but no exact size could be determined as their Guinier region lies outside the available SAXS window. At 25 °C, interaction with PE leads to the observed large aggregates that are formed due to a decrease in the cloud point of PEG-*g*-PVAc, similarly to what was observed for this polymer in surfactant solutions and salt addition.[65]

Table 3.3. Fitting results for the SAXS patterns of Figure 3.5A. R_c = core radius; σ = Schulz polydispersity of R; SLD_{core}, SLD_s = scattering length densities of the core and shell, respectively; t = shell thickness; R_{tot} = radius of the core-shell particle; Φ = hard-sphere volume fraction.

[PEG-*g*-PVAc] + 5% PE	**19.0**	**28.5**	**38.0**	**47.5**	**57.0**	**66.5**	**76.0**
Core-shell sphere form factor + hard-sphere structure factor							
R_c (Å)	48 ±0.3	37 ±0.2	-	-	-	-	-
σ	0.3	0.38	-	-	-	-	-
SLD_{core} (10^{-6} Å^{-2})	10.8	10.8	-	-	-	-	-
t_1	64 ±0.2	46 ±0.3	-	-	-	-	-
SLD_{s1} (10^{-6} Å^{-2})	9.51	9.51	-	-	-	-	-
R_{tot} (Å) = R_c + t_1	112	83	-	-	-	-	-
Φ	0.14	0.22	-	-	-	-	-
Teubner – Strey model							
Correlation length, ξ (Å)	-	-	73	70	63	50	42
Repeat distance, d (Å)	-	-	172	152	142	140	148
Amphiphilicity factor, f_a	-	-	-0.5	-0.5	-0.5	-0.4	-0.3

As the polymer concentration increases in the presence of 5% PE, the cloud point was raised above 25 °C and an isotropic solution was formed, with long-

term colloidal stability up to 80% PEG-*g*- PVAc. SAXS curves of the samples (**Figure 3.5A**) show a characteristic correlation peak, evident of strong interactions between the particles, similar to the one observed for PEG-*g*-PVAc binary system before.[92] The peak moves to higher Q values with increasing polymer concentration, indicating a decrease in interparticle distance.

Based on previous analysis for the very dilute PEG-*g*-PVAc/PE SCNPs in water, and assuming globular aggregates, SAXS patterns were fitted with a hard-sphere structure factor:[96]

$$S(Q) = \left[1 + \frac{24\Phi_{HS} G(2QR_{HS})}{2QR_{HS}} \right]^{-1} \qquad \textit{Eq. 3.3}$$

where $G(2QR_{HS})$ is a trigonometric function depending on Q, R_{HS} (hard-sphere radius) and ϕ_{HS} (hard spheres volume fraction). The potential has the form:

$$U(r) = \begin{cases} \infty, r < 2R \\ 0, r \geq 2R \end{cases}$$

For a more detailed description of the model's mathematical expressions and parameters see Supporting Information of Paper I. The form factor used was the one of core–shell spheres (Eq. 3.2, with a single shell). Fitting results can be seen in **Table 3.3**. The obtained SLD for the core was 1.08×10^{-5} Å^{-2} and for the shell 9.51×10^{-6} Å^{-2}. Most probably, at this high PEG-*g*-PVAc concentrations, the colloidal objects might no longer be SCNPs, but rather micelle-like aggregates of two or more polymer chains where the PEG and PVAc blocks are better segregated into a hydrophobic core and a hydrophilic shell. From the fitting it is obvious that the particle size decreases with increasing polymer concentration, from 11.2 nm at 19.0% PEG-*g*-PVAc to 8.3 nm at 28.5%, as it was expected from the moving of the correlation peak to higher Q values. At 38.0% polymer, the spherical model does not fit well anymore the experimental data, and from this point on, the patterns can be fitted using the Teubner–Strey model for bicontinuous structures,[97] as the systems are composed by polymer physical networks:

$$I(Q) = \frac{1}{a_2 + c_1 Q^2 + c_2 Q^4} + B$$

Eq. 3.4

Where the coefficients a, c_1, and c_2 lead to the calculation of the bicontinuous network's lattice size, ξ, and the repeat distance, d. For a detailed description of the model's mathematical expressions and parameters see Supporting Information of Paper I. From the fitting with the Teubner − Strey model, the amphiphilicity factor (f_a) was obtained, which is a measure of the local order in an aqueous surfactant system. The two limits of the parameter are $f_a = -1$ for ordered lamellar liquid crystal phases and $f_a = 1$ for a disordered liquid.[98] In our case, negative values were obtained ranging from −0.5 to −0.3 as the polymer concentration increases from 38% to 76%. This result shows that the presence of PE extends the persistence of stable bicontinuous polymer structures in a large area of the phase diagram and possibly their evolution towards a lamellar phase.

Moving to 5% CAR addition in the binary PEG-*g*-PVAc/water system, SAXS patterns similarly to PE showed a correlation peak moving to higher Q values as the polymer concentration increases (**Figure 3.5B**). The main difference in this system was that the correlation peak is followed by a number of bumps. The bumps can be indicative of core−shell signature, similarly to the very dilute PEG-*g*-PVAc / CAR/ water systems described earlier. Interestingly, the bumps move to higher Q values with increasing PEG-*g*-PVAc, together with the main correlation peak, suggesting that a gradual compression of the cores and shells in the structures occurs. SAXS patterns up to 57.0% polymer were fitted with a core-two-shell form factor (Eq. 3.2) together with a hard-sphere structure factor (equation S4, Paper I). Fitting results can be found in **Table 3.4**. The obtained SLD of the core is the same as in the dilute core−shell systems, 8.9×10^{-6} Å^{-2}, very close to the theoretical value for CAR. However, for polymer concentration > than 9.5%, a good fit can only be obtained if the core SLD is left free to increase gradually, suggesting a better homogenization of CAR among the PVAc chains. From the fitting results it was observed that for volume fractions higher than 0.35, the hard-sphere volume fractions were lower than expected, possibly due to the fact that hard-sphere potential does not describe well high-volume fraction systems with soft particles.[99] For the

highest PEG-*g*-PVAc samples with 57.0 and 66.5% polymer, SAXS patterns were fitted using the Teubner–Strey model, similarly to PE, yielding negative amphiphilicity factors around −0.5.

Table 3.4. Fitting results for the SAXS patterns of Figure 3.5B. R_c = core radius; σ = Schulz polydispersity of R; SLD_{core}, SLD_{s1}, SLD_{S2} = scattering length densities of the core, the first shell and the second shell respectively; t_1 and t_2 = thickness for the first and second shell respectively; R_{tot} = radius of the core-shell particle; Φ = hard-sphere volume fraction.

[PEG-*g*-PVAc] + 5% CAR	**19.0**	**28.5**	**38.0**	**47.5**	**57.0**	**66.5**	**76.0**
Core-shell sphere form factor + hard-sphere structure factor							
R_c (Å)	87 ±0.6	63 ±0.8	64 ±1.3	56 ±0.8	48 ±0.7	-	-
σ	0.31	0.31	0.32	0.30	0.35	-	-
SLD_{core} (10^{-6} Å^{-2})	8.9	9.2	9.7	9.7	9.7	-	-
t_1	32 ±0.7	25 ±0.6	20 ±1.2	22 ±0.9	26 ±0.9	-	-
SLD_{s1} (10^{-6} Å^{-2})	10.5	10.5	10.5	10.5	10.5	-	-
t_2	43 ±1.2	40 ±0.8	20 ±1.4	14 ±0.5	8 ±0.5		
SLD_{S2} (10^{-6} Å^{-2})	9.5	9.5	9.5	9.5	9.5		
R_{tot} (Å) = R_c + t_1	162	128	104	92	82	-	-
Φ	0.15	0.24	0.33	0.35	0.37	-	-
Teubner – Strey model							
Correlation length, ξ (Å)	-	-	-	-	-	89	70
Repeat distance, d (Å)	-	-	-	-	-	160	148
Amphiphilicity factor, f_a	-	-	-	-	-	-0.6	-0.5

3.3. PEG-*g*-PVAc/PRM/water systems at intermediate polymer concentrations

At intermediate polymer concentrations, lamellar liquid crystalline phases (L_α) were formed. Starting from PE, the presence of the perfume at around 25% led to a transition from the disordered bicontinuous structure to an ordered L_α phase. The double-layer liquid crystalline phases were identified with SAXS. Results are shown in **Figure 3.6A**. In the SAXS patterns, typical Bragg

peaks of L_α phases were observed, following the Q-sequence 1:2. The interlamellar distance (d) was calculated according to the relation $2\pi n/Q(n)$, where n is the order of diffraction and Q(n) is the corresponding Q value,[100,101] yielding d = 250 Å for a representative sample taken in the centre of the L_α region.

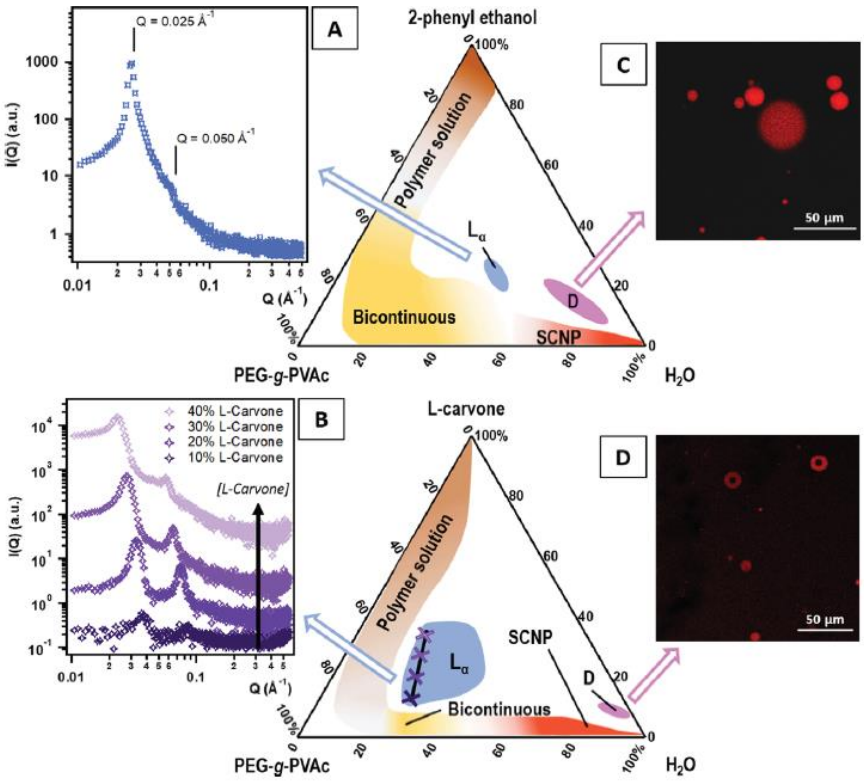

Figure 3.6. (A, B) SAXS patterns obtained for: (A) a representative sample from the L_α region in the PEG-$_g$-PVAc/2-phenyl ethanol/water system (28/30/42% w/w) and (B) four samples along a dilution line in perfume in the L_α region of the PEG-$_g$-PVAc/L-carvone/water system (curves were offset along the y axis for presentation purposes). (C, D) Confocal scanning laser microscopy images of representative samples in the "D" region of the phase diagrams of (C) PEG-$_g$-PVAc/2-phenyl ethanol/water and (D) PEG-$_g$-PVAc/L-carvone/water.

Moving to the PEG-*g*-PVAc/CAR/water phase diagram, a larger L_α region was observed compared to PE, which is also shifted to higher polymer concentrations. For the SAXS analysis, four samples within this area (**Figure 3.6B**) following a carvone dilution line were selected to calculate the lattice spacings. Results are shown in **Table 3.5**., showing that the L_α structure is

swollen as the concentration of the perfume increases from 10% (d = 165 Å) to 40% (d = 273 Å), suggesting the insertion of carvone in the hydrophobic PVAc palisade.

Table 3.5. Lamellar lattice spacing parameters (d) Corresponding to four samples along a carvone dilution line (polymer/water ratio held constant at 70/30 %w/w).

L-carvone content (%w/w)	**d (Å, ±0.6 Å)**
10	165
20	190
30	232
40	273

Moving towards the water corner of the phase diagram, a micro-capsule region ("D" region) was evident in both PE and CAR phase diagrams, with the related samples to present a milky-white liquid appearance. Observation of the samples with the optical microscope revealed spherical objects of around ten micron size, suggesting the spontaneous (or low energy) formation of a stable emulsion phase. The milky suspensions appeared to form spontaneously upon gentle mixing of the three components, and they were stable for long periods of time (at least 6 months). They resisted centrifugation, freezing, and heating up to 50 °C. However, the real thermodynamic stability of such systems cannot be confirmed by these properties alone as this aspect deserves further study. For the present scope, it is worth mentioning that these findings support the possibility to employ fragrance-driven coacervation of PEG-*g*-PVAc aqueous dispersions as a robust encapsulation method in products containing high levels of water.

To get more information on the aggregates' structure, the same samples were prepared using rhodamine-B labelled PEG-*g*-PVAc and observed with confocal scanning laser microscopy (CLSM). The micrograph of the sample containing PE can be seen in **Figure 3.6C**. Spherical objects of heterogeneous sizes were observed, ranging from a few microns to about 40 μm. The red fluorescence of the polymer was homogeneously distributed within the object. The polymer-rich structures were similar to the ones observed before in the presence of surfactant mixtures,[65] which have been identified as coacervates deriving from liquid–liquid phase separation. This suggests that PE could

drive the liquid–liquid phase separation by lowering the cloud point of the polymer, and it should therefore be embedded in the polymer matrix. The micro-capsule region was also present in the L-carvone phase diagram, but covering a smaller region, and its position is shifted closer to the water corner. Rhodamine-B labelled PEG-*g*-PVAc samples investigated under CLSM (**Figure 3.6D**) showed, surprisingly, a different structure for the coacervate droplets: instead of full polymer-rich spheres, L-carvone induces the formation of structures remindful of giant polymersomes with an average radius of around 15 μm and a polymer shell thickness of around 4 μm. Interestingly, the structure of these aggregates seems to follow hierarchically the structure of the SCNP at higher dilution: full spheres for PE and core–shell for CAR.

3.4. PEG-*g*-PVAc/α-pinene/water system phase diagram

The phase diagram for the ternary system PEG-*g*-PVAc/α-pinene/water at 25 °C is shown in **Figure 3.7**. The phase diagram was dominated by a three-phase region. In a typical sample, the upper and lower phases appeared as isotropic, while the middle phase was opaque. This is remindful of a Winsor-III-type microemulsion,[102] where a central phase rich in surfactant (bicontinuous microemulsion) is in equilibrium with excess water and oil (lower and upper phases, respectively, considering the densities). This suggests that very low amounts of pinene might actually be miscible with the polymer. CLSM imaging of the middle phase (**Figure 3.6A**), from samples prepared with rhodamine-B polymer, revealed diffuse fluorescence from a concentrated aqueous polymer phase dotted with black spherical objects. The black spheres are most likely droplets of insoluble perfume trapped in the polymer phase due to its high viscosity. SAXS curves (**Figure 3.6B**) of the middle phase in four samples marked in the phase diagram, taken along a dilution line in pinene covering almost the entire phase diagram, were almost superimposable. This observation shows that the nanostructure depends on the polymer/water ratio, which does not vary across the dilution line. The scattering patterns are very similar to the ones obtained for samples in the PE and CAR systems at a high polymer concentration, consistent with a bicontinuous structure.

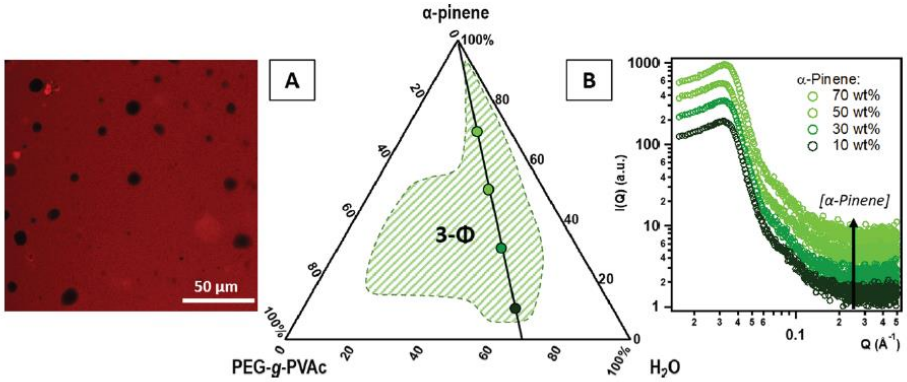

Figure 3.7. PEG-*g*-PVAc/α-pinene/water phase diagram at 25 °C. The green-shaded area indicates a three-phase (3Φ) region, and the white areas indicate two-phase regions. (A) CLSM micrograph obtained for the middle phase of a typical sample in the 3Φ region, prepared with rhodamine-B labeled polymer; (B) SAXS patterns obtained for the middle phases of samples along the dilution line characterized by a polymer/water ratio = 30/70% w/w, with increasing α-pinene concentration, as evidenced in the phase diagram. Curves were offset along the y axis for presentation purposes.

The selective solubilization of organic compounds by block copolymer micelles has been known since Nagarajan's work,[103] and many studies have explored the link between a fragrance's *log* K_{ow} value and its preferential location in a micellar structure.[104] One drawback of many studies, however, is to limit the investigation to the extremely dilute micellar phases and to assume, for the micelles, completely segregated core and shell regions consisting of each of the polymer blocks in consideration. In this work, we have extended the focus to the entire phase diagram of polymer/ perfume/water systems using the amphiphilic PEG-*g*-PVAc and three common natural fragrances. We have shown that 2-phenyl ethanol and L-carvone are both encapsulated in polymer single-chain nanoparticles, while α-pinene is too hydrophobic and it separates from the self-assembled structures at all ratios. Moreover, the two successfully encapsulated fragrances lead to similar phase behaviours but different nano- and micro-structures (matrix-like for PE and core–shell for CAR), and the borders of the thermodynamically stable regions differ in the two-phase diagrams. One of the possible consequences on final formulations could be the demixing of complex perfume blends when one or more of the components have no affinity for any of the polymer blocks. In conclusion, the graft copolymer PEG-g-PVAc described here is an extremely promising

candidate for the encapsulation of actives in a number of different applications. Thanks to its varied polymorphism, it offers a choice of thermodynamically stable means of encapsulation, where the spontaneous formation upon simple mixing of the components results in a low-energy input necessary for production and thus cost-effective production, as long as the formulation design takes into account the details of encapsulate-to-polymer blocks interactions.

Results and Discussion: Part 2

Investigation of the self-assembly properties of Soluplus or PEG-*g*-(PVAc-co-PVCL) aqueous solutions

Soluplus, or poly(ethylene glycol) – poly(vinyl acetate) – poly(vinyl caprolactam) (PEG-*g*-(PVAc-*co*-PVCL) graft copolymer (**Scheme 1**), is a non-linear graft copolymer that has a 6 kDa PEG backbone and a grafting chain composed by VAc and VCL units. Its biocompatible profile and amphiphilic nature have led to its wide usage as a solubilizing medium for several poorly water-soluble drugs (among others: quercetin,[105] carvedilol[106] and lipoic acid[107]), and as a matrix former for the manufacture of solid dispersions.[108,109] Soluplus in low concentrations is known to self-assemble into micellar structures in aqueous solutions with a critical micelle concentration (CMC) of 7.6 mg/L. [79] Soluplus' micelles are reported to have an average hydrodynamic diameter (D_h) of 55 – 65 nm depending on the polymer concentration and temperature,[110–112] however, in-depth characterization concerning their structure, shape, and interactions is still lacking. Increasing polymer's concentration up to 50% w/w leads to a progressive increment of the viscosity and improvement of the elastic properties of the material, but despite the gel-like appearance, there have been no rheological evidences of network formation.[106,109,113] The nanoscale structures and interactions characterizing these systems, both in diluted and concentrated solutions, therefore merits further investigation.

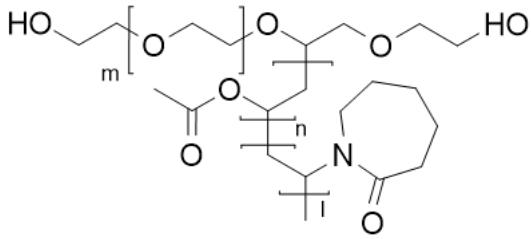

Scheme 4.1. Molecular structure of Soluplus (PEG-*g*-(PVAc-*co*-PVCL).

Based on our previous studies on PEG-*g*-PVAc,[91] which is an amphiphilic non-linear copolymer with similar structure, a possible interesting application for Soluplus is to be used as an encapsulating agent for fragrances in industrial formulations. The significant presence of VCL in Soluplus' graft chain (57% w/w) changes the hydrophilic/hydrophobic balance within the molecule compared to PEG-*g*-PVAc, making this polymer a strong candidate for the encapsulation of a different range of guests: the core of Soluplus micelles, being a more hydrophobic environment compared to water, exhibits a more comfortable space to host hydrophobic guests. At the same time, the presence of VCL in the hydrophobic part of the polymer (the PVAc-*co*-PVCL chain), while being itself a hydrophilic monomer, can offer Soluplus' micelles the possibility to host relatively more hydrophilic guests. Since perfumes being used in homecare or cosmetics industry can be composed by dozens to hundreds of perfume raw materials (PRMs) with different hydrophobicity and other molecular characteristics, a polymer able to host molecules with an ample range of hydrophobicity is of great importance. Soluplus presents additional interesting properties that make it a possible candidate as perfume carrier for our target application. It is noteworthy to mention the tendency of the market in the last years, in moving towards more environmentally-friendly technologies for perfume encapsulation,[10] but also towards "smart" materials where the release of active can be triggered by external stimuli.[114–116] PVCL is a thermosensitive unit, exhibiting a lower critical solution temperature (LCST) of 30-34 ºC, that can potentially add to the polymer thermo-responsive properties.[117,118] Despite the fact that PVCL hydrogels show a similar behavior with PNIPAm hydrogels, they are much less popular among researchers due to the difficulty of a controlled polymerization of the VCL monomer. Moreover, the fact that VCL is biodegradable, it can potentially improve the biodegradability profile of the polymer.[119,120]

For all the above-mentioned reasons, the potential of Soluplus as an encapsulating agent for different perfume molecules in aqueous solutions was investigated. In this chapter, we will first characterize the polymer' structure through NMR, and then investigate its self-assembly properties in aqueous solutions, by means of SANS, rheology and DSC. In a next chapter, Soluplus' potentials in perfume encapsulation will be exploited.

4.1. Characterization of Soluplus macromolecule

The molecular structure of Soluplus, its monomeric components and their relative ratio in the macromolecule were investigated by means of NMR spectroscopy. ^{1}H-NMR spectra of Soluplus in DMSO-d_6 can be seen in **Figure 4.1**. {^{1}H-^{1}H}-NOESY map of Soluplus in DMSO-d_6 can be seen in **Figure 4.2** while {^{1}H-^{13}C}-HSQC and {^{1}H-^{1}H}-COSY correlation maps can be seen in Figure S1 and Figure S3, Supporting Information, Paper II. The bands were clearly assigned for Soluplus, as shown in the ^{1}H-NMR spectra of **Figure 4.1**, completely consistent with the expected structure. In addition, the actual EG/VAc/VCL ratio was calculated by opportunely integrating ^{1}H-NMR peaks. The resulting weight percentage of the three components is 13% EG, 34% VAc and 53% VCL, in good agreement with the one reported by the supplier (13% EG, 30% VAc and 57% VCL)[79]. The determination of number of grafting sites per chain, as previously reported for PEG-*g*-PVAc,[74] was attempted through inverse-gated proton decoupled ^{13}C-NMR. Unfortunately in this case it was not possible to find a detectable band clearly allied with the resonance of the PEG's grafted methynes. Such result is however compatible with a very low degree of grafting, being it below the intrinsic detection limit of the technique. Moreover {^{1}H-^{1}H}-NOESY maps were used to gain insights on the block or random nature of the P(VAc-*co*-VCL) portion. The presence of strong correlation signals between almost all vinyl caprolactam and vinyl acetate resonances suggested a prevalently random or alternate distribution, excluding a block configuration. A more quantitative evaluation of the degree of blockiness of the P(VAc-*co*-VCL) moiety was thus obtained by following an approach similar to the one reported by Moritani *et al.*[121] for partly hydrolyzed polyvinyl alcohol. A blockiness index (η_B) for binary copolymers can be defined as the ratio between the fraction of alternate dyads (*e.g.* VAc-VCL) and the run fraction of the copolymer as purely random. It can take values between 0 for block copolymers and 2 for perfectly alternate ones, while a value of $\eta_B = 1$ is indicative of a completely random distribution. In our case, the fraction of VAc monomers in alternate (VAc, VCL) dyads was estimated through the deconvolution of the ^{1}H-NMR band in the 4-5 ppm range, as shown in **Figure 4.1**, in four Gaussian curves, one per each possible dyad, and their relative assignment and integration. A blockiness index of $\eta_B \approx 0.8$ was

obtained in line with a prevalently random configuration with no clear tendency for a block or alternate ones.

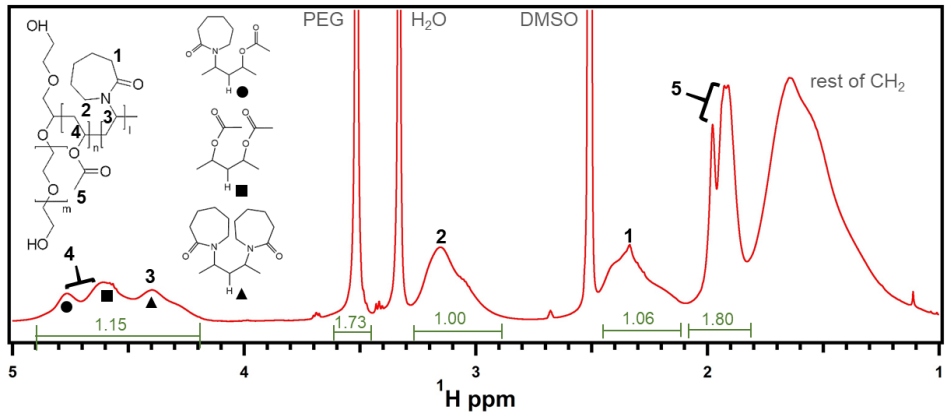

Figure 4.1. Soluplus 30 mg/mL in DMSO-d_6, ^{1}H-NMR spectrum.

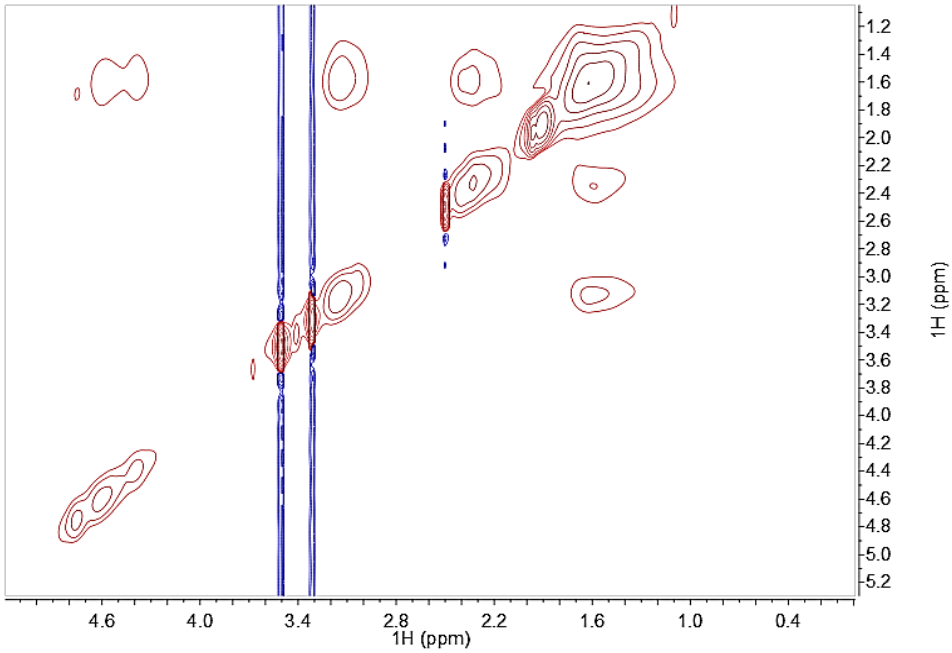

Figure 4.2. Soluplus 30 mg/ml in DMSO-d_6, NOESY map.

4.2. Self-assembly properties and nanostructure of Soluplus in water

The investigation of Soluplus' self-assembly properties in water started from the critical micellar concentration (CMC) determination using tensiometry. Surface tension *vs* Soluplus concentration results can be seen in **Figure 4.3**, yielding the value of 7.6 ± 0.1 mg/L, in good agreement with the value reported from the manufacturer and other literature.[79,122]

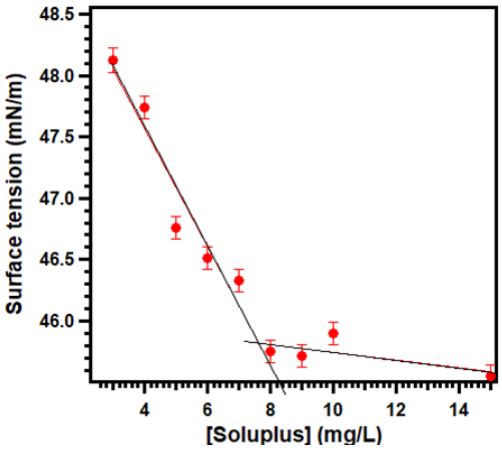

Figure 4.3. Surface tension vs Soluplus concentration – determination of Soluplus' critical micellar concentration (CMC).

Soluplus solutions in D_2O were further analysed by means of small-angle neutron scattering (SANS) and **Figure 4.4** shows the SANS scattering patterns for binary samples with concentrations ranging from 1% to 55% w/w, normalized by the theoretical volume fraction of the dispersed phase and after removing a constant value of each curve that accounts for the incoherent scattering background. Non-normalized SANS patterns can be seen in Figure S5, Paper II. A first, qualitative analysis of the curves reveals a downturn of the scattering intensity I(Q) in the low-Q region for concentrations higher than 1%, and further the appearance of an interaction peak that grows in intensity and moves to higher Q values as the polymer content increases. The shift of the interaction peak towards higher Q values is evidence of the decrease in the inter-particle distance while the particles are coming into closer contact. For all curves, the intensity decrease in the Porod region (high Q values in a log I/log Q plot) approximately follows a Q^{-2} power law, typical of polymer coils.

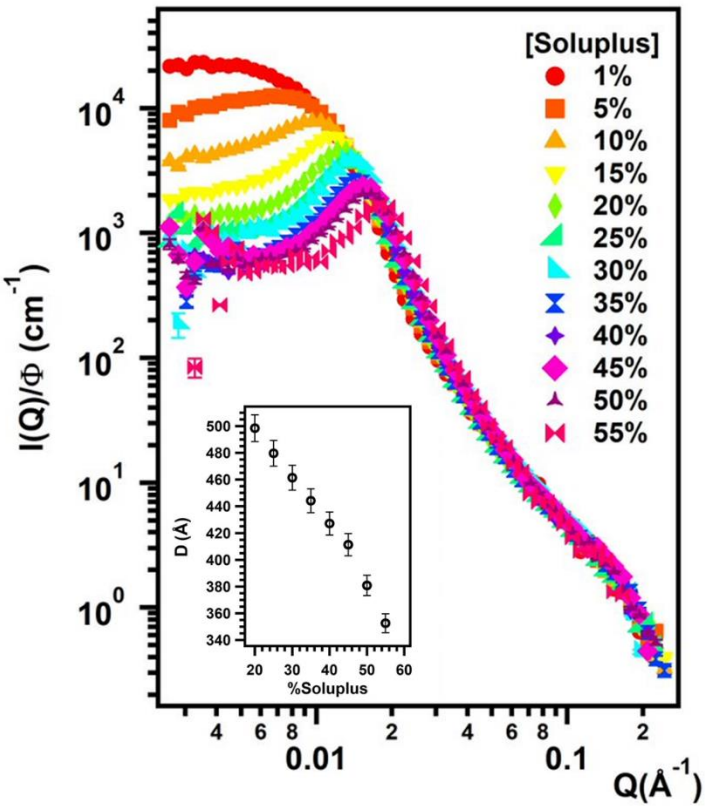

Figure 4.4. SANS curves normalized by the volume fraction for samples containing Soluplus in water with concentrations from 1% to 55% in steps of 5%. Inset: Intermicellar distance, *D* (obtained from the correlation peak position) *vs.* polymer concentration.

Further quantitative analysis of Soluplus' aqueous solutions started from the 1% Soluplus, the most dilute sample. A Kratky plot for this curve, Q^2*I(Q) *vs.* Q that can be seen in Figure S6, Supporting Information, Paper II, showed that the scattering objects in the sample are globular.[83] The radius of gyration, R_G, was calculated from the SANS data through a Guinier plot, Ln(I(Q) *vs.* Q^2 (**Figure 4.5**), using the approximation:[83]

$$Ln[I(Q)] = Ln[I_0] - \frac{Q^2 R_G{}^2}{3} \qquad \textit{Eq. 4.1}$$

which led to R_G = 177 ± 5 Å. From the relationship $R_G{}^2 = 3/5\ R^2$ for spherical objects where R is the radius of the micelle,[123] we obtain R = 228.5 Å, consistent with a slightly bigger R_H reported in literature (R_H of Soluplus

micelles ranges between 275 and 325 Å).[110,112] The interaction peak position was translated into real distance using the relation $D = 2\pi/Q$ and plotted in the inset of **Figure 4.4** against Soluplus concentration.

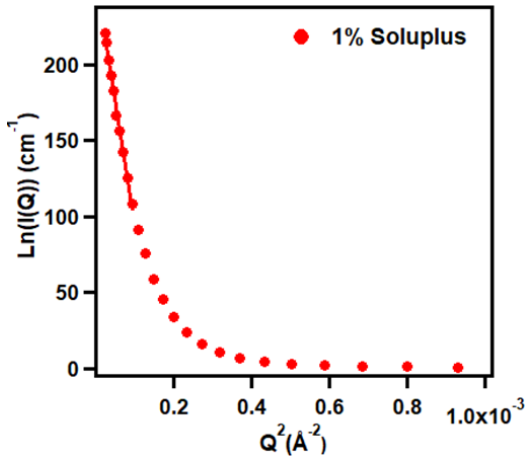

Figure 4.5. Guinier plot, Ln(I(Q) *vs.* Q^2, for Soluplus 1% SANS pattern.

For soft, highly hydrated colloidal particles like Soluplus micelles, the volume fraction usually cannot be calculated directly from the sample composition; rather, the effective volume fraction (Φ_H) needs to be considered. A common method to evaluate Φ_H for such systems is through rheology with the use of relative viscosity, η_r. According to the Batchelor – Einstein equation, Φ_H is related, in dilute conditions, with the relative viscosity of the colloidal suspension according to the equation:[124–127]

$$\eta_r = 1 + \frac{5}{2}\Phi_H + \gamma\Phi_H^2 \qquad \textit{Eq. 4.2}$$

We define $\Phi_H = kC$, where C is the weight fraction of the sample and k is a constant of proportionality. k and γ can be extracted by plotting η_r with weight concentration and then fitting with the Batchelor-Einstein equation substituting Φ_H with kC. Additionally to the determination of k that leads to Φ_H, γ coefficient can give information on the inter-particle interactions. For Brownian hard spheres γ is expected to take values between 5.9 and 6.2, while higher values are indicative of attraction between the colloidal particles. The flow curves of Soluplus in water from 1 to 7.5 % w/w are presented in **Figure 4.6**. It is evident that the samples up to 7.5% w/w exhibit Newtonian fluid

behavior and their viscosity remains constant over the accessible shear rate window, as expected from previous studies suggesting that Soluplus aqueous solutions exhibiting Newtonian behavior up to 20% w/w.[113] The relative viscosity of the dilute solutions was plotted against the weight polymer concentration (**Figure 4.6**). Best fitting with Eq. 4.2 gave 1 + (10±0.5)C + (107.1±0.7)C^2 leading to k = 4.0 ± 0.2 and γ = 6.7 ± 0.4. The analysis is though suggesting that Φ_H is about four times that of the theoretical obtained by the weight fraction of the suspensions. The value of γ coefficient is higher than the one expected for hard spheres suggesting the potential attractive interactions between Soluplus micelles. The obtained value of Φ_H was used for the fitting of SANS patterns of the diluted Soluplus water solutions (1 and 5% w/w).

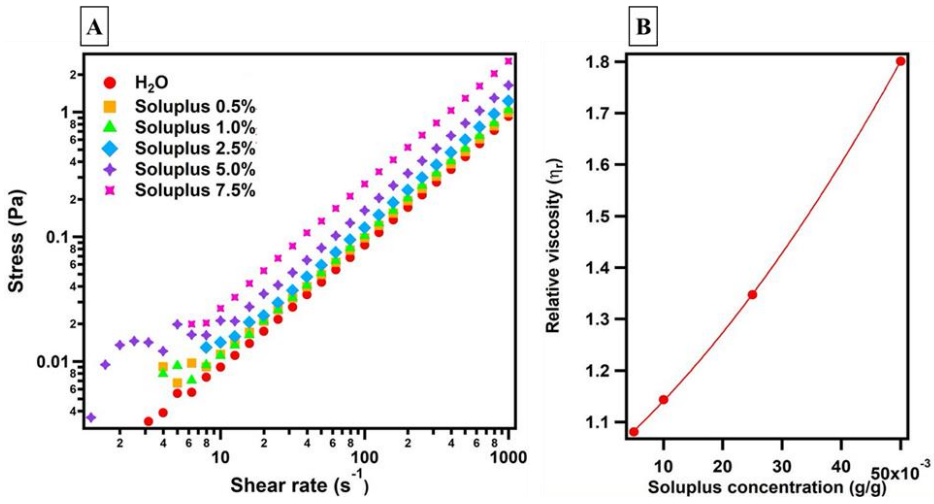

Figure 4.6. A) Flow curves of Soluplus in water for samples from C = 0.5% to 7.5%. B) Relative viscosity of Soluplus 1, 2.5, 5 and 7.5% samples as obtained from the flow curves *vs* Soluplus concentration, fitted to Eq. 4.2.

SANS patterns from 1% to 15% Soluplus were modelled according to a fuzzy sphere form factor with a double Yukawa interaction potential:[96,128]

$$I(Q) = \frac{\Phi}{V}(\Delta p)^2 P(Q)S(Q) + I_{fluct}(Q) + B \qquad \textit{Eq. 4.3}$$

Where Δ_p is the scattering length density (SLD) difference between the sphere and the solvent, Φ is the volume fraction of particles and V the sphere volume, P(Q) is the fuzzy sphere form factor, S(Q) the 2-Yukawa structure

factor, I_{fluct} an additional Lorentzian term and B the incoherent background. A detailed explanation of the terms and parameters can be found in Supporting Information, Paper II (Eq. S3 – S7). This model describes micelles as spherical particles in which the polymer density is gradually decaying from the particle's center to its surface. The micelle is thus composed by a more compact core and a corona with a fuzzy interface, which in the present case should be constituted, respectively, by the slightly more hydrophobic P(VAc-*co*-VCL) grafts and the more hydrophilic PEG backbone portions of the polymer macromolecule. A Lorentzian term is added to the model, describing the ensemble average correlations in the polymer network.[96] The fitting procedure for Soluplus 1% to 15% SANS patterns using Eq. 4.3, led to the results summarized in **Table 4.1** and fitted curves can be seen in **Figure 4.7**

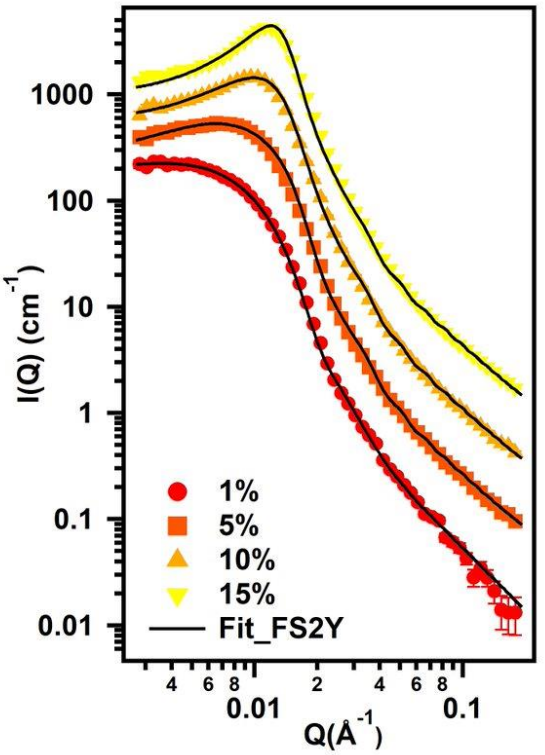

Figure 4.7. SANS patterns obtained for the samples containing 1% to 15% Soluplus in D_2O. Markers represent experimental points and solid line represents fitting with the fuzzy sphere – 2Y model as explained in the main text. Curves were offset along the y-axis for presentation purposes.

Table 4.1. Structural parameters obtained by fitting the 1% - 15% of Soluplus/D_2O SANS curve to Equation S2 of Paper II. The parameters for which no error is given were kept fixed during the fitting procedure. "L. scale" = Lorentzian scale; "L. length" = Lorentzian length.

Soluplus (% w/w)	**1**	**5**	**10**	**15**
Volume fraction	0.04	0.2	0.25	0.28
Core radius, R_{core} (Å)	173 ± 6	178 ± 7	173 ± 7	171± 3
Core polydispersity	0.27	0.27	0.34	0.38
Fuzziness, σ (Å)	25	25	23	23
Core SLD ($Å^{-2}$)	4.95 10-6	4.8 10-6	4.4 10-6	4.2 10-6
Solvent SLD ($Å^{-2}$)	6.4 10-6	6.4 10-6	6.4 10-6	6.4 10-6
L. scale	2	5	7.2	7.2
L. length (Å)	60	44	38	31
Attraction strength	3.0 ± 0.3	4.06 ± 0.05	4.0 ± 0.1	4.5 ± 0.1
Attraction range par.	19 ± 2	28.0 ± 0.1	29.0 ± 0.3	30.0 ± 0.1
Repulsion strength	-0.40 ± 0.01	-0.70 ± 0.01	-2.8 ± 0.1	-6.7 ± 0.1
Repulsion range par.	1.19 ± 0.01	1.20 ± 0.01	2.2 ± 0.1	2.3 ± 0.1

For Soluplus 1 and 5%, the calculated from rheology Φ_H was used for the fitting procedure. For 10 and 15%, the volume fraction was left as a free parameter. In those two samples the concentration was higher than the concentration range studied with rheology using the Bachelor-Einstein method for the Φ_{eff} calculation in diluted conditions. Thus, using the approach adopted for more diluted samples to evaluate Φ_H was considered unfeasible for samples having concentration higher than 7.5%. Moreover, it would have led to extremely high-volume fractions, which likely are unphysical. The size of the micelle can be obtained from the fitting parameters as $R = R_{core} + 2\sigma$.[129] The fitting shows that the micellar radius, R, is around 22.4 nm and almost constant in the 1-15% polymer concentration range. The correlation length, ξ, of the Lorentzian term is reduced from 6 nm for 1%, to 4.4 nm, 3.8 nm and 3.1 nm for 5%, 10% and 15% respectively. This was expected and it is in agreement with literature data on PNIPAm microgels, where as the effective volume fraction increases the polymer chain fluctuations are restricted to a smaller length scale.[96] Regarding the structure factor parameters, the attraction and repulsion ranges (inversely proportional to the range parameters reported in **Table 4.1**) decrease with increasing polymer concentration, as expected,

since micelles are coming into closer contact. The 2Y interaction potential with a long-range repulsion and a short-range attraction component is consistent with our earlier finding that attractive interactions are also present between Soluplus micelles from rheology analysis, which can arise from inter-chain attraction of polymer chains in the micellar corona. With another look in the inset of **Figure 4.4**, intermicellar distance for 35% w/w Soluplus is already 44 nm, meaning that the micellar structures are already into contact (assuming that their size remains more-or-less constant, around 22.4 nm).

The Soluplus/D_2O patterns with concentration >20% w/w were successfully fitted with the Teubner Strey (TS) model with an additional Lorentzian term (TS/Lor model). The mathematical expression of this model was described earlier in Results and Discussion Part I (see Eq. 3.4). The obtained fitting curves and parameters can be seen in **Figure 4.8** and **Table 4.2** respectively. The mathematical function of TS/Lor model is given also in the Supporting Information of Paper II along with a detailed explanation of the parameters. The TS model has been originally developed by Teubner and Strey to describe three- (or more) component microemulsion systems,[97] but it has been successfully extended to interpret the scattering behaviour of micellar systems,[130,131] and two-component systems,[92,132,133] in the case where the microscopic structure of the two-component system contains discrete domains rich in water and others rich in amphiphile. For Soluplus/D_2O binary mixtures, as the concentration of the amphiphilic polymer increases, the micellar phases start to inter-penetrate one into the other, suggesting a good example of a bi-continuous system with water-rich and amphiphile-rich domains. Additionally, a Lorentzian term was included in the fitting procedure (similarly to the fuzzy sphere – 2Y model for diluted samples) that accounts for the enhanced density fluctuations of the polymer chains in the micellar surface as the Q increases. The Lorentzian term describes well the scattering intensity at the high-Q region of the patterns, taking into account that they follow a Q^{-2} exponent. The obtained ξ and d parameters were decreasing (except of ξ for the 20% sample), as expected, for micellar systems coming into closer contact and the fluctuations of the polymer chains are restricted. The amphiphilicity factor, f_a, that can be derived from ξ and d using (Eq. S15, Paper II) describes the amphiphile's "strength" or "quality" and the degree of order in the system. The amphiphilicity factor can vary between $-1 < f_a < 1$, where $f_a = -1$ corresponds to an ordered system and $f_a = 1$ corresponds to a

disordered phase. When f_a is negative and approaches –1, the scattering intensity exhibits well-defined peaks at I(q) ≠ 0, and the system can be characterized as a strong amphiphile with ordered domains, as it happens for example in lamellar phases. Interestingly, for Soluplus/D_2O mixtures the calculated amphiphilicity factor f_a, was more-or-less constant and its value varied between -0.87 and -0.90, values close to f_a = -1 for strong amphiphiles and ordered systems. For micellar systems, like for the Soluplus/D_2O systems, the periodicity parameter (d) obtained from the TS model represents the inter-micellar distance.[133] Earlier, we have attempted to extract the inter-micellar distance (D) through the common relation $2\pi/Q_{max}$, from the Q value of the intensity maximum of the patterns' correlation peak. The two values of the intermicellar distance (see **Table 4.2**) obtained from the fitting with the TS model (d) and from the Q_{max} (D) are in a relatively good agreement.

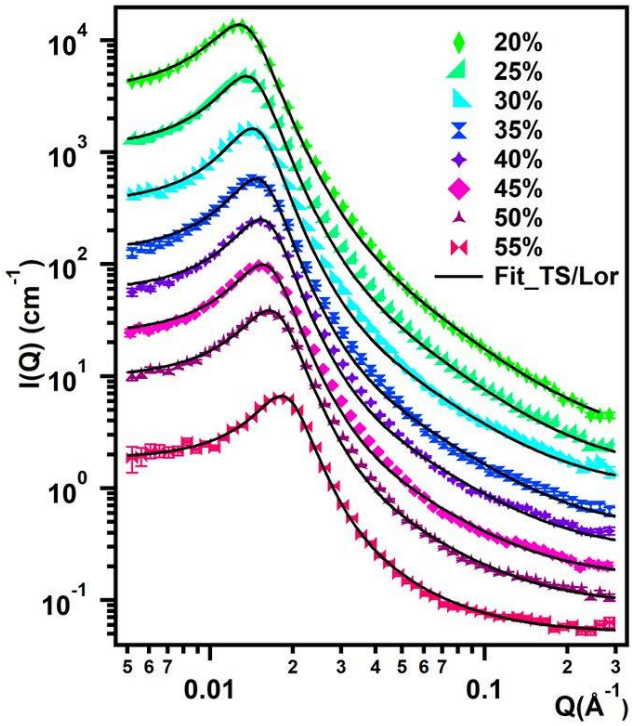

Figure 4.8: SANS patterns obtained for the samples containing 20% to 55% Soluplus in D_2O. Markers represent experimental points and solid line represents fitting with the TS/Lor model (Eq. S16, Paper II) as explained in the main text. Curves were offset along the y-axis for presentation purposes.

Table 4.2: Structural parameters obtained by fitting the 20% - 55% of Soluplus/D_2O SANS curves with the TS/Lor model (Eq. S16, Paper II). The parameters for which no error is given were kept fixed during the fitting procedure. The amphiphilicity factor fa was calculated with Eq. S15 and the intermicellar distance, D was calculated from $2\pi/Q_{max}$ from the position of the correlation peak of the scattering curves. L. scale: Lorentzian scale; L. length: Lorentzian length.

Soluplus (% w/w)	**ξ (Å)**	**d (Å)**	**f_α**	**L. scale**	**L. length (Å)**	**D (Å)**
20	286 ± 2	475 ± 1	-0.87	7	30	498.41
25	293 ± 3	449 ± 1	-0.89	7	29	479.76
30	292 ± 4	428 ± 1	-0.90	4.5	29	461.43
35	276 ± 4	414 ± 1	-0.89	5.5	25	444.13
40	264 ± 4	399 ± 1	-0.89	4.5	26	427.21
45	250 ± 4	386 ± 1	-0.89	4.5	27	411.26
50	235 ± 3	370 ± 1	-0.88	4.5	28	380.84
55	223 ± 3	334 ± 1	-0.89	2	43	352.61

More information on the micellar phases' ordering at high concentration can be accessed by exploiting further the position of the correlation peaks present in the SANS patterns. The intermicellar distance (*D or d*) depends on the amphiphile concentration and, for globular micelles following a face centered-cubic ordering, the mean distance between micelles is given by:

$$D = \frac{1}{\sqrt{2}}\left\{\frac{4000N}{N_A[c]}\right\}^{1/3} \times 10^8\,\text{Å} \qquad \textit{Eq. 4.4}$$

where Q_{max} is the correlation peak maximum, c is the molar concentration of the polymer and N_A is the aggregation number. **Figure 4.9** plots the intermicellar distance, D (derived from $2\pi/Q_{max}$) or d (obtained after fitting with the TS model) *versus* the reverse cubic root of the polymer concentration and the points can be fitted to a straight line. For this analysis, Soluplus/D_2O samples with concentrations 20 – 45% have been taken into account. For lower concentrations, the correlation peak was broad and thus its maxima was risky to be estimated with high accuracy. The two highest concentration samples, 50 and 55% w/w, were deviating from the linear behavior of the rest of the points, suggesting a possible structural change within the system at

these concentrations (e.g. no longer globular shape of the inner domains), and were excluded from the analysis. The fact that the points are following a good linear relation with the reverse cubic root of the polymer concentration is an indication for a face centered-cubic ordering of Soluplus micelles, supporting our earlier finding of the f_a being close to the one of ordered systems, and a concentration-independent globular shape across the concentration range studied.[134] Through this analysis the aggregation number, N_A of the micellar system, can be then calculated from the slope of the linear fitting in **Figure 4.9**, leading to $N_A = 32 \pm 1$.

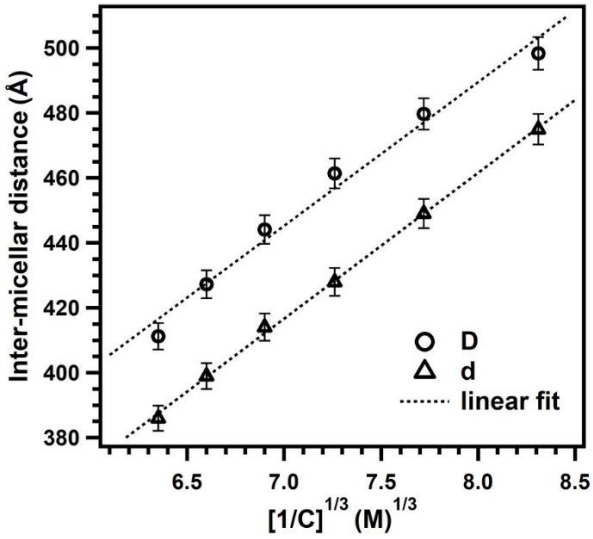

Figure 4.9. Intermicellar distance, *D* (derived from $2\pi/Q_{max}$) or *d* (obtained after fitting with the TS model) *vs.* the reverse cubic root of the polymer concentration. R^2=0.98, slope = 42 ± 2 for D; R^2=0.99, slope = 43 ± 1 for d.

This value was further confirmed by thermal analysis. DSC thermograms for the samples 1 – 80% Soluplus in H_2O are shown in **Figure 4.10** (for ease of comparison with the SANS results, the same set of experiments was also performed in D_2O solutions; see **Figure S9** of Supporting Information, Paper II). Integrating the endothermic peak due to the melting transition of water (around 0 °C) yields the ΔH_f of each sample, and the free water content (FWC) by means of Eq. 2.3 of the Materials and Methods section. For the sample containing 1% Soluplus, FWC was 93% of the total water content in the sample (calculations in Supporting Information, Paper II); therefore, the remaining 7% water is represented by non-freezable water bound to the

hydrophilic moieties of the polymer. N_A can be, thus, approximately obtained by dividing the total volume of a micelle ($V_{micelle}$) by that of each polymer chain (V_{chain}) according to Eq. S18 (Supporting Information, Paper II). Following this approach, we obtain $N_A = 30 \pm 1$, in agreement with the value obtained from the SANS.

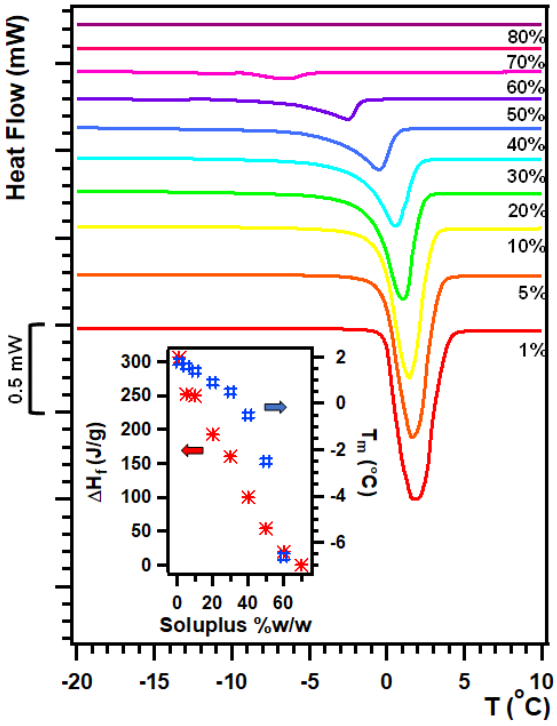

Figure 4.10. DSC thermograms for Soluplus samples in H_2O. Inset: enthalpies of fusion (ΔH_f, J/g) and melting temperatures (T_m, °C) as a function of polymer concentration.

Furthermore, the analysis of DSC data offers information on the hydration of polymer chains. The inset in **Figure 4.10** shows the dependence of ΔH_f, obtained from the integration of the endothermic for each DSC curve of **Figure 4.10**, on polymer concentration. As expected, increasing polymer concentration up to 70%, ΔH_f (and, as a consequence, FWC) decreases, until there is no more free water in the sample (in both H_2O and D_2O). If we initially consider that only PEG is hydrated, this gives 7-8 water molecules per EO unit (calculations in Supporting Information of Paper II). This number is significantly higher than the number reported in literature (3-4 H_2O per EO unit), indicating that likely also VCL units of the graft chain could be hydrated.

This finding is not surprising, since VCL is mostly hydrophilic and as hydrated as PEG units, according to literature.[135] The high average hydration of Soluplus chains can thus account for the large values obtained for the core SLD, meaning that water can penetrate deep into micelles, as it happens for PNIPAm microgels, which share several structural features with Soluplus supramolecular aggregates.[136–138]

In this chapter, Soluplus or PEG-*g*-(PVAc-*co*-PVCL), has been investigated in terms of its self-assembly properties in aqueous solutions. Soluplus' aqueous solutions were characterized up to 70% Soluplus (w/w) by means of SANS, rheology, and DSC analyses. It was found that, in the 1-15% concentration range, Soluplus micelles can be modeled as spherical core-shell particles with a fuzzy interface, having an average radius of about 22.4 nm, and interacting through a 2-Yukawa potential. These supramolecular aggregates were found to be highly hydrated, with a significant amount of water penetrating deep into the micelles' core. SANS patterns of Soluplus aqueous solutions with concentration 20% to 55% were characterized with the Teubner-Strey model, indicating relatively ordered systems. By exploiting the SANS interaction peak position it was shown that at least until Soluplus 45% w/w, micelles pack themselves together, without disappearing or evolving into different structures, as observed extensively in literature for PNiPAM microgels.[127]

Results and Discussion: Part 3

Soluplus as an encapsulating agent for fragrances in aqueous media

In this chapter, Soluplus is tested as an encapsulating agent for different perfume molecules in aqueous solutions. As mentioned earlier in this thesis, in formulations that include perfume, numerous PRMs with different hydrophobicity and molecular characteristics can be mixed to form an industrial perfume accord. As the constituent of Soluplus also present different degrees of affinity to water, this polymer has the potential to be used as host for different PRM molecules with an ample range of hydrophobicity.

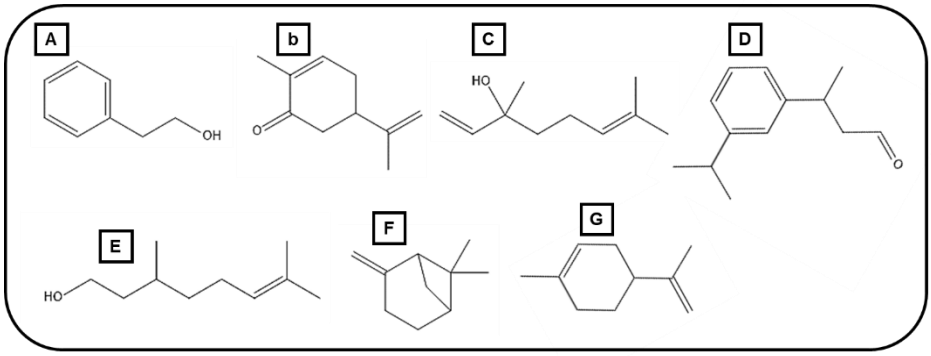

Scheme 5.1. Molecular structures of the PRMs used in this work. A) 2-phenyl ethanol; B) L-carvone; C) linalool; D) florhydral; E) β-citronellol; F) α-pinene and G) R-limonene

In order to assess the potential of Soluplus as an encapsulating/solubilizing/dispersing agent for fragrances in aqueous media, a series of seven perfume raw materials, having different hydrophobicity, but also different molecular characteristics was selected. Hydrophobicity of molecules can be expressed by their octanol/water partition coefficient (*log* K_{ow}), a parameter commonly used to classify fragrances in several perfume encapsulation studies.[34,38,72,139,140] The selected PRMs were 2-phenyl ethanol (PE, *log* K_{ow} = 1.36), L-carvone (CAR, *log* K_{ow} = 2.74), linalool (LIN, *log* K_{ow} = 2.97), florhydral (FLO, *log* K_{ow} = 3.02), citronellol (CIT, *log* K_{ow} = 3.3), α-pinene (PIN, *log* K_{ow} = 4.44) and limonene (LIM, *log* K_{ow} = 4.57) whose

molecular structures are reported in **Scheme 5.1**. Since industrial formulations are composed by high water amount and only few percent of the encapsulating agent and active, our studies were focused in the concentration range that is interesting for such applications. Encapsulation tests were carried out with solutions containing 94% water, 5% polymer and 1% perfume.

First, aqueous solutions with 5% Soluplus and 1% perfume (one of the seven PRMs of **Scheme 5.1**) were prepared as explained in the Materials and Methods chapter, and they were first visually inspected. Except for 2-phenyl ethanol, all the samples were milky solutions, suggesting the presence of dispersed objects bigger than 300-500 nm. Optical micrographs of the samples can be seen in **Figure 5.1**. The presence of micron-sized spherical particles was revealed, for six out of the seven PRMs-based systems investigated. Such systems are usually metastable, but inclusion in an industrial formulation can be done when the viscosity is increased e.g., by using structurers. In our studies, samples with the PRMs were stable for >3 months, while coalescence of the supramolecular structures when observed under the microscope was not evident during this period of study.

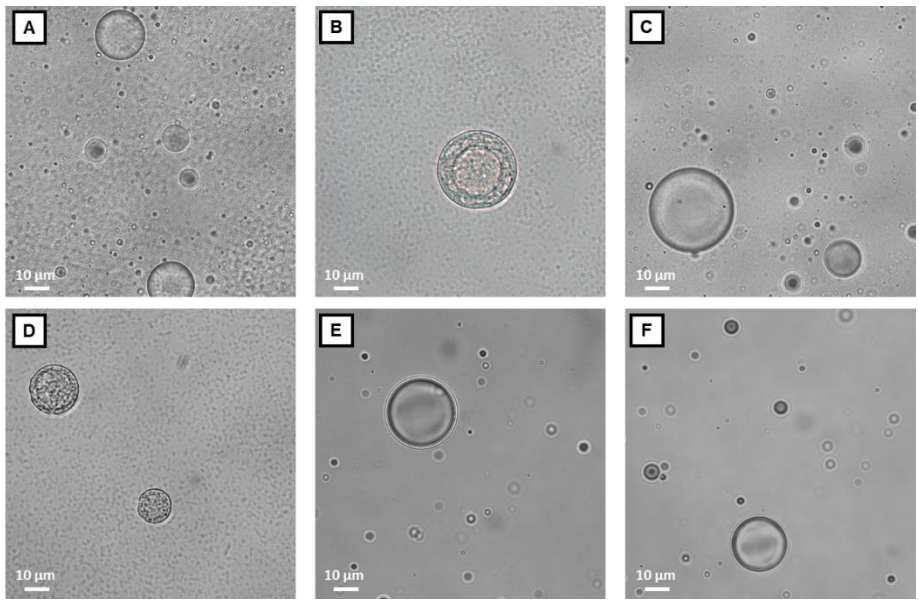

Figure 5.1. Optical microscope images of 94% w/w water, 5% polymer and 1% of each of the perfumes: A) L-carvone, B) linalool, C) florhydral, D) β-citronellol, E) α-pinene and F) R-limonene.

Starting from the sample with 5% Soluplus and 1% 2-phenyl ethanol, which was macroscopically single-phased and transparent, the presence of micron-scale objects was excluded. This sample was studied by means of SANS and the pattern can be seen in **Figure 5.2**. For the fitting of the SANS pattern, the fuzzy sphere form factor with a 2-Yukawa structure factor was used, the same one employed for Soluplus micelles without PRMs (Eq. 4.3).

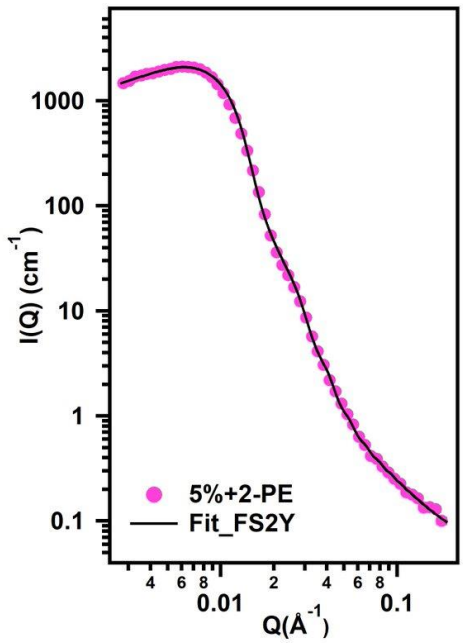

Figure 5.2. SANS patterns obtained for the sample containing 5% Soluplus / 1% PE in D_2O. Markers represent experimental points and solid line represents fitting with the fuzzy sphere – 2Y model (Eq. 4.3).

The model fits well the experimental data and the obtained fitting parameters can be seen in **Table 5.1**. The core radius of the micelle increased from 17.8 (±0.7) nm to 22.2 nm (±0.4) upon the addition of PE to 5% Soluplus. This result, together with the decrease of the core SLD from 4.8 to 4.0 ($\times 10^{-6}$) $Å^{-2}$, indicated that the PRM was solubilized in the polymeric micelle, likely replacing some D_2O molecules. Low *log* K_{OW} fragrances like PE tend to partition themselves between the dispersed, more hydrophobic phase and the aqueous bulk solvent, thus causing a slight swelling of micelles.[104] The behavior of PE when added to Soluplus micelles in water is consistent with the Soluplus micelles' core being not purely hydrophobic, as evidenced by the

SANS characterization reported in Results and Discussion Part 2. In fact, the abundant presence of VCL units and the significant amount of penetrating water molecules create an environment preferably suited to encapsulate/solubilize low hydrophobicity PRMs, such as PE.

Table 5.1. Structural parameters obtained by fitting the 5% Soluplus / 1% 2-phenyl ethanol in D_2O SANS curve with the fuzzy sphere – 2Y model. The parameters for which no error is given were kept fixed during the fitting procedure

Soluplus 5% w/w + PE 1% w/w	
Volume fraction	0.24
Core radius, R_{core} (Å)	222 ± 4
Core polydispersity	0.27
Fuzziness, σ (Å)	25
Core SLD ($Å^{-2}$)	4.0 10-6
Solvent SLD ($Å^{-2}$)	6.4 10-6
Lorentzian scale	5.3
Lorentzian length (Å)	50
Attraction strength	4.12 ± 0.05
Attraction range parameter	28.0 ± 0.1
Repulsion strength	-1.00 ± 0.01
Repulsion range parameter	1.50 ± 0.01

The same sample was further investigated with {^{1}H-^{1}H}-NOESY NMR to give more insights on the fragrance - polymer interactions and the correlation map can be seen in **Figure 5.3.** From the map it is clear that no strong correlation between the protons of PE and those of Soluplus is present. This can be explained, considering that PE molecules were included in the micelle in the form of tiny droplets or nano-domains. The perfume is not molecularly distributed in the micelles but is instead forming a core (single droplet) or more pools of solvent distributed in the volume of the micelles. From the NOESY experiment it is evident that 2-phenyl ethanol molecules can be thought to mostly interact among themselves with only the few of them being spatially in very close contact with the polymer, thus causing a slight swelling of the micelle.

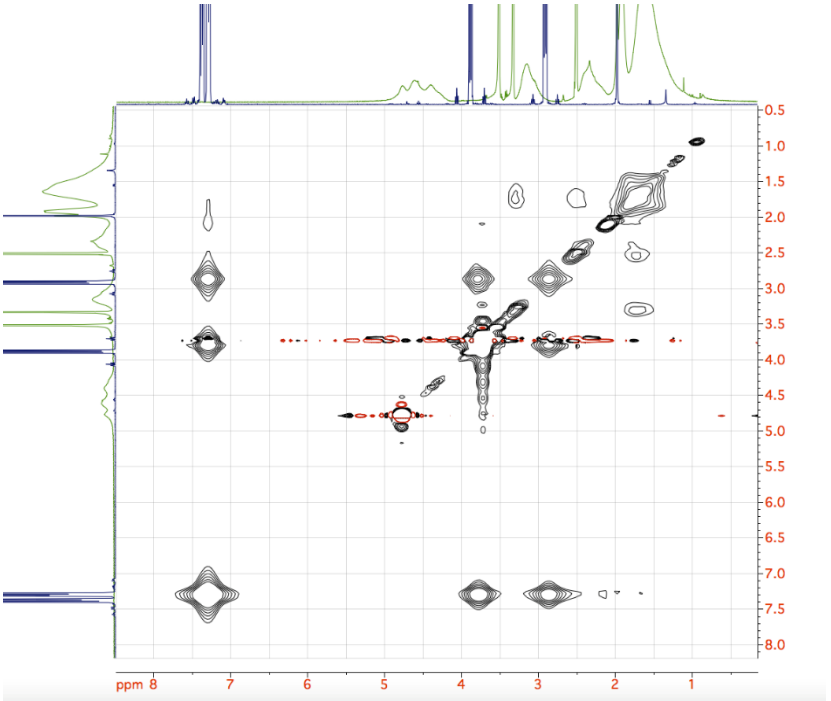

Figure 5.3. NOESY map of 5% Soluplus / 1% 2-phenyl ethanol in D_2O. On both axis ^{1}HNMR spectra of 2-phenylethanol in $CDCl_3$ and Soluplus in DMSO-d_6 are respectively depicted in blue and green. Such spectra are use as indicators of specific resonances of the two systems.

Samples prepared with the remaining six PRMs, and containing micron-size objects, were investigated with Confocal Laser Scanning Microscopy (CLSM) using rhodamine-B labelled Soluplus, and Confocal Raman Microscopy (CRM). CLSM micrographs can be seen in **Figure 5.4**, where the fluorescently labelled polymer can be tracked. 2D Raman mapping was performed in the spectral region between 1000 - 3400 cm^{-1}, to localize the perfume and water in the aggregates using specific Raman resonances. In this way, the three components of the system can be localized. The generated 2D maps can be seen in **Figure 5.5**. Reference Raman spectra of pure Soluplus and PRMs can be found in Figures S11-S17 of Paper II.

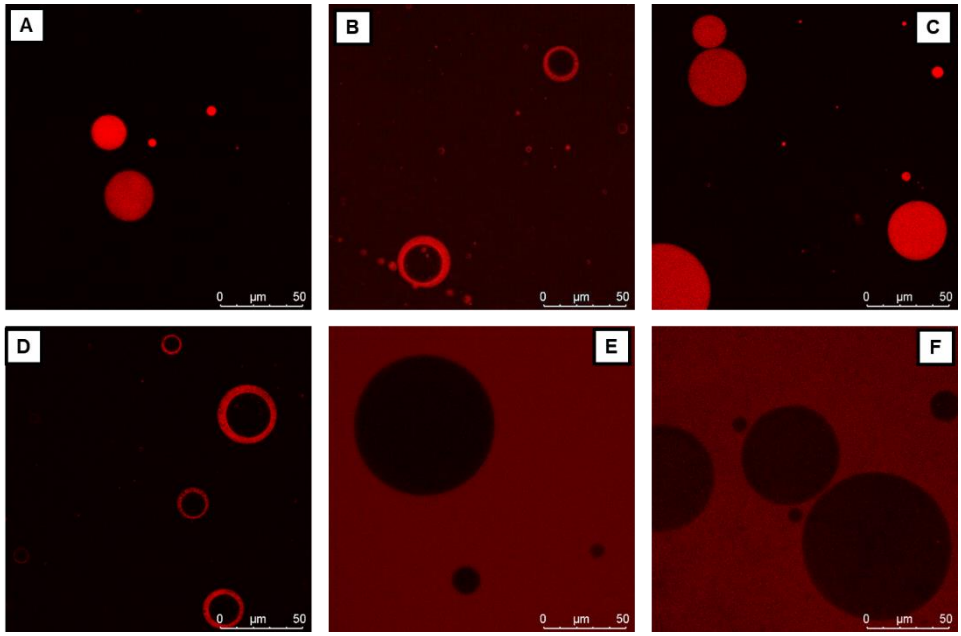

Figure 5.4. Confocal scanning laser microscopy images (63× water-immersion objective) of 94% w/w water, 5% polymer and 1% of each of the perfumes: A) CAR, B) LIN, C) FLO, D) CIT, E) PIN and F) LIM.

For FLO, CAR, LIN, and CIT, CLSM images revealed the presence of large polymeric aggregates of size between 10 and 100 µm. FLO and CAR led to the formation of matrix-type polymeric capsules where the polymer is embedded in the whole capsule area. PRM was, then, tracked with CRM in the capsules, using e.g. for FLO the Raman signal of its aromatic ring vibrations at around 1000 cm^{-1}, and the 2D mapping generated can be seen in **Figure 5.5C1**. This evidenced that both FLO and CAR are present as diffuse in the whole volume of polymeric matrix-type capsules together with Soluplus.

The case of LIN and CIT stands out, due to the presence of objects remindful of polymersomes or multiple w/o/w emulsions, clearly visible in CLSM images (**Figures 5.4B**, **5.4D**). A further insight on these microstructures came from CRM 2D maps, generated from the signal of the C=C stretching of the PRM at 1640 cm^{-1}, and the C-H stretching signal at 2920 cm^{-1} (see **Figure 5.5**).[141–144] In fact, LIN and CIT drive the formation of core-shell capsules, with the polymer and the PRMs that synergistically form a shell around an aqueous core, while no perfume was detected in the water inside or outside

the polymersomes. In these systems, the two PRMs seem to behave as a sort of cosurfactants for the polymer, creating vesicle-like structures. This phenomenon was proposed for fragrances with intermediate *log* K_{ow} values interacting with polymeric micelle systems.[104]

Finally, the two perfumes with the higher *log* K_{ow} values (*i.e.* higher hydrophobicity), LIM and PIN, were found to drive the formation of what appear to be o/w emulsions: indeed, CLSM images show highly polydisperse dark aggregates against a red fluorescent background, suggesting that a polymer-rich aqueous phase surrounds and stabilizes a dispersion of polymer-less droplets. SANS measurements prove the micellar nature of the polymer-rich phase, as the scattering profiles of LIM and PIN samples are identical to the ones of 5% Soluplus (**Figure 5.6**). CRM analyses (**Figure 5.5E and 5.5F**), on the other hand, show that the two PRMs are only located inside the dark droplets seen in CLSM images. These observations support the hypothesis that Soluplus micelles act as a stabilizing agent for a dispersion of perfume droplets. It is worth noting that the Raman signal of C=C and C-H stretching coming from Soluplus was much lower than the one coming from PRMs (see reference Raman spectra of pure materials in Supporting Information Figures S11-S17, Paper II); this is why in **Figures 5.5E** and **5.5F** Soluplus is not detectable outside the droplets, in the polymer-rich aqueous bulk phase. Moreover, quite interestingly, none of these hydrophobic perfume droplets appeared to coalesce upon contact with each other; this observation, corroborated by the long-term (>3 month) stability of the suspensions, suggests a remarkable elasticity of the interfacial polymer film that likely covers the droplets surface, leading to a particularly efficient stabilization mechanism against Ostwald ripening.

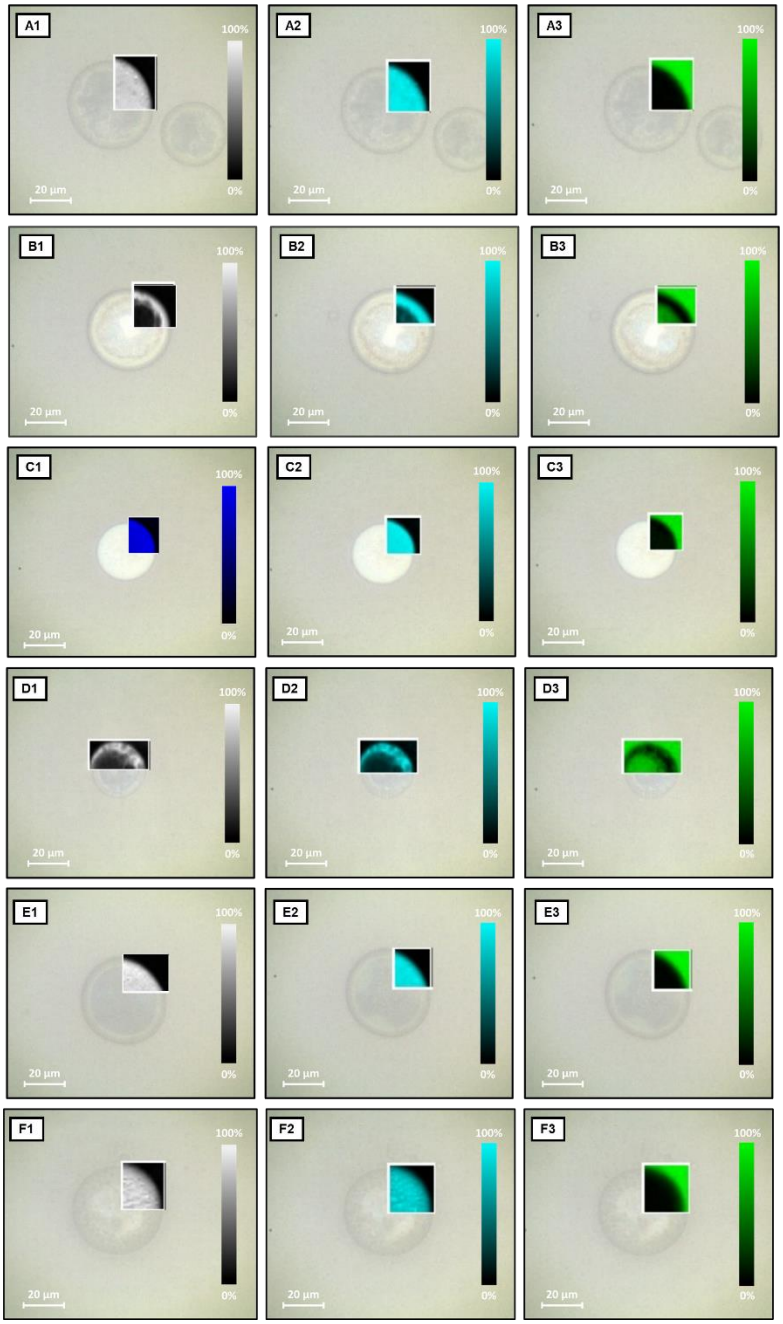

Figure 5.5. Raman 2D mapping of 94% w/w water, 5% polymer and 1% of each of the perfumes: A) CAR, B) LIN, C) FLO, D) CIT, E) PIN, F) LIM. The different colors represent tracking of the different Raman signals. White signal: 1640 cm^{-1} (C=C stretching band); Dark blue signal: 1000 cm^{-1} (aromatic ring stretching); Light blue signal: 2920 cm^{-1} (C-H stretching band); Green signal: 3400 cm^{-1} (O-H stretching band).

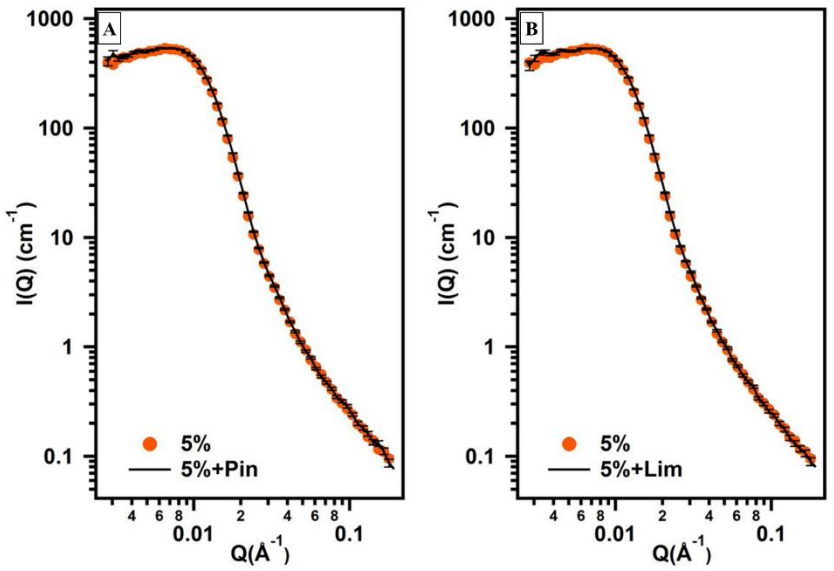

Figure 5.6. SANS patterns obtained for the samples containing 5% Soluplus and 1% A) α-Pinene or B) R-Limonene in D_2O. Markers represent the experimental points of 5% Soluplus aqueous solution in the absence of PRM and solid lines represents the experimental data of the two samples with PRM.

These observations indicate that no clear relationship can be found between the *log* K_{ow} of the seven PRMs and the structures they form with Soluplus. In other words, even if *log* K_{ow} is widely used to classify the nature of PRMs in the formulation of home- and beauty-care products,[34,38,72,139,140] this parameter is not enough to predict the microstructure of PRM-based systems in the presence of an amphiphile polymer, such as Soluplus. However, if, besides the hydrophobicity/hydrophilicity balance, additional parameters such as the presence of specific functional groups and molecular conformation are considered, a clearer picture emerges. Four different structures were identified in the PRM/Soluplus/water systems: i) swollen micelles (for PE); ii) matrix-like particles (for FLO and CAR); iii) vesicle-like particles (for CIT and LIN); iv) perfume emulsion droplets stabilized by polymer micelles (for PIN and LIM). By combining the hydrophobicity, the presence of given functional groups, and the molecular conformation of the seven PRMs, these four structures can be justified and understood. More in detail, PE is sufficiently hydrophilic that it is partitioned between the aqueous bulk and the micellar phases. The small fraction included in the micellar phase is easily solubilized into the slightly hydrophobic core of Soluplus micelles. FLO and CAR are

characterized by a medium hydrophobicity, rather bulky molecules and the presence of carbonyl groups. This makes them very similar to the repeating monomeric units of Soluplus chains, and a random PRM/polymer mixing is particularly favored, resulting in the formation of matrix-like droplets. On the other hand, CIT and LIN are both fairly linear molecules terminated with hydroxyl groups. This gives them a slight amphiphilic character, which is reflected in their "co-surfactant" behavior, resulting in the formation of core-shell vesicle-like structures. Finally, LIM and PIN are the most hydrophobic of these PRMs; they are bulky molecules with no polar groups. Consequently, they do not mix neither with water, nor with Soluplus, generating an emulsion-like structure, stabilized by the presence of Soluplus micelles in the aqueous bulk phase.

In this chapter Soluplus was successfully tested as a potential stabilizing agent for seven fragrance molecules exhibiting different hydrophobic character and molecular characteristics. Besides showing that Soluplus can be effectively employed to form a variety of stable structures for the formulation of perfume-based colloidal systems, the main result of these experiments is the proof that *log* K_{ow} is not enough to predict the structure and understand the complex interaction that takes place when a perfume molecule interacts with an amphiphilic polymer, such as Soluplus. In fact, these experiments prove that the nano- and micro-structure of complex systems can be efficiently predicted and described only if other parameters are also considered, such as the presence of specific functional groups and molecular conformation of the PRM. These factors can generate specific and uneasily predictable interactions between small PRM molecules and polymer chains, which are reflected on a bigger scale in the micro-structure of the system. Accordingly, PRMs having different hydrophobicity but similar molecular structure and functional groups may interact in a similar way with a given polymer. Or, PRMs having very similar hydrophobicity but slightly different molecular structures may interact in a completely different way with a given polymer.

Results and Discussion: Part 4

Self-assembly, perfume encapsulation and performance of PEG-*g*-(PVAc-*co*-PVCL) copolymers in SLFE

The objective of this chapter is to test the graft copolymers as perfume encapsulation systems in the environment of a model industrial formulation, a simplified fabric enhancer (SLFE). Different polymers (commercial and synthesized within SAMCAPS) were compared to understand how small variations of the polymer properties (e.g. molecular weight, grafting degree, chemical moieties) affect capsule formation, self-assembly and the performance of the technology. These variations might be key for the industry and the sustainability of the product. The objective is always to provide the highest consumer delight at the highest efficiency. When free perfume is used in the formulation, deposition on fabrics can be low,[145] since a great amount can be washed off during the rinse cycle. The use of encapsulation technologies enables a more efficient use of the perfume improving the sustainability of the product.

6.1. Self-assembly of PEG-*g*-(PVAc-*co*-PVCL) polymers in SLFE

For our studies, SLFE was selected as model formulation since plenty of fabric enhancer brands in the market today already comprise perfume microcapsules (e.g. Lenor, Comfort, Downy, Ensueno). A liquid fabric enhancer product works by depositing lubricating ingredients on the fabric, aiming to make it feel softer, reduce static cling, and impart a fresh fragrance. For research purposes, a simplified fabric enhancer formulation has been used, where the liquid matrix was composed by the softening agent (a cationic surfactant), water (>88.9 – 94.9% H_2O) and other minors (e.g. hydrochloric acid and formic acid, <0.1%).

Cationic surfactant is present in the SLFE matrix in the form of vesicles. Preparation of the SLFE matrix was carried out by the Procter&Gamble company process making. Two batches of SLFE have been used, containing

one population (SLFE_A) or two populations (SLFE_B) of cationic vesicles. For more details on the different SLFE matrices used, please refer to **Table 2.1**. Optical micrographs of the SLFE matrix before any additions, are presented in **Figure 6.1**. The SLFE can contain monodisperse cationic vesicles (~0.2 μm in diameter, **Figure 6.1A**) or two populations of vesicles, one of ~0.2 μm and a second one of ~8 μm, **Figure 6.1B**.

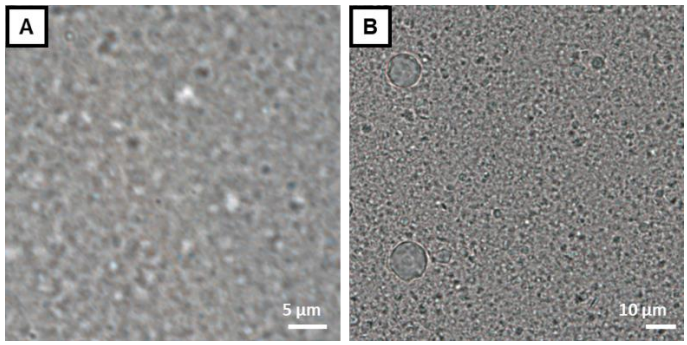

Figure 6.1. Optical micrographs of the cationic SLFE matrix containing cationic vesicles. A: SLFE_A1, presence of monodisperse cationic vesicles (~0.2 μm in diameter); B: SLFE_B2, presence of two populations of vesicles, (one of ~0.2 μm and a second one of ~8 μm). Surfactant level is 7% w/w in both formulations.

Two polymers were used for the studies in SLFE, based on the PEG-*g*-(PVAc-*co*-PVCL) structure (the structure can be seen in **Scheme 4.1**). The first polymer studied was the commercially available Soluplus, discussed extensively in Results and Discussion Part 2 and 3 of the thesis. An additional polymer, named *S2* was used and compared to Soluplus by means of encapsulation abilities in SLFE and performance after deposition on fabrics. Polymer S2 was replicated two times in order to confirm that the polymer S2 was reproducible (batches are named *S2A* and *S2B)* and that the two batches were performing the same. Polymer S2 was synthesized within the SAMCAPS network. A paper regarding the synthesis application of polymer S2 as perfume carrier is currently in preparation. The two polymers are based on the same molecular structure, but differ in some of their properties, including M_w, cloud point temperature (CPT) and grafting degree (GD). The main differences between the two polymers are summarized in **Table 6.1**.

Table 6.1. Properties of the two PEG-*g*-(PVAc-*co*-PVCL) polymers: Soluplus (commercial), and S2, batches S2A and S2B (synthesized within SAMCAPS network). CPT: cloud point temperature; GD: grafting degree, PVAc-*co*-PVCL units per PEG unit.

	Polymer	**M_w** (kDa)	**PEG:VAc:VCL ratio**	**CPT** (ºC)	**GD**
Commercial	Soluplus	90-140	13:30:56	40	1.12
Synthesized within SAMCAPS	S2A	195	15:25:60	21.5	1.46
	S2B	193	14:25:61	20.8	1.45

The small differences on the polymer properties have led to different self-assembly properties. The cloud point temperature (CPT) is the temperature above which a transparent solution can undergo either a liquid-liquid phase separation (LLPS) to form a stable colloidal suspension or a liquid-solid phase transition to form a suspension that tends to precipitate. LLPS induced by coacervation can spontaneously occur in a polymer's solution when temperature rises above the CPT. **Figure 6.2** shows optical micrographs of S2A and S2B aqueous solutions (concentration 0.5% w/w). The two aqueous solutions exhibiting CPT lower than 25 ºC, and as a result, at room temperature, liquid coacervate droplets are observed. In contrast, aqueous solutions of Soluplus did not undergo LLPS at room temperature, as the CPT of Soluplus is ~40 ºC. Similar coacervates in polymeric aqueous solutions that undergo LLPS upon heating (over their CPT) were observed in other studies, among them poly(acrylic acid)-*graft*-poly(*N,N*-dimethylacrylamide) (PAAc-*g*-PDMAAm),[146] poly(*N,N*-dimethacrylamide-*co*-glycidyl methacrylate) (DMA-GMA),[147] poly(*N,N*-dimethylacrylamide-*co*-*N*-phenylacrylamide) (DMA-*co*-PhAm),[148] and poly(N-vinylcaprolactam-*co*-vinyl acetate) (VCL-*co*-VAc).[149]

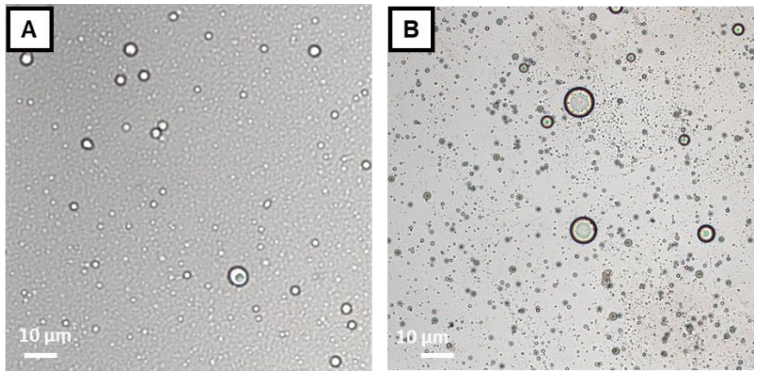

Figure 6.2. Optical micrographs of the coacervate droplets in 0.5% w/w aqueous solutions of polymer S2. A: Batch S2A and B: S2B at room temperature (25 ºC).

Within the numerous studies on synthetic nonionic surfactant solutions that undergo LLPS at temperature >CPT, it is concluded that this parameter is highly affected by several properties of the amphiphile, including its M_w, graft length and the ratio between its components.[65] Polymer S2 has significantly higher M_w (195 and 195 kDa, for S2A and S2B respectively) compared to Soluplus (90 – 140 kDa). The two polymers are composed by a PEG 6000 backbone, and thus the higher molecular weight of S2 arises from a longer PVAc-*co*-PVCL graft chain. Considering that the PEG 6000 backbone is the purely hydrophilic part of the amphiphilic polymer, by increasing the length of the PVAc-*co*-PVCL graft chain the hydrophobic (compared to PEG) part of the amphiphile is rising. This can explain the lowering of CPT for polymer S2 compared to Soluplus. CPT of a polymer solution shows a reverse relation with the polymer's M_w, and thus the CPT decreases with increasing M_w.[150–152] Longer hydrophobic chain, and as a consequence higher M_w, likely exhibits increase in the hydrophobic polymer–polymer interactions, resulting in a decreased CPT.[148,153,154] Another property of the graft copolymers that affects CPT, is the grafting degree. CPT was found to decrease with increasing the grafting degree of the polymer, in a study involving the PVCL-*g*-PEO graft copolymer. By increasing the degree of branching, the competition between PEO and PVCL to interact with water is diminished by weakening the interactions of VCL with water in the vicinity of PEO, promoting LLPS.[155,156] Taking into account that polymer S2 was synthesized with free radical polymerization, control of the grafting density was not possible. Additionally, it was attempted to obtain the value of grafting density through inverse-gated proton decoupled ^{13}C-NMR, but a detectable band clearly allied with the

resonance of the PEG's grafted methynes was not possible to be identified. As a result, any differences between the polymers regarding their grafting density and its effect on the self-assembly properties will not be considered here.

Interestingly, the coacervate droplets or micro-capsules were observed for S2 (0.5% w/w) when instead of water, SLFE was used as matrix. **Figures 6.3A and 6.3B** show the fluorescence micrographs of the capsules at 25 ºC, using rhodamine-B labelled polymers, indicated with red color. The coacervate droplets were found to increase in size (from 5-10 μm to 20-50 μm) when the cationic vesicle size increased (cationic surfactant level kept constant to 7% w/w) as can be seen in **Figure 6.3C.** This suggests that the micro-capsules are possibly formed on the interface between the cationic vesicle and the water medium, and thus, bigger size vesicles (with a smaller curvature) are leading to larger capsules (with a smaller curvature).

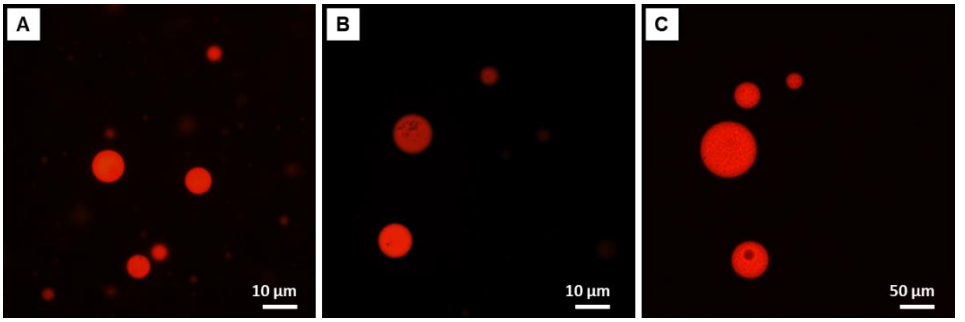

Figure 6.3. Fluorescence micrographs of the coacervate droplets formed in SLFE with 0.5% w/w of polymer S2. A: batch S2A and B: batch S2B in SLFE_A1. C: batch S2B in SLFE_B2, containing larger cationic surfactant vesicles at room temperature (25 ºC).

As a next step, the two polymers (Soluplus and S2) had been tested in SLFE in the presence of several PRMs. Many PRMs were tested in the presence of the two polymers: 2-phenyl ethanol (PE, *log* K_{ow} = 1.36), methyl anthranilate (MA, *log* K_{ow} = 1.88), L-carvone (CAR, *log* K_{ow} = 2.74), linalool (LIN, *log* K_{ow} = 2.97), florhydral (FLO, *log* K_{ow} = 3.02), citronellol (CIT, *log* K_{ow} = 3.3), α-pinene (PIN, *log* K_{ow} = 4.44) R-limonene (LIM, *log* K_{ow} = 4.57), iso-E super (IES, *log* K_{ow} = 5.12) and habanolide (HAB, *log* K_{ow} = 5.53). The molecular structures of MA, IES and HAB are reported in **Scheme 6.1**, while for the molecular structures of the rest of the PRMs refer to **Scheme 5.1** in Results and Discussion Part 3. Additionally, an industrial perfume accord (*log* K_{ow} =

6.99), which is a mixture of around 60 single perfume raw materials, was used. Three PRMs that are present in the industrial perfume accord in high percentage are iso-E super (14% w/w), habanolide (8% w/w) and linalool (4% w/w).

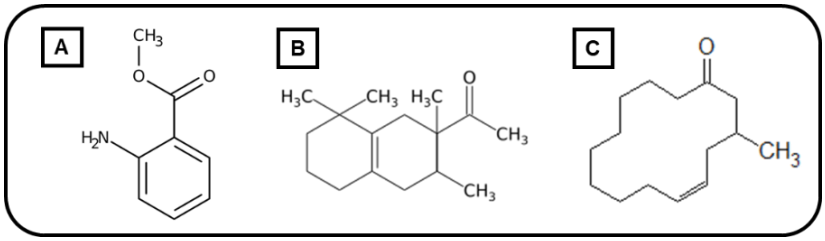

Scheme 6.1. Molecular structures of the PRMs A) methyl anthranilate; B) iso-E super and C) habanolide.

Samples prepared with different PRMs, or the industrial perfume accord, were observed with the fluorescence microscope, using rhodamine-B labelled polymers. Selected fluorescence micrographs can be seen in **Figure 6.4** for the PRMs L-carvone, R-limonene and habanolide. In the presence of all the studied PRMs, but also in the presence of the industrial perfume accord, Soluplus did not lead to the formation of micro-capsules. A red fluorescent background was instead observed (**Figure 6.4A1 – 6.4A3**), suggesting a polymer-rich solution or particles with size below the observation limit of the microscope. On the other hand, micro-capsules were observed in the case of polymer S2, for batch S2A (**Figure 6.4B1 – 6.4.B3**) and batch S2B (**Figure 6.4C1 – 6.4C3**), as evident by the red coloured polymer-rich structures in the images. It is evident by our studies that the two batches of polymer S2 behave in the same way by means of self-assembly and capsule formation in water and SLFE.

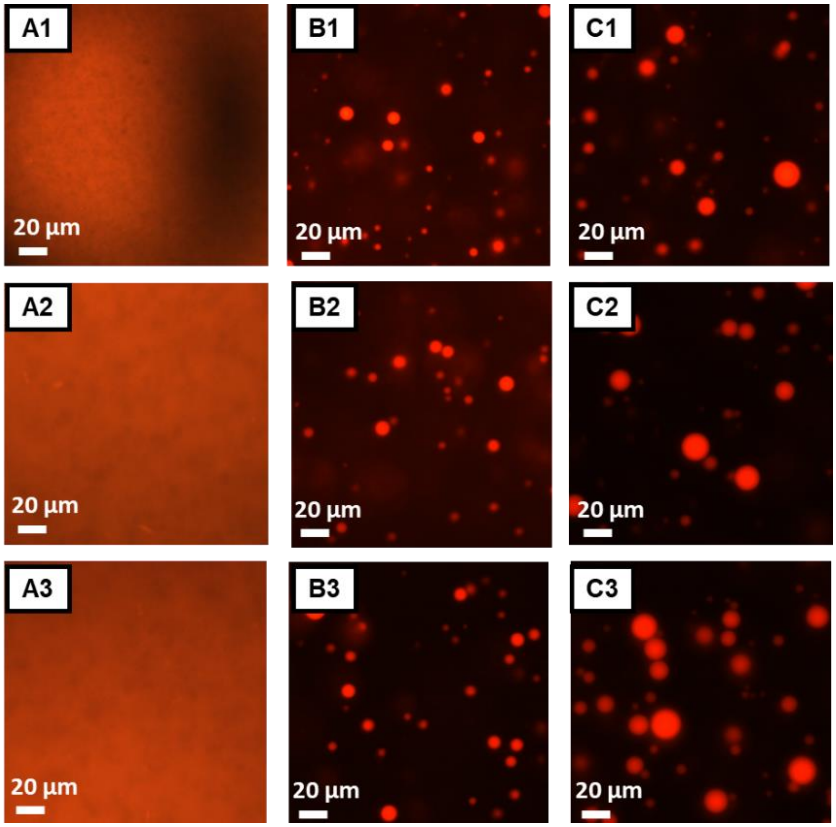

Figure 6.4. Fluorescence micrographs of the coacervate droplets formed in SLFE_A1 with 0.5% w/w of A: Soluplus; B: polymer S2 batch A and C: polymer S2 batch B, at room temperature (25 °C). A1, B1, C1: L-carvone; A2, B2, C2: R-limonene; A3, B3, C3: habanolide.

In general, ionic surfactants (anionic or cationic) are known to increase dramatically the CPT, and as a consequence, the appearance of LLPS coacervate droplets is observed at higher temperatures. CPT can, for example, raise by 40°C in the presence of surfactants in concentrations much less than the amphiphilic polymer's CMC. The increase in CPT is attributed to the induced polymer-surfactant interactions, leading to the formation of charged polymer chains, and thus to inter-chain repulsion.[157–159] In this case, the repulsive electrostatic forces are in competition with the attractive hydrophobic forces that promote the self-assembly of a polymer in the solution.[160] Interestingly, coacervates droplets of polymer S2 were resistant to 7% w/w cationic surfactant addition, as evident in **Figure 6.4B** and **Figure 6.4C**. Here, the cationic surfactant concentration is 14 times higher than the one of the polymer's. The self-assembly properties of polymer S2 are thus

attractive for perfume encapsulation in industrial home- and personal care formulations that are rich in ionic surfactants. Increase of the surfactant content from 7% w/w (SLFE_A1) to 11% w/w (SLFE_A2) decreased the number of micro-capsules as evident in **Figure 6.5**. This behaviour was expected, as increase in the cationic level lowers the CPT and thus hampers the self-aggregation of the copolymer as explained above.

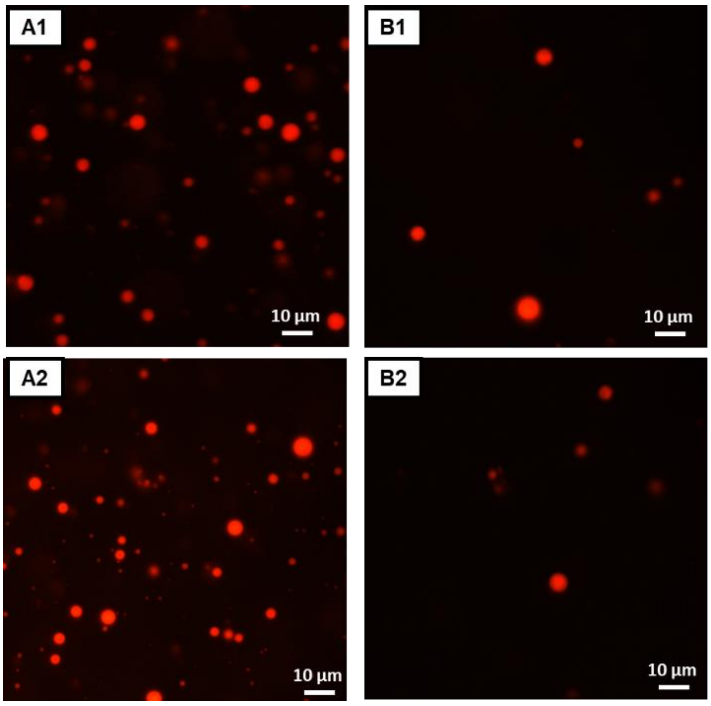

Figure 6.5. Fluorescence micrographs of the coacervate droplets formed in SLFE with 0.5% w/w of polymer S2 (batch B) at room temperature (25 ºC). A: SLFE_A1 and B: SLFE_A2. A1, B1: florhydral; A2, B2: industrial perfume accord.

For confirming the encapsulation of perfume in the polymer S2 capsules in SLFE, a PRM with fluorescence properties, methyl anthranilate, was used (λ_{ex} = 365 nm). MA has its maximum emission peak at 432 nm.[161] **Figure 6.6** shows the fluorescence micrographs of S2 coacervates encapsulating MA, as indicated from the polymer-rich (red signal) and MA-rich (blue signal) structures. In the case of Soluplus, the fluorescent background suggests that the polymer and MA are not forming micro-particles in the solution. Confocal-Raman microscopy will be used in later studies to confirm the encapsulation all of the PRMs used.

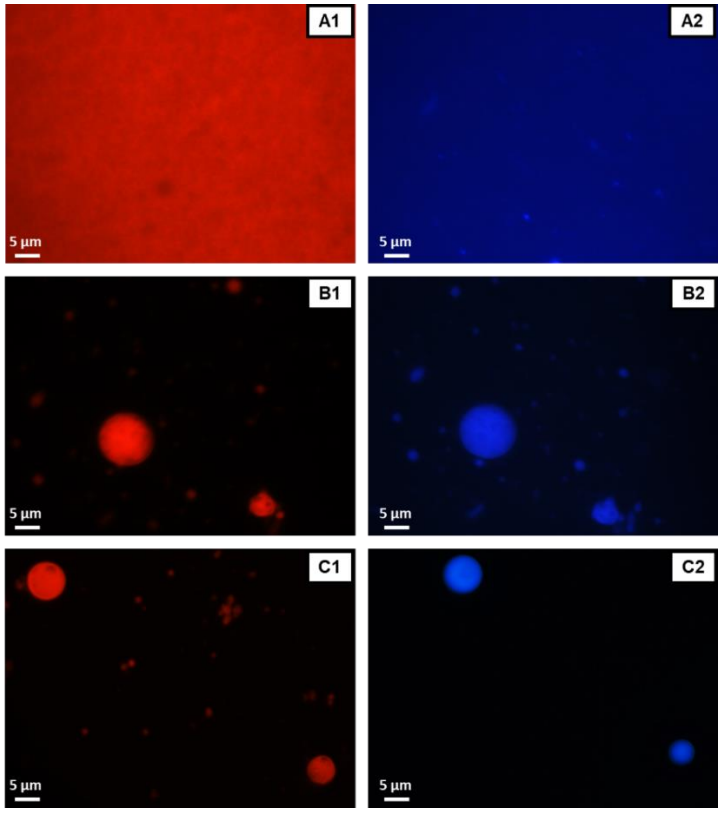

Figure 6.6. Fluorescence micrographs of the coacervate droplets formed in SLFE with 0.5% w/w of A: Soluplus; B: polymer S2, batch A; C: polymer S2, batch B and 0.5% w/w of methyl anthranilate (MA) at room temperature (25 ºC). Red signal: tracking of rhodamine-B labelled polymer; Blue signal: tracking of MA.

6.2. Performance tests after deposition of micro-capsules on fabrics

In the last experimental part of this thesis, the potential application of self-assembled polymeric capsules as perfume carriers in SLFE will be examined. The performance of the encapsulation systems will be evaluated after deposition of the product on fabrics, by means of headspace GC-MS. Headspace analysis is the most used analytical technique for detection and quantification of volatile aroma compounds, and for the evaluation in terms of quality, freshness and safety.[162] Headspace solid phase microextraction (HS-SPME) GC-MS is a rapid, non-separative, solvent-free, and simple method for volatile analysis.[163] HS-SPME-GC-MS has been used here as analytical tool for perfume systems after deposited on fabrics, sampled because of their ability to be vaporized spontaneously due to their volatile

composition. This technique has been widely used to monitor processes that involve microencapsulation of lasting fragrances (in home- or personal care products, disinfectants, insect repellents, etc) especially in textile industry.[164]

For the performance experiments, two methods of deposition were used, as illustrated in **Scheme 6.2**. For the first method, named forced deposition, the SLFE product was spread on cotton fabric pieces using a plastic pipette (**Scheme 6.2A**). In this way the solution is "forced" to be deposited on the fabrics (in other words, directly applied on fabrics), avoiding any losses. The SLFE product was diluted 100 times with water before spreading on fabrics, to mimic washing machine conditions. The second method involved the use of a full-scale wash test (using a washing machine) where the SLFE product with the self-assembled capsules was used in realistic conditions as a fabric enhancer (**Scheme 6.2B**). In both cases, after the deposition, the fabrics were line dried in a closed room for further headspace GC-MS analysis at the desired touchpoint.

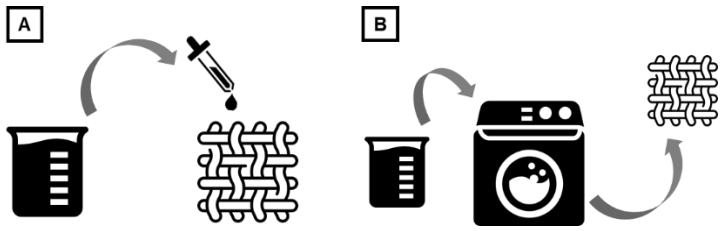

Scheme 6.2. Schematic representation of the two methods of deposition used in our performance studies. A. forced deposition method, B. deposition via a wash test.

The fabrics were analysed at two touchpoints:

- Dried fabrics 24 hours after the deposition (DFO-24 - Dry Fabric Odor after 24 h)
- Dried fabrics 48 hours after the deposition (DFO-48 - Dry Fabric Odor after 48 h)

For all the performance studies, SLFE solutions containing one of the two polymers (Soluplus or S2) and a PRM (or perfume accord) were compared to a reference SLFE solution in the absence of the polymer. In the case of the reference product, the perfume oil was dissolved in the SLFE matrix without encapsulating agent.

For the first performance experiment, following the forced deposition method, the PRM florhydral (FLO, *log* K_{ow} = 3.02) was used as the fragrance compound. For the deposition, knitted cotton fabrics were used. Results after the forced deposition test are summarized in **Figure 6.7**.

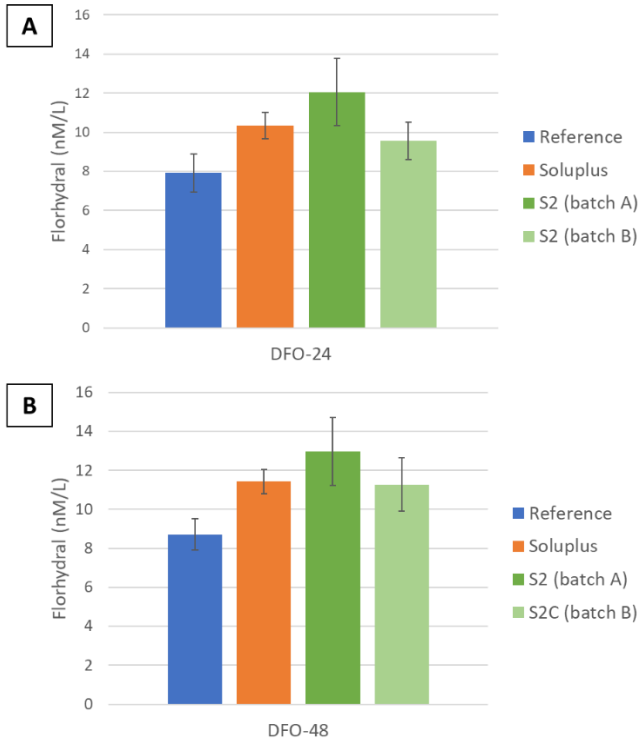

Figure 6.7. Concentration of florhydral (nM/L) detected in the headspace over each cotton fabric in the vial, at the tested touchpoints after the forced deposition of SLFE product. A: DFO-24 (dry fabric odour after 24 h) and B: DFO-48 (dry fabric odour after 48 h). Error bars represent the four replicates carried out per system (reference, Soluplus, S2 (batch A and B)) per touchpoint.

The amount of florhydral in the headspace over each piece of fabric in the vial, at the two tested touch points was detected. The measurement was replicated four times per system (reference, Soluplus, S2A, S2B), per touchpoint (DFO-24 and DFO-48). The benefit of encapsulation was evident on the dried fabrics. After drying the fabrics for 24 hours (**Figure 6.7A**) and 48 hours (**Figure 6.7B**), the detected concentration of florhydral was higher in the headspace over the cotton fabrics when the SLFE product with the polymers was deposited. Thus, in the presence of polymers, when the fabrics

are dried for at least up to 48 hours, the perfume is retained more on the fabric providing a longer-lasting freshness effect compared to the free oil reference. Even though the benefit of encapsulation is evident here after the 48 h dried fabrics, it's hard to say which polymer performs better. Thus, distinctions cannot be made between the polymers within the experimental error.

The second performance experiment was carried out following a full-scale wash test, involving the use of a washing machine. In this case, the self-assembled micro-capsule technology was tested in more realistic and harsh conditions. For the wash test, instead of a single PRM, an industrial perfume accord was used, that is composed by a mixture of around 60 PRMs. For the deposition, in order to mimic a real wash cycle, both knitted cotton fabrics and polyester (PE) fabrics were used, in 80:20 weight ratio (total of 3 kg fabric load). **Figure 6.8** summarizes the results after the wash test, where the total amount of the PRMs was detected in the headspace over each piece of fabric (cotton or polyester) in the vial, at the two touch points (DFO-24 and DFO-48). Four replicates were carried out for each system (reference, Soluplus, S2) per touchpoint, per type of fabric (cotton or polyester). Results were in general similar to the ones obtained from the forced deposition. The benefit of encapsulation was evident for the 24-hour (**Figure 6.8A**) and 48-hour dried fabrics (**Figure 6.8B**) after the wash test. On the dried fabrics, the total detected concentration of PRMs was higher in the headspace over the fabrics with the polymeric SLFE solutions, with the benefit of encapsulation being more pronounced after 48 hours of drying. Again, distinctions between the performance of the different polymers are not possible taking into account the experimental error. This observation, common for both the deposition methods used, can be attributed to the nature of the self-assembled structures. A self-assembly system is affected by changes in the concentration of its components, leading to a de-formation of structures or their re-arrangement into a different phase. Thus, dilution of the product during washing conditions can lead to the dissociation of the micro-particles present in the case of polymer S2. The enhanced performance when one of the polymers is added in the SLFE solution, might be coming from a process called "polymer-assisted deposition", where surface – polymer – fragrance interactions promote a better deposition of the perfume, compared to when the volatile is solubilized in the product without encapsulating agent. This phenomenon will

not be further investigated here, as it is the subject of study of another project within the SAMCAPS network.

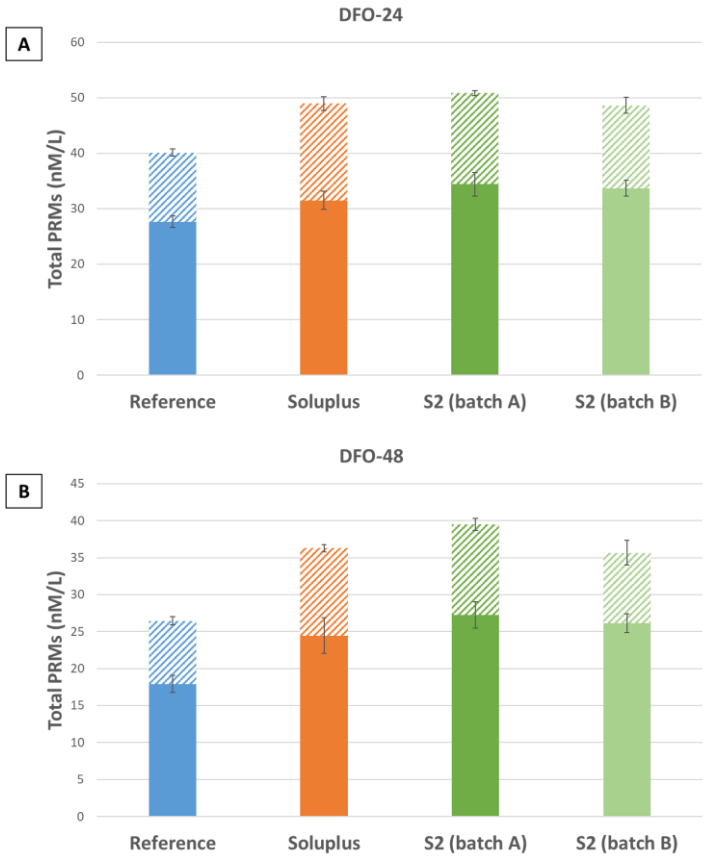

Figure 6.8. Total amount of PRMs (nM/L) detected in the headspace at the tested touchpoints after the wash test using SLFE product on cotton and polyester fabrics. A: DFO 24h (dry fabric odour after 24 h) and B: DFO 48 h (dry fabric odour after 48h). Error bars represent the four replicates carried out per system (reference, Soluplus, S2 (batch A and B)) per touchpoint. Line-filled bars represent the detected amount of PRMs in the headspace over polyester fabrics. Dark-coloured bars represent the detected amount of PRMs in the headspace over cotton fabrics.

The last experimental part of the thesis was focused on the application of the new technology, the self-assembled polymeric micro-capsules, as perfume carriers with potential use in industrial liquid formulations. As target application product, the SLFE matrix was used, with main component a cationic surfactant in the form of vesicles. Two polymers based on the PEG-*g*-(PVAc-*co*-PVCL) but with some different properties (Mw, grafting degree,

cloud point temperature) were used, one commercial (Soluplus) and one synthesized within the SAMCAPS network (polymer S2). Polymer S2 (replicated in two batches) showed enhanced self-assembly properties and found to form stable and resistant micron-sized coacervate droplets in the SLFE. The two batches of S2 (S2A and S2B) were performing the same by means of self-assembly and encapsulation studies and thus the polymer was reproducible. Performance tests were carried out for the first time, to test our technology, via either the forced deposition of SLFE on fabrics, or via full-scale wash tests in washing machines. Headspace GC-MS analysis showed an enhanced performance of the product when amphiphilic graft copolymers where present, that was more pronounced after 48 hours of drying the fabrics. Distinction between the performances of the different polymers was not possible, showing that small variations between the polymers' properties can affect self-assembly in the solution, but are not enough to cause a significant change of its performance upon deposition and wash conditions. The technology is thus robust, and small differences on the polymer synthesis / structure are not affecting the performance. This is important from an industrial point of view where broad specifications of the raw are preferred. Our experiments have given a first idea on the potential of the self-assembly of amphiphilic graft copolymers as a new, sustainable method of perfume encapsulation that needs less energy for the formation of capsules, avoids the use of organic solvent and time-consuming synthetic steps. On the other hand, there is still a long way to go and many things to understand through fundamental research, until having this technology ready for a marketed product.

Conclusions

The topic of this PhD thesis was the self-assembly of copolymers and capsule formation in complex fluids. In this thesis, we reported specifically on the use of amphiphilic graft copolymers, with biocompatible and biodegradable properties, for perfume encapsulation with potential application in industrial liquid products. Perfume appears as an active ingredient in numerous consumer products, with main fields of application household care, personal, food and health care products. The fragrance can serve different purposes i.e. provide a pleasant scent, the feeling of cleanness, or transfuse pharmacological properties to a product. Encapsulation of perfume is essential for the protection of the volatile from evaporation and degradation upon environmental conditions ensuring a longer shelf live. Currently, perfume encapsulation market needs more sustainable and less time-consuming technologies. In this PhD thesis we are exploring the potentials of perfume encapsulation by taking advantage of self-assembly, a simple, spontaneous, and sustainable process. The experimental part of this work was divided in four parts and the main conclusions extracted are reported here.

The first experimental part reported on the investigation of the phase behaviour of PEG-*g*-PVAc aqueous solutions in the presence of three common PRMs with different water affinities as expressed by their octanol/water partition coefficients, 2-phenyl ethanol (*log* K_{ow} =1.36), L-carvone (*log* K_{ow} = 2.74) and α-pinene (*log* K_{ow} = 4.44). We studied the ternary system in the 10-90% concentration range and the effect of the actives' hydrophobicity on the polymorphism of PEG-*g*-PVAc. Our studies pointed out the role of perfume's hydrophobicity by showing that 2-phenyl ethanol and L-carvone can both be encapsulated, while α-pinene is too hydrophobic and it phase-separates at all ratios. The two successfully encapsulated fragrances lead to similar phase behaviours, as both phase diagrams included SCNPs, lamellar liquid crystalline phases and micro-capsules, but the formed nanostructures exhibited differences. 2-phenyl ethanol could be encapsulated in SCNPs or matrix-like capsules with the perfume showing no preference for one of the two polymer segments, while the slightly more hydrophobic L-carvone was encapsulated in the core of the core–shell SCNPs or micro-

capsule structures. The borders of the phase diagram regions also differ, with carvone for example forming L_α phases covering a bigger area of the phase diagram, able to swell upon increase perfume concentration.

The second experimental part reported on Soluplus or PEG-*g*-(PVAc-*co*-PVCL) self-assembly properties in aqueous solutions. Soluplus' aqueous solutions were characterized for concentration up to 70% (w/w). Results showed that in the 1-15% concentration range, Soluplus was forming spherical micelles with a fuzzy interface and average radius of about 22.4 nm, interacting through a 2-Yukawa potential. These supramolecular aggregates were found to be highly hydrated, with a significant amount of water penetrating deep into the micellar core. SANS patterns of Soluplus aqueous solutions with higher concentration (up to 55%) were characterized with the Teubner-Strey model, indicating the presence of ordered systems. By exploiting the SANS interaction peak position, it was shown that at least until Soluplus 45% w/w, micelles pack themselves together, without disappearing or evolving into different structures.

In the third chapter, Soluplus was successfully used as perfume encapsulation agent for seven common fragrances with different hydrophobic character, functional groups and molecular conformation: 2-phenyl ethanol (*log* K_{ow} = 1.36), L-carvone (*log* K_{ow} = 2.74), linalool (*log* K_{ow} = 2.97), florhydral (*log* K_{ow} = 3.02), citronellol (*log* K_{ow} = 3.3), α-pinene (*log* K_{ow} = 4.44) and limonene (*log* K_{ow} = 4.57). Results showed that the most hydrophilic fragrance, 2-phenyl ethanol was solubilized in the polymeric micelles causing a slight swelling. With the remaining 6 PRMs, using a combination of CLSM and CRM imaging, different micro-structures were identified: i) matrix-type particles for florhydral and L-carvone; ii) vesicle-like particles in the presence of linalool and β-citronellol showing a co-surfactant behavior to the polymer; iii) perfume emulsion stabilized by polymer micelles for α-pinene and R-limonene. These results showed that no clear relation can be found between the PRM's *log* K_{ow} and the observed micro-structure and the hydrophobicity of the molecule is not enough to characterize such complicated systems, but specific chemical characteristics of the perfume (e.g. functional groups, bulkiness, conformation) need to addressed.

In the last experimental part of the thesis, two different polymers, the commercially available Soluplus and polymer S2 (synthesized within the

SAMCAPS network), based on the PEG-*g*-(PVAc-*co*-PVCL) structure were tested and compared by means of capsule formation and performance in a simplified liquid fabric enhancer. Polymer S2, with higher M_w, grafting degree and lower CPT compared to Soluplus, was found to self-assemble and form stable micro-capsules in the SLFE matrix. This is of great importance for industry, where liquid formulations with high surfactant levels are being used. As a last step, performance tests were carried out to evaluate the benefit of perfume encapsulation in the polymeric capsules after deposition on fabrics. Headspace GC-MS analysis showed the benefit of encapsulation compared to reference samples without encapsulating agent, that was more pronounced after 48 h of drying the fabrics. No distinction between the two polymers' performance was observed, suggesting that variations on polymer's properties (e.g. CPT, M_w etc.) can lead to different self-assembly in the solution, but do not significantly affect its performance upon deposition and wash conditions, allowing the technology to be unaffected by relatively broad specifications of the raw materials.

As a conclusion, graft copolymers like PEG-*g*-PVAc and PEG-*g*-(PVAc-*co*-PVCL) were shown to be extremely promising candidates for the encapsulation of perfume. They offer a choice of thermodynamically stable means of encapsulation, where the spontaneous formation upon simple mixing of the components results in a low-energy input and thus cost-effective production. It is important that formulation design takes into account the details of PRM-to-polymer interactions, as it was shown to dramatically affect the obtained encapsulation system. Fundamental studying and understanding of these phenomena will pave the way towards giving to the market a new generation of perfume encapsulation technologies.

References

1 K.-G. Fahlbusch, F.-J. Hammerschmidt, J. Panten, W. Pickenhagen, D. Schatkowski, K. Bauer, D. Garbe and H. Surburg, in *Ullmann's Encyclopedia of Industrial Chemistry*, Wiley-VCH Verlag GmbH & Co. KGaA, Weinheim, Germany, 2003, pp. 341–358.

2 S. P. De Matos, H. F. Teixeira, Á. A. N. De Lima, V. F. Veiga-Junior and L. S. Koester, *Biomolecules*, 2019, **9**, 1–19.

3 C. Turek and F. C. Stintzing, *Compr. Rev. Food Sci. Food Saf.*, 2013, **12**, 40–53.

4 L. Pavoni, F. Maggi, F. Mancianti, S. Nardoni, V. V. Ebani, M. Cespi, G. Bonacucina and G. F. Palmieri, *J. Drug Deliv. Sci. Technol.*, 2019, **53**, 101101.

5 H. Majeed, Y.-Y. Bian, B. Ali, A. Jamil, U. Majeed, Q. F. Khan, K. J. Iqbal, C. F. Shoemaker and Z. Fang, *RSC Adv.*, 2015, **5**, 58449–58463.

6 V. Nedovic, A. Kalusevic, V. Manojlovic, S. Levic and B. Bugarski, *Procedia Food Sci.*, 2011, **1**, 1806–1815.

7 US Patent 2,800,457, 1957.

8 US Patent 2,800,458, 1957.

9 M. Showell, *Handbook of Detergents, Part D*, CRC Press, 2016.

10 K. Bruyninckx and M. Dusselier, *ACS Sustain. Chem. Eng.*, 2019, **7**, 8041–8054.

11 N. A. Welden and A. Lusher, *Microplastics: from origin toimpacts*, Elsevier Inc., 2020.

12 J. Boucher and D. Friot, *Primary Microplastics in the Oceans*, 2017, vol. 111.

13 GESAMP, *Sources, fate and effects of microplastics in the marine environment*, IMO, 2015.

14 I. T. Carvalho, B. N. Estevinho and L. Santos, *Int. J. Cosmet. Sci.*, 2016, **38**, 109–119.

15 G. Molina, V. K. Gupta, B. N. Singh and N. Gathergood, *Bioprocessing*

for Biomolecules Production, John Wiley & Sons, Ltd, Chichester, UK, 2019.

16 A. Santini, G. C. Tenore and E. Novellino, *Eur. J. Pharm. Sci.*, 2017, **96**, 53–61.

17 A. Madene, M. Jacquot, J. Scher and S. Desobry, *Int. J. Food Sci. Technol.*, 2006, **41**, 1–21.

18 A. R. Patel and K. P. Velikov, *LWT - Food Sci. Technol.*, 2011, **44**, 1958–1964.

19 X. Zhao, H. Cui, Y. Wang, C. Sun, B. Cui and Z. Zeng, *J. Agric. Food Chem.*, 2018, **66**, 6504–6512.

20 J. Kumar, N. A. Shakil, M. K. Singh, M. K. Singh, A. Pandey and R. P. Pandey, *J. Environ. Sci. Health. B.*, 2010, **45**, 310–314.

21 C. Maes, S. Bouquillon and M. L. Fauconnier, *Molecules*, 2019, **24**, 1–15.

22 J. O. Werdin González, E. N. Jesser, C. A. Yeguerman, A. A. Ferrero and B. Fernández Band, *Environ. Sci. Pollut. Res.*, 2017, **24**, 17006–17015.

23 Q. Yue, X. Shao, Y. Wei, S. Jiang, F. Xu, H. Wang and H. Gao, *Postharvest Biol. Technol.*, 2020, **162**, 111114.

24 Y. Xue, S. Zhou, C. Fan, Q. Du and P. Jin, *Nanomaterials*, 2019, **9**, 1777.

25 D. J. Merline, S. Vukusic and A. A. Abdala, *Polym. J.*, 2013, **45**, 413–419.

26 D. X. Zhang, B. X. Li, X. P. Zhang, Z. Q. Zhang, W. C. Wang and F. Liu, *J. Agric. Food Chem.*, 2016, **64**, 2841–2846.

27 Z. Liao, D. Xue, H. Li and L. Shi, *J. Appl. Polym. Sci.*, 2016, **133**, 1–7.

28 N. Paret, A. Trachsel, D. L. Berthier and A. Herrmann, *Macromol. Mater. Eng.*, 2019, **304**, 1–15.

29 P. A. Winsor, *Trans. Faraday Soc.*, 1948, **44**, 376.

30 P. Izquierdo, J. Esquena, T. F. Tadros, J. C. Dederen, J. Feng, M. J. Garcia-Celma, N. Azemar and C. Solans, *Langmuir*, 2004, **20**, 6594–6598.

31 I. Solè, C. M. Pey, A. Maestro, C. González, M. Porras, C. Solans and

J. M. Gutiérrez, *J. Colloid Interface Sci.*, 2010, **344**, 417–423.

32 L. Shang, Y. Cheng and Y. Zhao, *Chem. Rev.*, 2017, **117**, 7964–8040.

33 A. Sedaghat Doost, F. Devlieghere, A. Dirckx and P. Van der Meeren, *J. Food Process. Preserv.*, 2018, **42**, 1–12.

34 A. V. Sadovoy, M. V. Lomova, M. N. Antipina, N. A. Braun, G. B. Sukhorukov and M. V. Kiryukhin, *ACS Appl. Mater. Interfaces*, 2013, **5**, 8948–8954.

35 Z. Ji, Y. Tang, C. Wang and J. Yang, *Polym. Bull.*, 2021, **78**, 1821–1833.

36 A. Gordillo-galeano and C. E. Mora-huertas, *Eur. J. Pharm. Biopharm.*, 2018, **133**, 285–308.

37 N. Naseri, H. Valizadeh and P. Zakeri-milani, *Tabriz Univ. Med. Sci.*, 2015, **5**, 305–313.

38 A. Cortial, M. Vocanson, E. Loubry and S. Briançon, *Flavour Fragr. J.*, 2015, **30**, 467–477.

39 B. Rodenak-Kladniew, G. A. Islan, M. G. de Bravo, N. Durán and G. R. Castro, *Colloids Surfaces B Biointerfaces*, 2017, **154**, 123–132.

40 S. Bashiri, B. Ghanbarzadeh, A. Ayaseh, J. Dehghannya and A. Ehsani, *LWT - Food Sci. Technol.*, 2020, **119**, 108836.

41 J. N. Israelachvili, *Intermolecular and Surface Forces 3d edition*, Elsevier, 2011.

42 R. Kaur, D. Kukkar, S. K. Bhardwaj, K.-H. Kim and A. Deep, *J. Control. Release*, 2018, **285**, 81–95.

43 G. Gaucher, M. H. Dufresne, V. P. Sant, N. Kang, D. Maysinger and J. C. Leroux, *J. Control. Release*, 2005, **109**, 169–188.

44 D. L. Berthier, I. Schmidt, W. Fieber, C. Schatz, A. Furrer, K. Wong and S. Lecommandoux, *Langmuir*, 2010, **26**, 7953–7961.

45 I. Grillo, I. Morfin and S. Prévost, *Langmuir*, 2018, **34**, 13395–13408.

46 L. Deng, M. Taxipalati, F. Que and H. Zhang, *Nat. Publ. Gr.*, 2016, 1–8.

47 T. M. Popiolski, I. Otsuka, S. Halila, E. C. Muniz, V. Soldi and R. Borsali, *Mater. Res.*, 2016, **19**, 1356–1365.

48 T. Zhang, Z. Lu, X. Wang, J. Shen, J. Wang, Y. Niu, Z. Xiao and X. Zhang, *Chinese Chem. Lett.*, 2020, 1–4.

49 F. H. Xavier-Junior, C. Vauthier, A. R. V. Morais, E. N. Alencar and E. S. T. Egito, *Drug Dev. Ind. Pharm.*, 2017, **43**, 700–714.

50 M. Cespi, L. Quassinti, D. R. Perinelli, M. Bramucci, R. Iannarelli, F. Papa, M. Ricciutelli, G. Bonacucina, G. F. Palmieri and F. Maggi, *Flavour Fragr. J.*, 2017, **32**, 159–164.

51 O. A. Chat, N. Nazir, P. A. Bhat, P. A. Hassan, V. K. Aswal and A. A. Dar, *Langmuir*, 2018, **34**, 1010–1019.

52 K. Letchford and H. Burt, *Eur. J. Pharm. Biopharm.*, 2007, **65**, 259–269.

53 Y. Zhu, B. Yang, S. Chen and J. Du, *Prog. Polym. Sci.*, 2017, **64**, 1–22.

54 L. Lin, X. Zhang, C. Zhao and H. Cui, *RSC Adv.*, 2016, **6**, 978–986.

55 C. Sebaaly, A. Jraij, H. Fessi, C. Charcosset and H. Greige-Gerges, *Food Chem.*, 2015, **178**, 52–62.

56 A. Yaghmur, in *Lipid-Based Nanostructures for Food Encapsulation Purposes*, Elsevier, 2019, pp. 483–522.

57 I. Martiel, S. Handschin, W. K. Fong, L. Sagalowicz and R. Mezzenga, *Langmuir*, 2015, **31**, 96–104.

58 B. Jia, Z. Zhang, M. H. Chen and W. P. Zhang, *J. Dispers. Sci. Technol.*, 2017, **38**, 876–882.

59 S. G. Ferreira, V. S. Conceição, N. S. Gouveia, G. S. Santos, R. L. C. Santos, A. A. M. Lira, S. C. H. Cavalcanti, V. H. V. Sarmento and R. S. Nunes, *J. Colloid Interface Sci.*, 2015, **456**, 190–196.

60 J. Wan, S. mei Wang, Z. ping Gui, Z. zhuan Yang, Q. qian Shan, X. qin Chu, S. ying Gui and Y. Yang, *Eur. J. Pharm. Sci.*, 2018, **125**, 93–101.

61 C. Tian, L. Liu, M. Xia and X. qin Chu, *AAPS PharmSciTech*, 2020, **21**, 1–13.

62 M. Wang and Y. Wang, *Soft Matter*, 2014, **10**, 7909–7919.

63 F. Ganachaud and J. L. Katz, *ChemPhysChem*, 2005, **6**, 209–216.

64 S. A. Vitale and J. L. Katz, *Langmuir*, 2003, **19**, 4105–4110.

65 A. Bartolini, P. Tempesti, A. F. Ghobadi, D. Berti, J. Smets, Y. G.

Aouad and P. Baglioni, *J. Colloid Interface Sci.*, 2019, **556**, 74–82.

66 N. Devi, M. Sarmah, B. Khatun and T. K. Maji, *Adv. Colloid Interface Sci.*, 2017, **239**, 136–145.

67 Y. Yuan, M.-F. Li, W.-S. Chen, Q.-Z. Zeng, D.-X. Su, B. Tian and S. He, *Int. J. Food Sci. Technol.*, 2018, **53**, 1681–1688.

68 E. Hasanvand and A. Rafe, *Int. J. Biol. Macromol.*, 2019, **131**, 60–66.

69 X. Z. Kong, X. Gu, X. Zhu and Z. Zhang, *Biomed. Microdevices*, 2009, **11**, 275–285.

70 C. Ternat, G. Kreutzer, C. J. G. Plummer, T. Q. Nguyen, A. Herrmann, L. Ouali, H. Sommer, W. Fieber, M. I. Velazco, H. A. Klok and J. A. E. Månson, *Macromol. Chem. Phys.*, 2007, **208**, 131–145.

71 C. Ternat, L. Ouali, H. Sommer, W. Fieber, M. I. Velazco, C. J. G. Plummer, G. Kreutzer, H. A. Klok, J. A. E. Månson and A. Herrmann, *Macromolecules*, 2008, **41**, 7079–7089.

72 W. Fieber, A. Herrmann, L. Ouali, M. I. Velazco, G. Kreutzer, H. A. Klok, C. Ternat, C. J. G. Plummer, J. A. E. Manson and H. Sommer, *Macromolecules*, 2007, **40**, 5372–5378.

73 C. Song, L. Li, L. Dai and S. Thayumanavan, *Polym. Chem.*, 2015, **6**, 4828–4834.

74 A. Bartolini, P. Tempesti, C. Resta, D. Berti, J. Smets, Y. G. Aouad and P. Baglioni, *Phys. Chem. Chem. Phys.*, 2017, **19**, 4553–4559.

75 A. Ciobanu, D. Landy and S. Fourmentin, *Food Res. Int.*, 2013, **53**, 110–114.

76 L. Cai, D. Jeremic, H. Lim and Y. Kim, *Ind. Crops Prod.*, 2019, **130**, 42–48.

77 M. Shrestha, T. M. Ho and B. R. Bhandari, *Food Chem.*, 2017, **221**, 1474–1483.

78 M. Durante, M. S. Lenucci, P. P. Marrese, V. Rizzi, M. De Caroli, G. Piro, P. Fini, G. L. Russo and G. Mita, *Food Chem.*, 2016, **199**, 684–693.

79 BASF, *Soluplus—technical information*, 2010.

80 NCNR, Neutron scattering lengths and cross sections.

81 E. Oksanen, J. C.-H. Chen and S. Z. Fisher, *Molecules*, 2017, **22**, 596.

82 A. Guinier and G. Fournet, *Small-angle scattering of X-rays*, John Wiley & Sons, New York, 1955.

83 O. K. O. Glatter, *Small Angle X-Ray Scattering*, Academic Press, 1982.

84 T. Zemb and P. Lindner, *Neutron, X-rays and Light. Scattering Methods Applied to Soft Condensed Matter*, North Holland, 1988.

85 S. R. Kline, *J. Appl. Crystallogr.*, 2006, **39**, 895–900.

86 J. B. Pawley, *Handbook Of Biological Confocal Microscopy*, Springer US, Boston, MA, 2006.

87 J. Müller, W. Ibach, K. Weishaupt and O. Hollricher, *Confocal Raman Microscopy*, Springer International Publishing, Cham, 2018, vol. 66.

88 HORIBA Scientific, Raman Theory.

89 K. Klein, A. M. Gigler, T. Aschenbrenner, R. Monetti, W. Bunk, F. Jamitzky, G. Morfill, R. W. Stark and J. Schlegel, *Biophys. J.*, 2012, **102**, 360–368.

90 N. N. Smirnova, T. A. Bykova, K. Van Durme and B. Van Mele, *J. Chem. Thermodyn.*, 2006, **38**, 879–883.

91 A. Bartolini, P. Tempesti, C. Resta, D. Berti, J. Smets, Y. G. Aouad and P. Baglioni, *Phys. Chem. Chem. Phys.*, 2017, **19**, 4553–4559.

92 M. Mamusa, P. Tempesti, A. Bartolini, E. Carretti, A. F. Ghobadi, J. Smets, Y. G. Aouad and P. Baglioni, *Nanoscale*, 2019, **11**, 6635–6643.

93 M. Valero, F. Castiglione, A. Mele, M. A. da Silva, I. Grillo, G. González-Gaitano and C. A. Dreiss, *Langmuir*, 2016, **32**, 13174–13186.

94 F. Castiglione, M. Valero, C. A. Dreiss and A. Mele, *J. Phys. Chem. B*, 2011, **115**, 9005–9013.

95 J. Wang, N. Wang, B. Liu, J. Bai, P. Gong, G. Ru and J. Feng, *Phys. Chem. Chem. Phys.*, 2017, **19**, 30097–30106.

96 M. Stieger, J. S. Pedersen, P. Lindner and W. Richtering, *Langmuir*, 2004, **20**, 7283–7292.

97 M. Teubner and R. Strey, *J. Chem. Phys.*, 1987, **87**, 3195–3200.

98 R. D. Koehler and K.-V. Schubert, *J. Chem. Phys.*, 1994, **101**, 10843–10849.

99 D. J. Kinning and E. L. Thomas, *Macromolecules*, 1984, **17**, 1712–1718.

100 P. Alexandridis, U. Olsson and B. Lindman, *Langmuir*, 1997, **13**, 23–34.

101 P. Alexandridis, U. Olsson and B. Lindman, *Langmuir*, 1998, **14**, 2627–2638.

102 P. A. Winsor, *Trans. Faraday Soc.*, 1948, **44**, 376.

103 R. Nagarajan, M. Barry and E. Ruckenstein, *Langmuir*, 1986, **2**, 210–215.

104 E. Fischer, W. Fieber, C. Navarro, H. Sommer, D. Benczédi, M. I. Velazco and M. Schönhoff, *J. Surfactants Deterg.*, 2009, **12**, 73–84.

105 L. Dian, E. Yu, X. Chen, X. Wen, Z. Zhang, L. Qin, Q. Wang, G. Li and C. Wu, *Nanoscale Res. Lett.*, 2014, **9**, 1–11.

106 S. F. Taveira, A. Varela-Garcia, B. dos Santos Souza, R. N. Marreto, M. Martin-Pastor, A. Concheiro and C. Alvarez-Lorenzo, *Carbohydr. Polym.*, 2018, **200**, 278–288.

107 F. Alvarez-Rivera, D. Fernández-Villanueva, A. Concheiro and C. Alvarez-Lorenzo, *J. Pharm. Sci.*, 2016, **105**, 2855–2863.

108 M. Linn, E.-M. Collnot, D. Djuric, K. Hempel, E. Fabian, K. Kolter and C.-M. Lehr, *Eur. J. Pharm. Sci.*, 2012, **45**, 336–343.

109 I. Salah, M. A. Shamat and M. T. Cook, *J. Appl. Polym. Sci.*, 2019, **136**, 1–9.

110 H. Yu, D. Xia, Q. Zhu, C. Zhu, D. Chen and Y. Gan, *Eur. J. Pharm. Biopharm.*, 2013, **85**, 1325–1336.

111 M. Saydam, W. P. Cheng, N. Palmer, F. Mawas, R. Francis, K. MacLellan-Gibson and A. Khan, *Vaccine*, 2017, **35**, 2489–2495.

112 F. Andrade, P. Fonte, M. Oliva, M. Videira, D. Ferreira and B. Sarmento, *Int. J. Pharm.*, 2015, **486**, 195–206.

113 M. Cespi, L. Casettari, G. F. Palmieri, D. R. Perinelli and G. Bonacucina, *Colloid Polym. Sci.*, 2014, **292**, 235–241.

114 C. C. Pola, A. R. F. Moraes, E. A. A. Medeiros, R. F. Teófilo, N. F. F. Soares and C. L. Gomes, *Food Chem.*, 2019, **295**, 671–679.

115 C. Miao, F. Li, Y. Zuo, R. Wang and Y. Xiong, *RSC Adv.*, 2016, **6**, 3013–3019.

116 M. Wei, X. Song, X. Pan, R. Li, C. Chen, X. Du and J. Li, *Appl. Sci.*, 2020, **10**, 1677.

117 Y. E. Kirsh, *Prog. Polym. Sci.*, 1993, **18**, 519–542.

118 L. Li, *Macromolecules*, 2002, **35**, 5990–5998.

119 K. Rao, K. Rao and C.-S. Ha, *Gels*, 2016, **2**, 6.

120 M. N. Mohammed, K. Bin Yusoh and J. H. B. H. Shariffuddin, *Mater. Express*, 2018, **8**, 21–34.

121 Y. F. T. Moritani, *Macromolecules*, 1977, **10**, 532–535.

122 G. V. Bonde, G. Ajmal, S. K. Yadav, P. Mittal, J. Singh, B. V. Bakde and B. Mishra, *Colloids Surfaces B Biointerfaces*, 2020, **185**, 110611.

123 W. Van De Sande and A. Persoons, *J. Phys. Chem.*, 1985, **89**, 404–406.

124 N. Merlet-Lacroix, E. Di Cola and M. Cloitre, *Soft Matter*, 2010, **6**, 984–993.

125 H. Senff and W. Richtering, *J. Chem. Phys.*, 1999, **111**, 1705–1711.

126 A. F.-N. U. Gasser, J. S. Hyatt, J.-J. Lietor-Santos, E. S. Herman, L. A. Lyon, *J. Chem. Phys.*, , DOI:10.1063/1.4885444.

127 P. S. Mohanty, N. Sofi and K. Van Gruijthuijsen, 2017, 1–8.

128 S. H. Chen, M. Broccio, Y. Liu, E. Fratini and P. Baglioni, *J. Appl. Crystallogr.*, 2007, **40**, 321–326.

129 M. Stieger, J. S. Pedersen and P. Lindner, *J. Chem. Phys.*, 2004, **120**, 6197–6206.

130 K. Mortensen, *Polym. Adv. Technol.*, 2001, **12**, 2–22.

131 X. Zhou, X. Fan and C. He, *Macromolecules*, 2016, **49**, 4236–4244.

132 R. D. Koehler, K. -V. Schubert, R. Strey and E. W. Kaler, *J. Chem. Phys.*, 1994, **101**, 10843–10849.

133 G. Wu, B. Chu and D. K. Schneider, *J. Phys. Chem.*, 1995, **99**, 5094–5101.

134 D. Berti, F. B. Bombelli, M. Fortini and P. Baglioni, *J. Phys. Chem. B*, 2007, **111**, 11734–11744.

135 M. M. Vorob'ev, T. V. Burova, N. V. Grinberg, A. S. Dubovik, N. G.

Faleev and V. I. Lozinsky, *Colloid Polym. Sci.*, 2010, **288**, 1457–1463.

136 M. Horecha, V. Senkovskyy, K. Schneider, A. Kiriy and M. Stamm, *Colloid Polym. Sci.*, 2011, **289**, 603–612.

137 M. Cors, L. Wiehemeier, Y. Hertle, A. Feoktystov, F. Cousin, T. Hellweg and J. Oberdisse, *Langmuir*, 2018, **34**, 15403–15415.

138 M. J. Bergman, J. S. Pedersen, P. Schurtenberger and N. Boon, *Soft Matter*, 2020, **16**, 2786–2794.

139 T. Ishiguro, Y. Sakata, H. Arima, D. Iohara, M. Anraku, K. Uekama and F. Hirayama, *J. Incl. Phenom. Macrocycl. Chem.*, 2018, **92**, 147–155.

140 M. Kfoury, L. Auezova, H. Greige-Gerges and S. Fourmentin, *Environ. Chem. Lett.*, 2019, **17**, 129–143.

141 Y. Lan, S. Ali and N. Langley, *Characterization of Soluplus ®*, 2016.

142 P. Vargas Jentzsch and V. Ciobotă, *Flavour Fragr. J.*, 2014, **29**, 287–295.

143 J. R. Avilés Moreno, F. Partal Ureña and J. J. López González, *Vib. Spectrosc.*, 2009, **51**, 318–325.

144 M. D. Sutherland, *J. Am. Chem. Soc.*, 1952, **74**, 2688.

145 K. Thompson, *Ppportunities and challenges in encapsulation for home and personal care products*, 2014.

146 T. Shibanuma, T. Aoki, K. Sanui, N. Ogata, A. Kikuchi, Y. Sakurai and T. Okano, *Macromolecules*, 2000, **33**, 444–450.

147 X. Yin and H. D. H. Stöver, *Macromolecules*, 2003, **36**, 9817–9822.

148 X. Yin and H. D. H. Stöver, *Macromolecules*, 2005, **38**, 2109–2115.

149 L. Etchenausia, A. M. Rodrigues, S. Harrisson, E. Deniau Lejeune and M. Save, *Macromolecules*, 2016, **49**, 6799–6809.

150 X. Yin and H. D. H. Stöver, *J. Polym. Sci. Part A Polym. Chem.*, 2005, **43**, 1641–1648.

151 N. S. Ieong, M. Hasan, D. J. Phillips, Y. Saaka, R. K. O'Reilly and M. I. Gibson, *Polym. Chem.*, 2012, **3**, 794–799.

152 Z. Tong, F. Zeng, X. Zheng and T. Sato, *Macromolecules*, 1999, **32**, 4488–4490.

153 J. P. Swanson, M. R. Martinez, M. A. Cruz, S. G. Mankoci, P. J.

Costanzo and A. Joy, *Polym. Chem.*, 2016, **7**, 4693–4702.

154 Y. Yang, J. Li, M. Hu, L. Chen and Y. Bi, *J. Polym. Res.*, 2014, **21**, 549.

155 S. Verbrugghe, K. Bernaerts and F. E. Du Prez, *Macromol. Chem. Phys.*, 2003, **204**, 1217–1225.

156 S. Verbrugghe, A. Laukkanen, V. Aseyev, H. Tenhu, F. M. Winnik and F. E. Du Prez, *Polymer (Guildf).*, 2003, **44**, 6807–6814.

157 R. Sharma and P. Bahadur, *J. Surfactants Deterg.*, 2002, **5**, 263–268.

158 S. K. Goel, *J. Colloid Interface Sci.*, 1999, **212**, 604–606.

159 C. Manohar and V. . Kelkar, *J. Colloid Interface Sci.*, 1990, **137**, 604–606.

160 A. Carlsson, G. Karlström and B. Lindman, *J. Phys. Chem.*, 1989, **93**, 3673–3677.

161 A. T. R. Williams and W. Slavin, *J. Agric. Food Chem.*, 1977, **25**, 756–759.

162 G. Pennazza, C. Fanali, M. Santonico, L. Dugo, L. Cucchiarini, M. Dachà, A. D'Amico, R. Costa, P. Dugo and L. Mondello, *Food Chem.*, 2013, **136**, 668–674.

163 J. M. Lee, D. H. Kim, P. S. Chang and J. H. Lee, *Food Chem.*, 2007, **105**, 414–420.

164 S. Gherghel, R. M. Morgan, J. Arrebola-Liébanas, R. Romero-González, C. S. Blackman, A. Garrido-Frenich and I. P. Parkin, *Forensic Sci. Int.*, 2018, **290**, 207–218.

Acknowledgements

As the completion of my PhD program is approaching, I feel the need to express my deep gratitude to the people, who each one of them helped me in their own way, to be here today.

Firstly, I would like to express my sincere gratitude to my academic advisor, Prof. Piero Baglioni, for his support, motivation, endless ideas, and passion for science, leading me to fall in love with science even more. The knowledge he has transferred to me through his guidance for all the scientific topics related with my thesis, had helped me within the past three years to grow scientifically and feel confident to work as an independent researcher. It has been an honour to work with Prof. Baglioni and have as my PhD advisor one of the greatest scientific minds of his generation.

Second, I would like to express my deep sense of thanks to my industrial advisor, Dr. Johan Smets, for introducing me to the fascinating world of innovation. His immense knowledge on the applied part of my research and his passion for the discovery of new technologies has tremendously pushed me towards discovering a new and ambitious version of myself.

At this point, I would like to thank several people from CSGI Florence and Procter&Gamble Brussels for their individual contribution to the completion of my PhD. I would like to warmly thank Dr. Michele Baglioni for a great scientific collaboration during the last year of my PhD and for reminding me how productive I can be when I work with kind people who enjoy doing research. I would like to say a big thank you to my project manager, Susana Fernandez-Prieto, for being a role model to me and showing me that a strong, independent woman can be a successful, multi-tasking and brilliant scientist without sacrificing either her career or family. My sincerest thanks to Dr. Marianna Mamusa for all the scientific knowledge on colloids and phase diagrams but also for leading me in becoming a stronger person. I would also like to thank Dr. Claudio Resta for all the enjoyable discussions (scientific, political etc.) and for guiding me through the chemical modification and NMR topics of my PhD. A warm thank you to Dr. Beth Schubert and Prof. Debora Berti for always being polite to me and providing me with useful scientific

feedback during the three years of my PhD. I would like to especially thank my colleague and eventually friend, Cedric Tahon, for all the scientific enthusiasm and the relaxing moments we've shared together at BIC. I would like to also thank Arianna, Giulia, Jacopo, Rosangela, Teresa, Marietta, Laura and all the other collaborators and friends at CSGI for the nice moments we've spent together in Polo Scientifico di Sesto Fiorentino. Of course, I would like to thank all the rest of the SAMCAPS team and collaborators from CSGI and P&G, among them Prof. Massimo Bonini, Dr. Jeremy Gummel, Mattia Collu and Patrizia Zitelli.

Special thanks to the other three SAMCAPS early-stage researchers and my "partners in crime", Aleksandra Zawadka, Xavier Castellvi-Corrons and Keo-Oudone Seymany (soon all with a Dr. in front of our names), for sharing the PhD journey together with all its ups and downs, but also full of nice moments that will accompany us forever.

I would also like to thank the European Union's Horizon 2020 research and innovation programme and the Marie Skłodowska-Curie actions for funding this project under the grant agreement No 814100.

Last but not least, I would like to deeply thank from all my heart, my family, my mother, Barbara, my father, Marios, my brother, Simos, my grandparents and my partner, Andreas, for their continuous support in every possible way, their endless faith in me even the moments that myself I was losing it and for their urge in pursuing my dreams.

Appendix

List of publications related to this PhD

Paper I: Mamusa, M.; Sofroniou, C.; Murgia, S.; Resta, C.; Smets, J.; Baglioni, P. *Tuning the encapsulation of simple perfumes with amphiphilic graft copolymers.* ACS Appl. Mater. Interfaces, 12 (2020) 25, 28808–28818. https://doi.org/10.1021/acsami.0c05892

Paper II: Sofroniou, C.; Baglioni, M.; Mamusa, M.; Resta, C.; Doutch, J.; Smets, J.; Baglioni, P. *Self-assembly of Soluplus in aqueous solutions: characterization and prospectives on perfume encapsulation.* ACS Appl. Mater. Interfaces (2022). https://doi.org/10.1021/acsami.2c01087

Paper III: Mamusa, M.; Resta, C.; Sofroniou, C.; Baglioni, P. *Encapsulation of volatile compounds in liquid media: fragrances, flavours, essential oils in commercial formulations.* Advances in Colloid and Interface Science, 298 (2021) 102544. https://doi.org/10.1016/j.cis.2021.102544

Paper IV: Zawadka, A.; Sofroniou, C.; Leone, G.; Consumi, M.; Fernandez Prieto, S.; Semts, J.; Baglioni, P.; Magnani, A. *PEG-g-(PVAc-co-PVCL) amphiphilic graft copolymer with improved environmental footprint for fragrance encapsulation in commercial formulations.* In preparation

Conference presentations related to this PhD

Oral presentation (presenting author) on *Encapsulation of fragrances via the self-assembly of amphiphilic graft copolymers: The role of perfume nature* at the 35th conference of the European Colloid and Interfaces Society, September 2021, Athens, Greece

Poster presentation (presenting author) on *Self-assembly of amphiphilic copolymers in the presence of surfactants* at the 33rd conference of the European Colloid and Interfaces Society, September 2019, Leuven, Belgium

Poster presentation (co-author) on *A rational approach to liquid microencapsulation of fragrance materials via an amphiphilic copolymer* at the 10th International Colloids Conference by Elsevier (Online), December 2020

Poster presentation (one out of four presenting authors) on *SAMCAPS Revolution: Synthesis, Characterization and Eco-friendly Application of Self-Assembled MicroCAPSules in Home Care Products* at the Marie Curie Alumni Association 6th General Assembly and Annual Conference, February 2019, Vienna, Austria

Other publications

Sofroniou, C.; Chazapi, I.; Leontidis, E. *Binding of lanthanide salts to zwitterionic phospholipid micelles*. Journal of Colloid and Interface Science, 557 (2019) 568-579. https://doi.org/10.1016/j.jcis.2019.09.048

Tatini, D.; Ciardi, D.; Sofroniou, C.; Ninham, B. W.; Lo Nostro, P. *Physicochemical characterization of green sodium oleate-based formulations. Part 2. Effect of anions. Specific ion effect on the properties of sodium oleate viscoelastic dispersions – anions.* Journal of Colloid and Interface Science 617 (2022) 399-408. https://doi.org/10.1016/j.jcis.2022.01.135